Radiation Damage in Charge Coupled Devices

Thesis submitted for the degree of
Doctor of Philosophy
at the University of Leicester

by

David Ryan Smith
Space Projects and Instrumentation Group
Department of Physics and Astronomy
University of Leicester

12^{th} September 2003

Radiation Damage in Charge Coupled Devices

David Ryan Smith

Abstract

This thesis is concerned with the effects of radiation damage in CCDs used for space applications. The manufacturing process and operational principles of CCDs are presented in Chapter 2. The space radiation environment, the two radiation damage mechanisms relevant to CCDs, and the effects of radiation on the operational characteristics of CCDs are described in Chapter 3.

Chapter 4 presents a study to assess the suitability of novel low light level L3Vision CCD technology to applications in space. Two L3Vision CCDs were subjected to proton irradiations representative of doses expected to be received by spacecraft in low Earth orbit. Post-irradiation the devices were found to operate as expected, the effects of radiation on the operational characteristics of the devices being comparable to previous studies.

The effect of low energy protons on CCDs is the subject of Chapter 5. The study was initiated in response to the finding that soft protons could be focused by the mirror modules of the XMM-Newton spacecraft onto the EPIC CCD detectors. Two EPIC devices were irradiated with protons of a few keV to find that soft protons cause more damage than that expected by the Non-Ionising Energy Loss damage relationship, as they deposit most of their energy within the CCD. The observed change in CTI of the EPIC devices on XMM-Newton is however comparable to the pre-launch prediction, and the component attributable to low energy protons is small, <20 %.

Chapter 6 presents a study of a specific radiation induced phenomenon, ‘Random Telegraph Signals’. Development of analysis software and the irradiation of two CCDs are discussed before a detailed characterisation of the generated RTS pixels is presented. The study shows that the mechanism behind RTS involves a bi-stable defect linked with the E-centre, in combination with the high field regions of a CCD pixel.

Declaration

I hereby declare that no part of this thesis has been previously submitted to this or any other university as part of the requirement for a higher degree. The work described herein was conducted solely by the undersigned except for those colleagues and other workers acknowledged in the text.

David Ryan Smith

12th September 2003

Dedication

To my family and everyone who believed I could do it.

Acknowledgements

I would like to acknowledge the following people for their help and encouragement over the duration of my thesis work.

Thanks go to my supervisor Andrew Holland for his guidance, advice and gentle pushing in the right direction, and also to Adam, Richard, Ian, Nick and Alex for their support and continued assurance that I was not a 'normal' student.

Thanks to all the staff of the Space Research Centre for their technical assistance in and out of the lab and for their general chat and friendship that made my three years so enjoyable.

Thanks also to the staff of E2V Technologies, especially Mark Robbins and Dave Burt, for their wise words and help when it was needed.

Finally, I would like to gratefully acknowledge the financial support received from the Particle Physics and Astronomy Research Council and E2V Technologies during my research studentship.

Contents

Chapter 1: Introduction

1.1. Radiation Damage in CCDs

The advantages of semiconductor detectors in astronomy have long been recognised. Semiconductor imaging detectors are generally smaller and require less power than gaseous and solid-state scintillation detectors, demonstrating better signal-to-noise, energy resolution and linearity over a wide energy range. In the 1960's semiconductor technology had progressed to a point where metal-oxide-semiconductor (MOS) devices could be combined into large arrays that allowed the storage and transport of charge through the many elements of the array. These charge-coupled devices (CCDs) had a number of applications in the electronics world in the form of memory storage components and analogue signal processors, but it was the development of silicon CCDs for use as imaging devices in the mid 1970's that gained the interest of NASA. By 1978 NASA had produced imaging CCDs of 500^2 pixels with noise levels below 10 electrons and by 1989 devices with 800^2 pixels with improved signal-to-noise and operational reliability were being manufactured and considered for potential instruments on upcoming space missions.

The launch of the Galileo mission to Jupiter in 1989 and the Hubble Space Telescope in 1990 resulted in the first astronomical images to be obtained from charge-coupled devices (CCDs) operating in space. The effects of the space radiation environment on CCD operational characteristics were also observed for the first time. The affect of radiation on CCD imagers had been studied since their initial development, however measurements from the devices in space revealed a number of new unexpected effects on device performance and output noise. The composition of the space radiation environment is complex and dependent on spacecraft orbit and solar activity. The major limitation to CCD reliability arises from damage caused by the space radiation environment which in extreme cases can render a device inoperable. Study of the space radiation environment and its effects on CCDs had begun and is the subject of this thesis.

CCD detector technology has advanced through the nineties with the development of many techniques to improve the radiation tolerance of devices and improve their spatial and spectral capabilities. CCDs have been used as optical and X-ray detectors on a large number of space missions and they emerged as the preferred detectors in all the X-ray missions of the nineties. The current trends in astronomy detector requirements are for increased imaging area, smaller pixel size, increased charge collection efficiency, faster readout and lower noise. These goals all lend themselves well to the continuing development of CCD technology with CCDs being chosen for several future optical and X-ray scientific missions currently planned or under study.

To date the largest CCD focal plane instruments operated in space are the twin European Photon Imaging Cameras (EPIC) cameras of the X-ray Multi Mirror (XMM-Newton) spacecraft, each composed of 7 individual CCDs. Focal plane instruments comprised of many more CCDs are envisioned for future missions to fulfil the demand for increased focal plane size. The main astrometric mapper instrument of the GAIA mission is composed of 160 CCDs covering a focal plane area of ~0.5 m^2, while the wide field imager CCD array planned for the X-ray Evolving Universe Spectroscopy (XEUS) mission consists of 16 CCDs optimised for X-ray detection. These missions are scheduled for launch in 2010 and 2015 respectively. The size of these planned instruments necessitates detailed radiation studies of the environment each spacecraft will be located in and the effects that environment will have on the devices.

The continued use of CCDs in space requires radiation testing of state of the art detectors to deduce their suitability for up coming space applications. There is also a need to analyse data obtained from CCD detectors currently in orbit to improve understanding of how the space radiation environment affects device operating characteristics and to characterise specific radiation damage phenomena. Long term measurements of on-orbit device degradation are now available from several spacecraft in different orbits for comparison with data obtained from ground based radiation experiments and modelling.

1.2. Research Goals

The work carried out for this thesis is comprised of three separate CCD irradiation studies. The aim of the first study was to assess the potential of using new E2V Technologies L3Vision CCD technology for space based applications. L3Vision CCDs feature a novel structural design that can reduce the effective readout noise of the device to less than one electron while operating at MHz pixel rates. This attribute is particularly useful for low light level (‘L3’) imaging applications. Two L3Vision CCDs were subjected to representative mission doses of protons and the effects of irradiation on the operational characteristics of the devices were investigated.

The second study examined the effects of low energy proton irradiation of E2V Technologies CCD22 devices. This is the same type of device used in the EPIC focal plane instruments of the XMM-Newton spacecraft. The investigation was carried out in response to the discovery that soft protons could be focused by scattering interactions with the mirrors of the Chandra (formerly AXAF) satellite onto the focal plane of the AXAF CCD Imaging Spectrometer (ACIS) instrument. The XMM-Newton spacecraft has a similar mirror structure to Chandra and is subject to the same focusing problem. A critical need for characterisation of the possible damage caused by different soft proton fluences was addressed with this work both experimentally and theoretically with the development of a computational model by the author.

The third radiation study involved the in-depth study of a particular radiation induced phenomenon in CCDs, fluctuating bright pixels, or 'Random Telegraph Signals' (RTS). RTS pixels have been observed in many CCD types as a result of irradiation and the underlying mechanism is not well understood. A detailed study of the phenomenon in two E2V Technologies CCD47-20 devices was carried out to obtain a better understanding of the characteristics of RTS pixels and to improve on the current accepted model of the underlying mechanism.

The work carried out for this thesis was funded by a Co-operative Award in Science and Engineering (CASE) studentship from the Particle Physics and Astronomy Research Council (PPARC) in collaboration with E2V Technologies (formerly Marconi, formerly EEV) of Chelmsford, Essex, England.

1.3. Thesis Organisation

There have been a number of theses on different aspects of CCD studies produced by the group at the University of Leicester including an investigation of the feasibility of detecting X-rays with conventional video CCDs (Lumb 1983), the use of high resistivity silicon in CCDs to improve high energy X-ray detection efficiency (Chowanietz 1986), radiation damage effects in CCDs for space applications (Holland 1990), the soft X-ray response of CCDs (Castelli 1991), three-dimensional modelling of astronomical CCDs for X-ray and UV detection (Kim 1995), fine structure effects in CCDs developed for the JET-X instrument (Keay 1997), device modelling of CCDs for the CUBIC mission (Hutchinson 1999), the use of CCDs for X-ray polarimetry (Hill 1999) and the use of CCDs for exotic atom X-ray spectroscopy to determine the charged pion mass and muon neutrino mass upper limit (Nelms 2002).

The work in this thesis continues the CCD theme with a further investigation of radiation damage effects in CCDs, in particular the effects of proton irradiation on novel devices for low light level applications, the effects of low energy protons on the EPIC MOS CCDs of XMM-Newton and the underlying mechanism behind radiation induced fluctuating CCD pixels.

The thesis is organised into seven chapters including this introduction. Chapter 2 describes how CCDs are manufactured, the structure of the different types of device available, how CCDs store and transport charge, CCD noise sources and how a CCD detects photons. A number of terms used for describing a CCD's performance are also detailed.

Chapter 3 outlines the space radiation environment and its effects on CCD operational characteristics. The various components of the space radiation environment are discussed before the two important radiation damage mechanisms for the study of radiation damage in CCDs, ionisation and displacement damage, are described.

Chapter 4 is an investigation of the effects of proton irradiation of L3Vision CCDs to deduce the suitability of this novel device technology for space applications. The device structure is described, followed by a description of the proton irradiation experiments and the effect proton irradiation had on the operational characteristics of the devices.

Chapter 5 describes soft proton irradiation experiments carried out on CCD22 devices, the same as those of the European Photon Imaging Cameras of XMM-Newton, to assess the effects of different low energy proton fluences on the device operating characteristics. The development of a computational model to simulate the charge transfer efficiency changes resulting from the soft proton irradiations is also presented.

Chapter 6 first describes an initial study of the 'Random Telegraph Signal' phenomenon in a CCD47-20 device. This study was carried out to allow improvement of the experimental set up and the development of analysis software for a far more in-depth study of the phenomenon using a second CCD47-20 device. The detailed study is then presented, after which the proposed theoretical models for explaining the mechanism behind RTS are discussed.

The final chapter, Chapter 7, recounts the main conclusions of this thesis and assesses the possible directions for future work.

1.4. Publications

Some of the results in this thesis are contained within the following publications. The thesis chapters to which these papers refer are given in brackets:

Smith, D. R., A. D. Holland, M. S. Robbins, "The effect of protons on E2V Technologies L3Vision CCDs", *Nuc. Inst. and Meth.*, vol. **A513**, (2003), pp. 296-99 [Chapter 4].

Abbey, A. F., R. M. Ambrosi, **D. R. Smith**, E. Kendziorra, I. Hutchinson, A. Short, P. Bennie, A. Holland, T. Clauss, M. Kuster, W. Rochow, M. Brandt, M. J. L. Turner, A. Wells, "The effect of low energy protons on the operational characteristics of EPIC-MOS CCDs", *Proc. RADECS*, (2001) [Chapter 5].

Ambrosi, R. M., **D. R. Smith**, A. F. Abbey, I. B. Hutchinson, E. Kendziorra, A. Short, A. Holland, M. J. L. Turner, A. Wells, "The impact of low energy proton damage on the operational characteristics of EPIC-MOS CCDs", *Nuc. Inst. and Meth.*, vol. **B207**, (2003), pp. 175-85 [Chapter 5].

Ambrosi, R. M., A. D. T. Short, A. F. Abbey, A. A. Wells, **D. R. Smith**, "The effect of proton damage on the X-ray spectral response of MOS CCDs for the Swift X-ray Telescope", *Nuc. Inst. and Meth.*, vol. **A482**, (2002), pp. 644-52 [Chapter 5].

Smith, D. R., A. D. Holland, M. S. Robbins, R. M. Ambrosi, I. B. Hutchinson, "Proton induced leakage current in CCDs", *Proc. SPIE*, vol. **4851**, (2003), pp. 842-48 [Chapter 6].

Smith, D. R., A. D. Holland, I. B. Hutchinson, "Random telegraph signals in charge coupled devices", accepted for publication in *Nuc. Inst. and Meth.*, vol. **A**, (2003) [Chapter 6].

Smith, D. R., R. M. Ambrosi, A. D. Holland, I. B. Hutchinson, A. Wells, "The prompt particle background and micrometeoroid environment at L2 and its implications for Eddington", in press, *Proc. 2nd Eddington Workshop*, ESA SP-485, (2003) [Chapter 6].

Chapter 2: The Charge Coupled Device

This chapter describes how CCDs are manufactured and the underlying principles of CCD operation. Charge storage, transfer and readout are detailed for both surface channel and buried channel devices. The various components of CCD noise are then discussed followed by the definition of several terms used to describe a CCD's operational characteristics.

2.1. Introduction

The charge-coupled device (CCD) was originally conceived by Boyle and Smith (1970) at Bell Telephone Laboratories in the late 1960's, and consists of a metal-oxide semiconductor (MOS) capacitor array usually made of silicon. An electrode structure is fabricated over the surface of the device that allows depletion regions to be formed under biased electrodes. Charge is collected in these depletion regions and by changing the bias of subsequent electrodes of the device, the charge 'packet' is transferred to an output circuit where the level of charge is measured. The technique of transferring, or 'coupling', charge from one electrode to another has a number of applications, for example analogue signal processing, high density memories and most importantly, imaging devices (Barbe 1975). For use as imaging devices, higher quality fabrication methods need to be employed to produce CCDs with fewer structural defects (Jastrzebski et al. 1981). Such defects are not as important in signal processing and memory devices where higher charge signals are used. In a CCD imaging device, charge is generated in proportion to the incident light intensity by the process of ionisation. The signal charge is collected in the depletion region of the MOS capacitors before it is transferred to the output node, amplified and measured. The distribution of the collected charge in the CCD forms an electronic image which is reconstructed after readout of the device. Since the initial design of the CCD many improvements in fabrication methods and device structure have been instigated to produce modern devices that can be used for high resolution imaging and spectroscopy in the X-ray and optical wavebands while withstanding the rigours of being launched into space and subjected to the space radiation environment for the duration of their operation.

This chapter describes how CCDs are fabricated and how a CCD collects, transfers and reads out charge. The different noise sources are also described along with a discussion of the performance parameters that characterise a device. Further information about CCDs and their applications can be found in Beynon and Lamb (1980), Sze (1981), Howes and Morgan (1979) and Janesick (2001).

2.2. CCD Fabrication and Structure

A CCD consists of strips of polysilicon electrode formed into an array by the presence of orthogonal 'channel stops' that prevent charge spreading along the length of the electrodes. Each CCD pixel consists of a set of two to four electrodes, usually three, that when biased collect charge and are used to 'clock' the signal packet to the readout node of the device. These 'three phase' devices are the most common due to their high process tolerance and high yield, although two and four phase devices are also available. Charge collected in the potential wells formed by the biased electrodes and channel stops is stored under an oxide insulating layer at the surface of the device. Such a device is called a 'surface channel' CCD. Figure 2.1 shows a section of a three phase surface channel CCD.

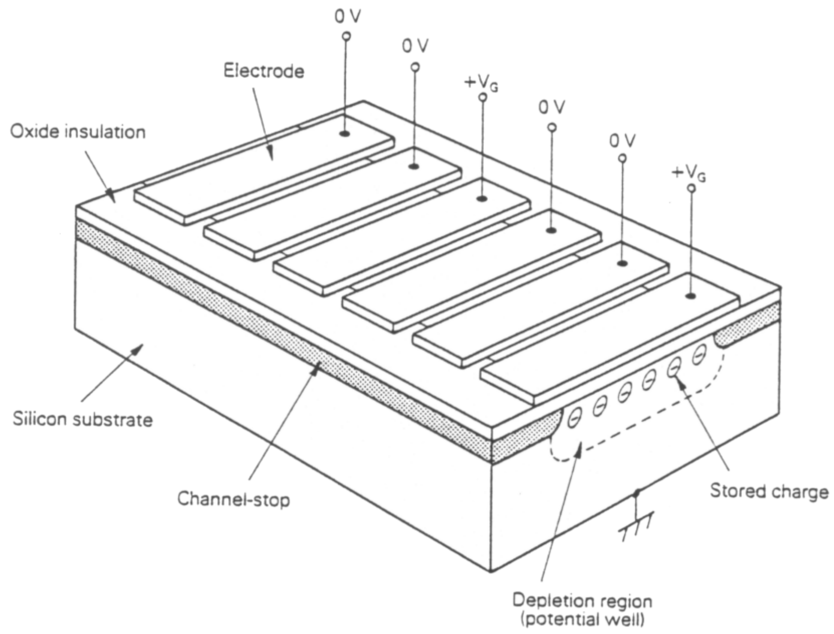

Figure 2.1 A section of a surface channel CCD showing the electrodes, channel stops, charge storage area and different layers of the CCD

The idea of transferring charge in a 'buried channel' was first suggested by Boyle and Smith in 1970, with the first test structures produced by 1972 (Walden et al. 1972). The buried channel device stores and transports charge a short distance, ~0.5 μm, below the Si-SiO_2 interface, greatly reducing the signal loss to lattice defects in the interface region. Impurity atoms in the silicon lattice have associated discrete energy levels that lie between the conduction and valence bands and it is here that the carriers can become 'trapped' (Grove 1967). Figure 2.2 illustrates the main defect complexes found in CCDs and lists some of their properties. Lattice defects are produced not only during the CCD manufacturing process but are also created as a result of displacement damage by energetic particles. Displacement damage is discussed in more detail in Chapter 3.

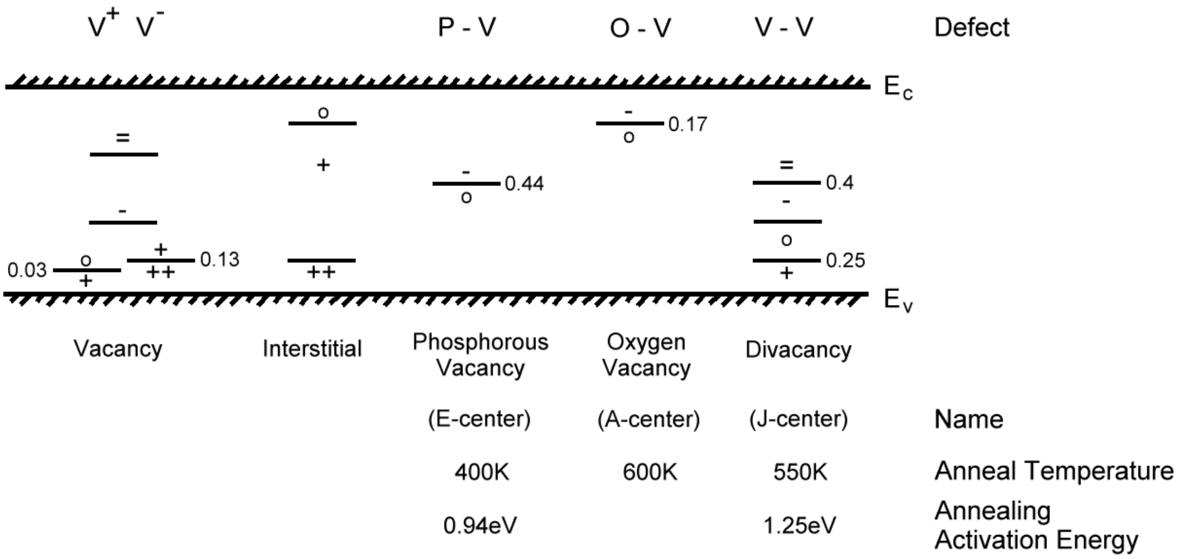

Figure 2.2 A diagram of the main defect complexes that form as a result of displacement damage in CCDs. Details of the energy levels induced in the silicon band-gap and the approximate annealing temperatures and activation energies are given. The energy levels are in eV measured from the nearest band edge

The CCD fabrication process involves firstly growing p-type epitaxial silicon over a heavily doped p+-type silicon substrate. The use of a heavily doped substrate has the advantage over bulk silicon that intrinsic gettering occurs during processing, where defects in the epitaxial silicon migrate to the substrate, increasing the purity and uniformity of the epitaxial layer and leaving fewer cosmetic defects in the finished device. The image area of the CCD is then defined by boron doping of the non-imaging area forming a p+ peripheral region. Charge from these areas is swept away by contacts to an external power supply during operation of the CCD, therefore not contributing charge to the image. The silicon surface is covered in a thermally grown oxide creating an insulating layer between the silicon and the polysilicon electrode structures that will be placed on top. The buried channel is then created by ion implantation, usually phosphorous, through the oxide layer to a peak concentration of ~5×10^{17} cm^{-3}, creating a p-n junction with the underlying p-type silicon. A silicon-nitride layer is then added to prevent contamination of the underlying silicon during later manufacturing steps, prevent further non-uniform growth of the oxide layer and improve the integrity of the electrical insulation of the two layers. A 1000 ^{o}C anneal is then given to anneal displacement damage resulting from the ion implantation. Photolithography processes are then used to build up the polysilicon electrode structures on top of the silicon-nitride. Each electrode is deposited in turn with 0.2 μm to 0.3 μm of oxide between each one, before a final layer of vapour phase grown oxide, 'VAPOX', is added to protect the electrode structure from particle contamination. Contact holes are then opened up in the oxide where bond pads and tracks to the electrodes and output register are needed and each device is cut from the wafer to be wire bonded and packaged for use. A more detailed description of the CCD manufacturing process is given in Morgan and Board (1983). A cross-section through a surface channel CCD is shown in Figure 2.3 and a buried channel CCD cross-section is shown in Figure 2.4. The electrode structure and various layers within each device are labelled.

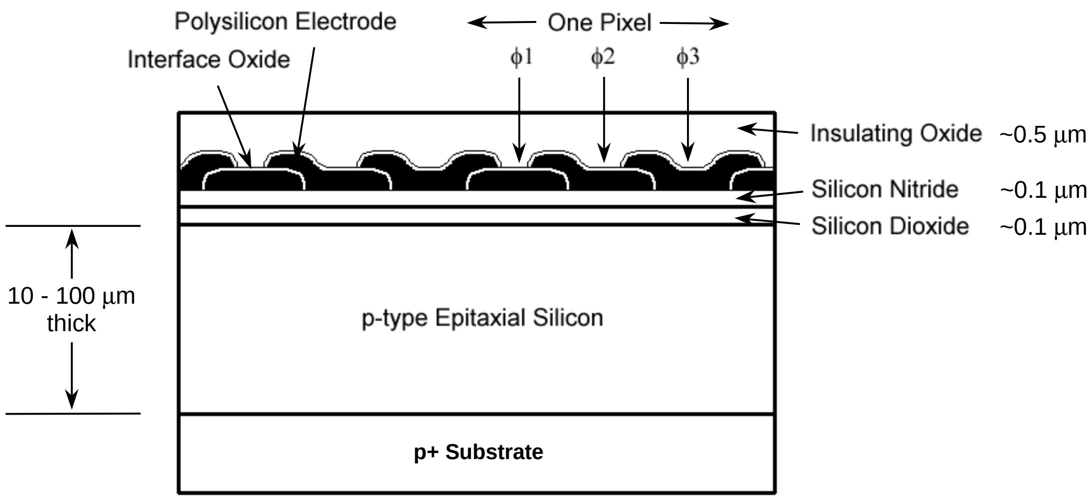

Figure 2.3 A cross-section through a surface channel CCD showing the 'overlapping' polysilicon electrode structure

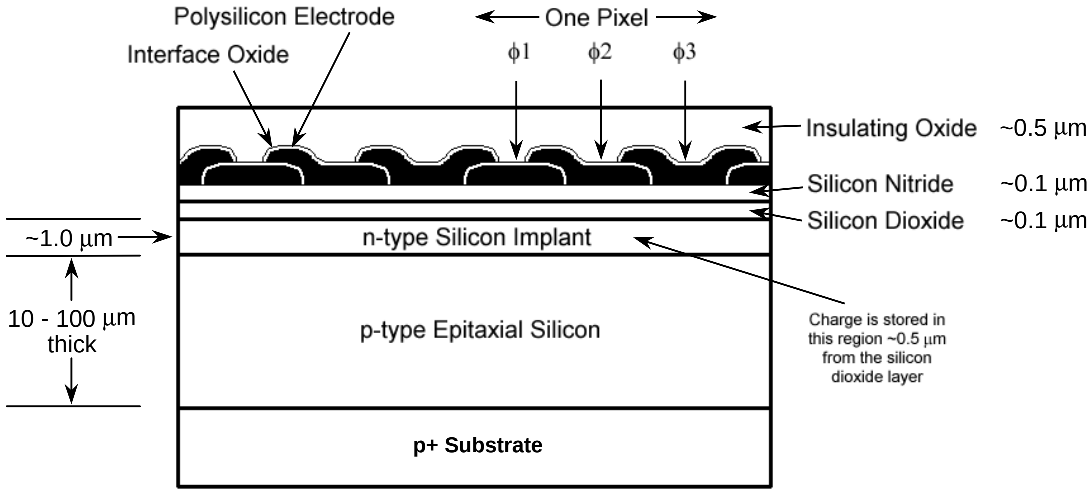

Figure 2.4 A cross-section through a buried channel CCD showing the charge storage region that located away from the Si-SiO_2 interface

The structure of a completed CCD is shown in Figure 2.5. The device shown is a 'frame transfer' device which has an 'image' section and a 'store' section. A device without a store section is called a 'full frame' device. During readout of the collected charge, additional charge will be accumulated if the image section of the CCD remains exposed to light. One method of preventing this extra charge causing unwanted image smear during readout is to have a shutter that can close over the image section, while another more commonly used technique is the use of a frame transfer device with a shielded store section. In the frame transfer device the image charge is transferred quickly to the store section of the device where readout can occur with no additional charge being accumulated. This type of device also has the added advantage of allowing the next image to be taken while readout is taking place.

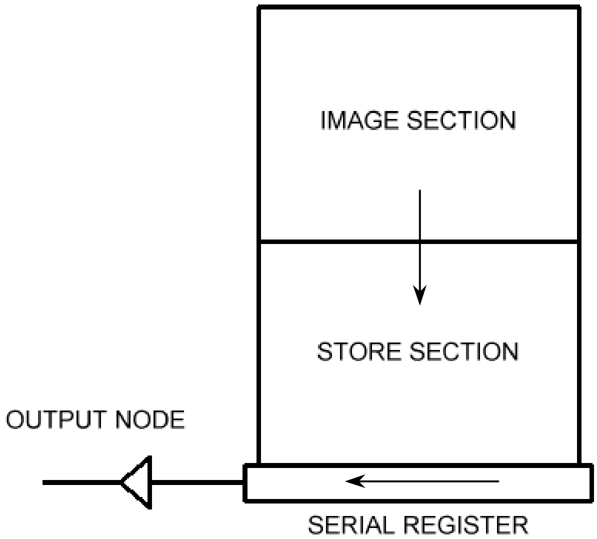

Figure 2.5 A schematic of a 'frame transfer' CCD. The arrows indicate the charge transfer direction

2.3. Potentials in a CCD

2.3.1. The Surface Channel Device

Signal charge generated by incident photons is collected in the 'depletion' region under the biased electrode in each CCD pixel. The potential applied to an electrode repels the majority carriers forming the depletion region. It is useful to consider a single MOS capacitor to understand the potentials and electric field in a CCD. Figure 2.6 shows the effect of electrode bias on the energy bands of the underlying silicon. With no applied voltage the Fermi level, E_F, is the same in the semiconductor and the metal. When a voltage is applied to the electrode the potential drops across the junction. Band bending occurs in the semiconductor as the E_F level stays flat as no current flows. If the bias voltage is made more negative the valence band bends nearer to E_F resulting in an increased concentration of majority carriers, holes in the case of p-type silicon, developing near the Si-SiO_2 interface. This situation is called 'accumulation'. For small positive bias the valance band bends away from E_F creating a region depleted of majority charge carriers. The depth of this region into the silicon increases as the applied voltage is increased. This situation is called 'depletion'. For large positive bias the intrinsic level bends below E_F and minority carriers accumulate at the interface while majority carriers are removed by a substrate connection. This situation is therefore called ‘inversion’. If the bias is increased further to the point where the conduction band crosses E_F, ‘strong inversion’, the number of majority carriers at the surface becomes very high. The bulk silicon is shielded from the applied bias and no further increase in the depletion depth can be made.

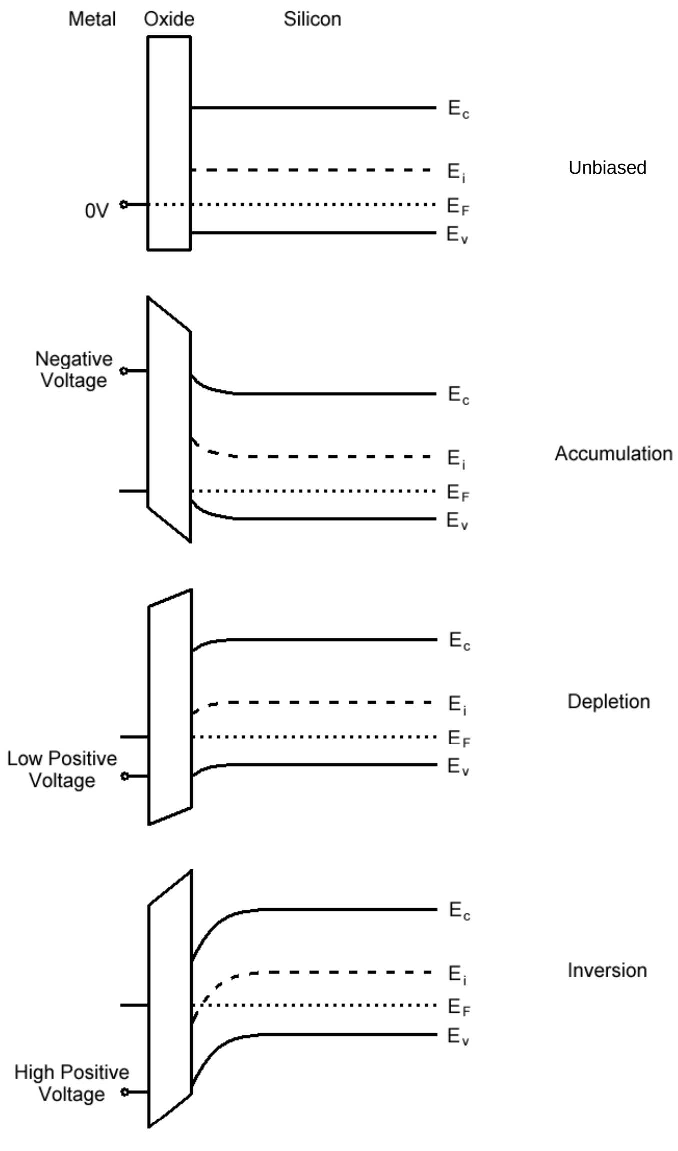

Figure 2.6 The effect of electrode bias on the energy bands of the underlying silicon

The potential profile in the depletion region of a uniformly doped p-type silicon CCD is related to the dopant concentration, N_A, by Poisson's equation:

$$\frac{d^2V}{dx^2} = \frac{qN_A}{\varepsilon_{Si}\varepsilon_0} \tag{2.1}$$

Where q is the electronic charge, ε_{Si} is the relative permittivity of silicon and ε_0 is the relative permittivity of free space. Integrating equation 2.1 with the boundary condition that the electric field is zero at the depletion depth D, gives a linear expression for the electric field into the device:

$$\frac{dV}{dx} = \frac{qN_A}{\varepsilon_{Si}\varepsilon_0}(x - D) \tag{2.2}$$

Integrating equation 2.2 with respect to x gives an expression for how the potential changes with distance, x, into the silicon:

$$V = \frac{qN_A}{2\varepsilon_{Si}\varepsilon_0}(x - D)^2 \tag{2.3}$$

At the silicon surface $V = V_S$ and $x = 0$, giving an expression for the relationship between the depletion depth and the surface potential:

$$V_S = \frac{qN_A D^2}{2\varepsilon_{Si}\varepsilon_0} \tag{2.4}$$

Therefore:

$$D = \sqrt{\frac{2\varepsilon_{Si}\varepsilon_0 V_S}{qN_A}} \tag{2.5}$$

Figure 2.7 shows the potential profile of a surface channel device with a 0.2 μm oxide layer on silicon with a dopant concentration of 1×10^{15} cm^{-3} with 10 V applied to the gate electrode (Holland 1990). Figure 2.8 shows the potential profile under two electrodes of a surface channel device modelled using the EVEREST Device Modelling Software for Charge Generation Events (Fowler et al. 1998).

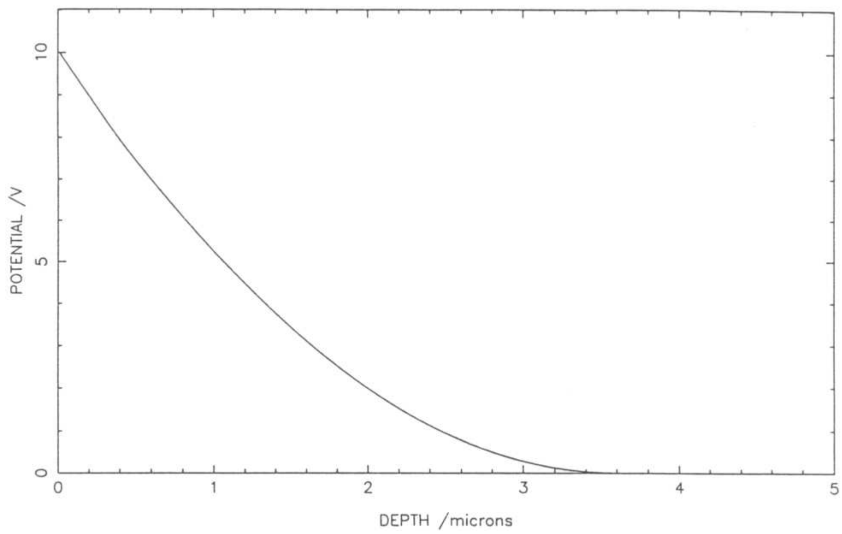

Figure 2.7 The potential profile of a surface channel device

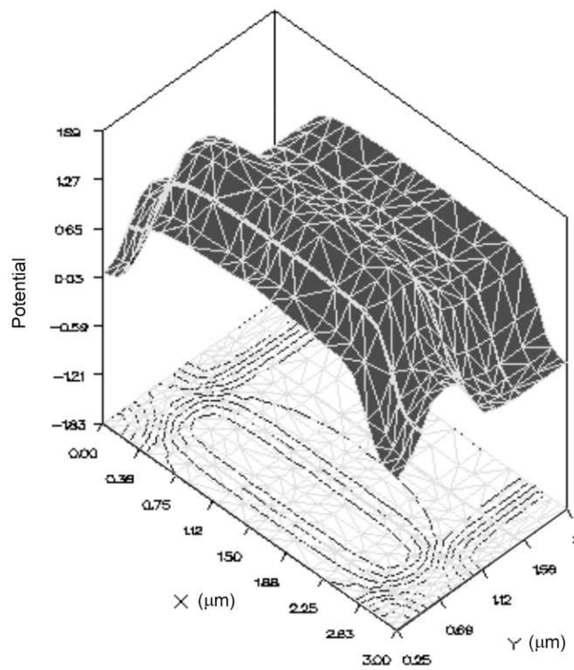

Figure 2.8 The potential profile under two CCD electrodes in a surface channel device, one biased, one unbiased, modelled using the EVEREST Device Modelling Software for Charge Generation Events (Fowler et al. 1998)

2.3.2. The Buried Channel Device

In the buried channel CCD, when a potential is applied to the n layer a depletion region is formed. The depletion layer at the p-n junction between the n-type buried channel implant and the p-type underlying epitaxial silicon, grows as the applied electrode voltage is increased. A point arises where the depletion layers meet and any further bias on the n layer has no further influence on the potential profile. This condition is called ‘pinch-off’ and results in the creation of a potential maximum ~0.5 μm below the Si-SiO_2 interface. Any increase in electrode bias will increase the depth of the depletion region into the silicon but the potential minimum remains in the same place. Solving Poisson’s equation numerically for different applied bias produces the plot in Figure 2.9. The solid and dashed lines represent the potential profile under electrodes held at 10 V and 0 V respectively, the dotted line showing the potential profile under an intersection of both the channel stop and the 10 V electrode and the p+-type isolation columns (Holland 1990).

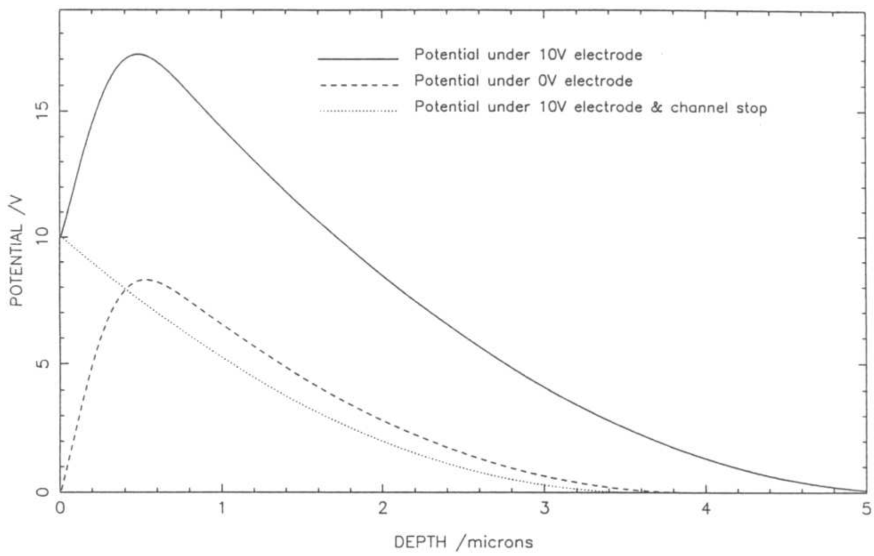

Figure 2.9 The potential profile of a buried channel device

2.4. Charge Transfer

Charge collected under the bias electrode of each pixel in the CCD is first moved down the columns of the device by a series of 'clocking' pulses. This transfer is known as 'parallel' transfer and is brought about by sequencing the bias of the electrodes in each pixel. One cycle results in all the charge packets moving down one row, the first packet moving into the readout register which has one bias electrode held high to preserve the horizontal information. Figure 2.10 shows a clocking sequence transferring charge from under one electrode to another. In the initial stages of transfer, the charge is moved by self induced drift brought about by the charge distribution concentration gradient. Once the charge distribution becomes more uniform the fringing-field between the electrodes becomes the dominant influence on charge movement (Hsieh and Luk 1984). A final factor influencing the flow of charge is thermal diffusion that may have an effect in low field regions (Banghart et al. 1991).

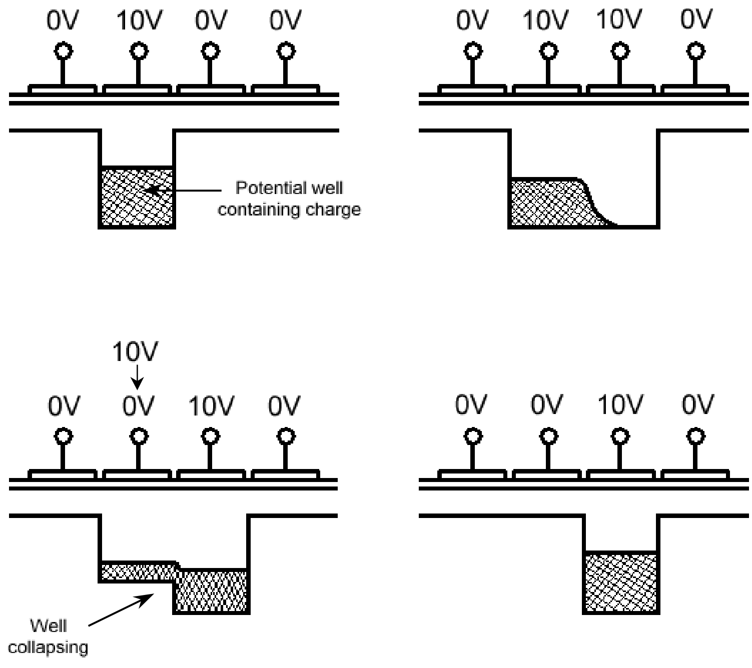

Figure 2.10 The charge transfer process

2.4.1. Charge Transfer Efficiency

For scientific imaging CCDs it is important to have good Charge Transfer Efficiency, CTE. A reduction in CTE is caused by insufficient transfer time and by trapping of charge that is released into following signal packets. The effect of bad CTE is seen as smearing of the sources in a CCD image in the direction of charge transfer. The energy resolution of a device is also affected by bad CTE, the deferment of charge from the source pixel leading to a broadening of the observed spectral lines. When describing the transfer efficiency of a device numerically, it is useful to talk about Charge Transfer Inefficiency, CTI, which is the fraction of total charge left behind after transfer from one pixel to another, where:

$$CTI = 1 - CTE \tag{2.6}$$

Given suitable charge transfer time, CTI is dependent on the trapping and release time constants of electrons and holes from the trapping sites, governed by Shockley-Reed-Hall theory (Shockley and Reed 1952). In a buried channel device with a charge packet residing in the n layer, hole capture can be omitted. The traps below mid-band are always occupied due to long electron emission time constants and the traps above mid-band have long hole emission time constants. For these reasons only the traps above mid-band are of interest where electron capture and emission is dominant. Electron capture and emission is described by:

$$\frac{dN_{trapped}}{dt} = \underbrace{\sigma_n v_{th} n_e \left(N_t - N_{trapped}\right)}_{\text{capture}} - \underbrace{\sigma_n v_{th} N_c N_{trapped} \exp\frac{-E}{kT}}_{\text{emission}} \tag{2.7}$$

Where $N_{trapped}$ is the number of trapped electrons at an energy level E below the conduction band edge, σ_n is the electron capture cross-section, v_{th} is the electron thermal velocity, n_e is the density of electrons in the conduction band, N_t is the density of traps, N_c is the density of states in the conduction band, k is the Boltzmann constant and T is the temperature. The electron capture and emission time constants are therefore given by:

$$\tau_{capture} = \frac{1}{\sigma_n v_{th} n_e} \qquad \tau_{emission} = \frac{\exp\left(\frac{E}{kT}\right)}{\sigma_n v_{th} N_c} \tag{2.8}$$

The electron capture time constant is dominated by the electron capture cross-section, while the emission time constant is dominated by the trap energy level and temperature. In a steady state, the fraction of traps filled, *Γ*, in a time, Δ*t*, is given by (Bond 1996):

$$\Gamma = \frac{1}{\left(1 + \frac{\tau_{capture}}{\tau_{emission}}\right)}\left[1 - \exp\left(\frac{-\Delta t}{\tau_{capture}}\right)\exp\left(\frac{-\Delta t}{\tau_{emission}}\right)\right] \tag{2.9}$$

The electron trapping time is ~10 - 100 ns while the release time is dependent on the trap species and can be of order a few 10’s of nanoseconds to seconds. If the release time is slow in comparison to the pixel transfer time, charge smearing will be seen in the CCD image. Figure 2.11 shows the effect of CTE on the signal charge packet.

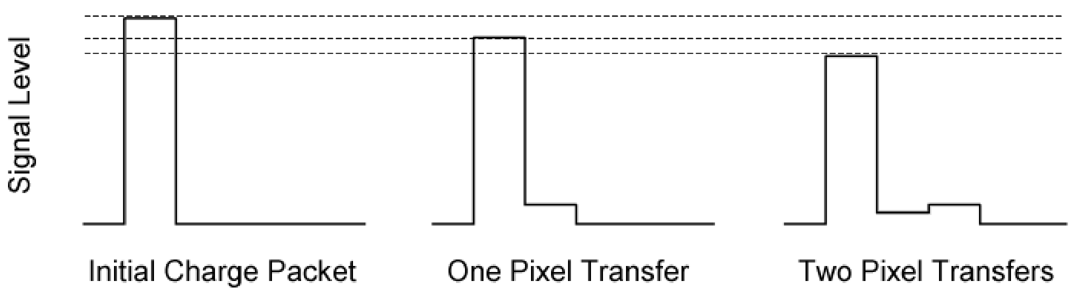

Figure 2.11 The effect of CTE on a charge packet. Signal charge is lost from the initial charge packet during transfer and is emitted into subsequent pixels

2.5. Charge Readout

After transfer of a CCD row into the orthogonal serial readout register, each charge packet in the row is clocked onto an output node for amplification and readout. The end of the serial register and the output circuit are shown in Figure 2.12. A number of methods of readout exist but the method employed by the CCDs used for the work in this thesis is as follows:

The reset FET is turned on allowing the output FET to be set to a reference voltage level. The reset FET is then turned off while the bias on the last electrode in the serial register, the output gate, is lowered allowing the charge packet to pass to the output node. The output node is of n-type silicon and biased to form a deep potential well for collecting the signal charge. As the signal charge is transferred to the output node, the voltage of the output FET, V_{FET}, changes in proportion to the number of electrons in the charge packet, if the output transistor is operated in its linear region. This relationship is given by:

$$\Delta V_{FET} = \frac{\Delta Q}{C_T} G_{FET} \tag{2.10}$$

Where ΔQ is the signal charge level, C_T is the total output FET capacitance (usually ~10 fF for low noise CCDs) and G_{FET} is the gain of the output FET (usually ~0.7). This readout process is repeated for each pixel of the CCD. Usually a value of 1-6 μV per electron is obtained.

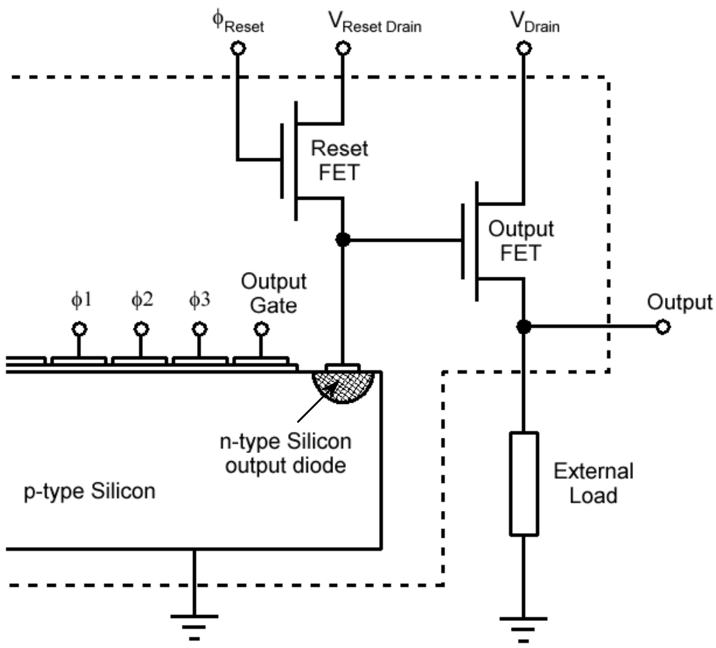

Figure 2.12 A typical CCD readout register and output circuit

2.6. CCD Noise

The main components of CCD noise are discussed in detail by Beynon and Lamb (1980), Howes and Morgan (1979) and Robbins (1992). The total CCD noise figure is the quadrature sum of the following sources:

2.6.1. Photon Shot Noise

The mean number of electron hole pairs, n_{eh}, created in silicon for a given incident X-ray photon of energy, E_γ, is:

$$n_{eh} = \frac{E_\gamma}{\omega} \tag{2.11}$$

Where ω is the energy required for generation of a single electron-hole pair. For silicon ω is 3.68 eV at -100 ^{o}C and 3.65 eV at room temperature (Bertolini and Coche 1968). This value is higher than the silicon band-gap energy of 1.12 eV as phonons are produced as well as electron-hole pairs. The statistical variation of n_{eh} given by Poissonian statistics is higher than the observed variation. The difference is due to secondary electron-hole pair generation not being independent and an empirical modifier to the Poissonian value, called the Fano factor, F, needs to be included (Fano 1947). The photon shot noise is therefore given by:

$$\sigma_{shot} = \sqrt{Fn_{eh}} = \sqrt{\frac{FE_\gamma}{\omega}} \tag{2.12}$$

To enable X-ray spectroscopy, the overall CCD system needs to have a noise level not much greater than this Fano-Limited value. F is usually taken to be 0.115 (Alig et al. 1980).

2.6.2. Reset Noise

Due to thermal noise in the reset potential. At -90 ^{o}C the reset noise can be ~100 electrons. The reset noise is given by:

$$\sigma_{reset} = \frac{\sqrt{kTC_T}}{q} \tag{2.13}$$

This source of noise can be removed by use of Correlated Double Sampling, CDS, where the reference voltage is measured and averaged over a finite time both before and after charge is clocked onto the output node, the difference between the two levels being the signal charge component (Hopkinson and Lumb 1982).

2.6.3. Transistor Noise

Due to thermal motion of charge carriers, 'Johnson' noise, and the trapping and release of electrons in the conductive drain to source channel of the output FET, 'flicker' noise. Flicker noise is also known as '1/f' noise due to its spectral distribution which is proportional to $1/f^{\alpha}$, where α is close to unity (Sze 1981). Both sources of transistor noise can be optimised by accurate CDS methods (Hopkinson and Lumb 1982).

2.6.4. Transfer Noise

Due to loss of signal charge to trapping sites. For small losses the transfer noise is given by:

$$\sigma_{CTI} = \sqrt{N_e N \varepsilon} \tag{2.14}$$

Where N_e is the number of electrons in the signal packet, N is the number of transfers and ε is the CTI.

2.6.5. Dark Current

Due to thermal excitation of electrons into the conduction band. These electrons will become added to the signal charge packet introducing a noise component that is dependent on the intrinsic carrier concentration, n_i, and therefore temperature. Electrons can be thermally excited into the conduction band from three locations within the CCD: from the depletion region, from the bulk silicon field-free region and from the Si-SiO_2 interface. The total dark current, I_d, is given by (Sze 1981):

$$I_d = \underbrace{\left(\frac{qn_i}{2\tau}\right)D}_{\text{Depletion region}} + \underbrace{\left(\frac{qD_n}{L_n N_A}\right)n_i^2}_{\text{Field-free region}} + \underbrace{\frac{qsn_i}{2}}_{\text{Si-O}_2\text{ interface}} \tag{2.15}$$

Where τ is the effective lifetime in the depletion region, D_n is the diffusion constant, L_n is the electron diffusion length and s is the surface recombination velocity. The dark current components from the depleted region and the interface have a temperature dependence of $\exp\left(-E_{Si}/2kT\right)$, where E_{si} is the silicon band-gap energy of 1.12 eV. The temperature dependence of the dark current component from the field-free region is $\exp\left(-E_{Si}/kT\right)$. The dominant component of the total dark current is from the interface region.

It is common practice to operate scientific CCDs at a low temperature to reduce the dark current contribution to the overall CCD noise figure. Operation of a CCD at -90 ^{o}C has been demonstrated to reduce the dark current by 3×10^{-6} (Chowanietz 1987). The use of 'inverted mode' operation also reduces the dark current by suppressing the contribution from the interface region. The surface of the device is put into inversion, allowing the accumulation of holes at the interface, which then combine with thermally generated electrons from interface generation sites, reducing the dark current by a factor of >100. Dark current is discussed in more detail in Chapter 3.

2.7. Photon Detection

Accounting for the electrode structure and oxide layers above the bulk silicon, a CCD is an efficient detector in two distinct energy bands. These bands fall in the visible wavelength range, 4000 Å to 10000 Å and the X-ray wavelength range, 1 keV to 5 keV. The absorption efficiency of silicon at different wavelengths is shown in Figure 2.13. When an X-ray photon interacts with the bulk silicon of the CCD a cloud of electron-hole pairs is produced as a result of ionisation. This is a threshold process that has a weak temperature dependence. At room temperature the ionisation energy is ~3.65 eV increasing to ~3.72 eV close to absolute zero (Bertolini and Coche 1968). The number of electron-hole pairs produced by ionisation is therefore proportional to the incident photon energy for energies above a few eV.

Optical photons are of a relatively low energy and interact with electrons in the valence band of the silicon, promoting electrons to the conduction band via the photoelectric effect. In this way a single electron is generated for each incident optical photon. The electrons can then move freely in the silicon to be collected in the potential wells under biased CCD electrodes, the number of electrons in a given pixel being proportional to the intensity of the incident radiation.

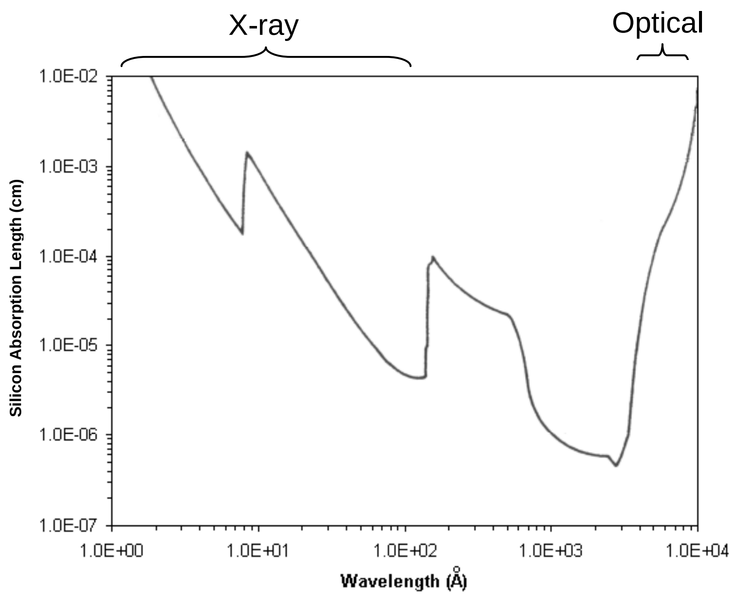

Figure 2.13 The absorption length of electromagnetic radiation in silicon

If an incident photon imparts some of its energy directly to a silicon atom, it may excite an electron in the K-shell, expelling it from the atom. The emitted electron will have the same energy as the incident photon, minus the silicon K-shell binding energy of 1.84 keV. The atom then de-excites by transfer of an outer shell electron to the K-shell, releasing a fluorescence X-ray, or by Auger and non-radiative processes. Fluorescence X-rays in silicon have an energy of 1.7 keV and are absorbed by ~10 μm of silicon, before they can travel into an adjacent CCD pixel contributing to the escape peak in the X-ray spectrum.

2.7.1. Charge Spreading

Electrons liberated in the depletion region of the CCD are collected under the biased electrode in each pixel, forming the signal packet, while holes are swept away by the electric fields. In the field free region charge spreading occurs before the electrons are pulled into the buried channel. This process may result in some electrons being collected in surrounding pixels and not the interaction pixel causing a distortion in the CCD image. When observing a spectrum recorded by a CCD it is usual to consider only 'isolated events', pixels with no charge in the adjacent pixels, to get the best spectral resolution. A spectrum of 'all events' will increase the width of the spectral features as a result of charge spreading, degrading the resolution. One technique of increasing the spectral resolution is to use software that recognises 'split-pixel' events and sums the charge in the central and adjacent pixels, recovering the incident photon energy information. The effect of charge spreading can be reduced by minimising the extent of the field free region of the device.

2.7.2. Quantum Efficiency

The efficiency of a CCD to detect photons of different wavelength is called the 'quantum efficiency', QE. The QE at a given energy, *E*, is given by:

$$QE(E) = T_{electrode}\left(1 - e^{-\mu x}\right) \tag{2.16}$$

Where $T_{electrode}$ is the transmission of the electrode structure, μ is the absorption coefficient of silicon and x is the thickness of the epitaxial silicon layer of the device. An example of a CCD QE curve for a CCD22 open electrode device optimised for X-ray spectroscopy is shown in Figure 2.14. The absorption edges are due to photons being absorbed by electrons in the inner shells of the silicon atom. The absorption edges are also where the quantum mechanical nature of the photoelectron causes variations in the QE attributable to absorption fine structures (Keay 1997).

The QE at low energy is decreased as photons are absorbed by the electrode structures before passing into the bulk silicon of the device where the charge generated can be collected. An improvement in the low energy QE can be achieved by 'back illumination' of a device (Shortes et al. 1974). This involves thinning the bulk silicon on the back of the CCD down to the depletion layer boundary during fabrication. The resulting device can be back illuminated with low energy photons being absorbed in the bulk silicon after passing through a dead layer of only ~50 nm, improving the QE. An example QE curve for a back illuminated device is also shown in Figure 2.14. Other methods of improving the low energy QE are use of thin and open electrode structures (Castelli 1991, Holland et al. 1993). The high energy QE can be improved by using a higher atomic number material as the detector, for example GaAs, or in the case of the silicon CCD, increasing the depletion depth by using higher resistivity silicon.

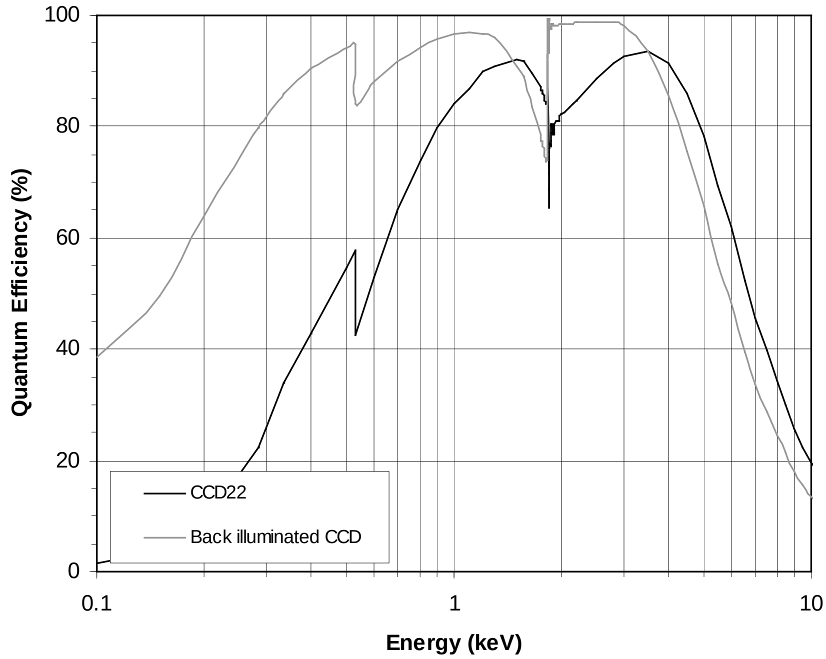

Figure 2.14 Quantum efficiency of an E2V Technologies CCD22 open electrode device (Short 2002). The quantum efficiency of a back illuminated device is also shown for comparison

The ‘response matrix’ of a CCD describes the probability distribution of the CCD channel in which a photon of a given energy will be measured. An example of a modelled response matrix for an E2V Technologies CCD12 device is given in Figure 2.15. The grey scale of the figure is a logarithmic scale and represents the QE for a given photon energy and CCD channel. A logarithmic scale is used to emphasise the second order loss effects.

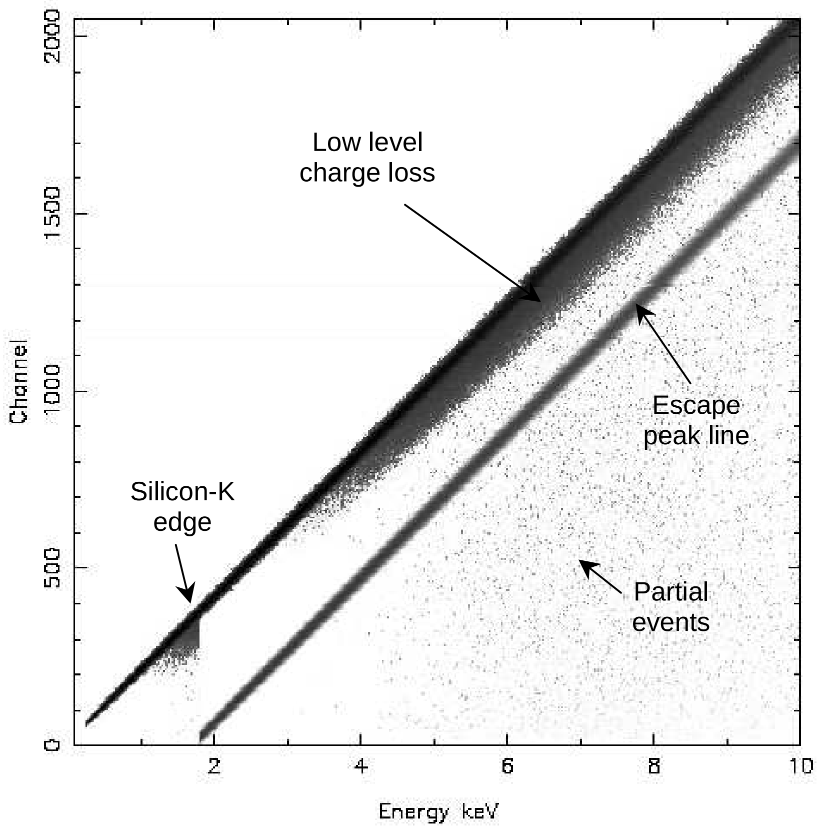

Figure 2.15 An E2V Technologies CCD12 response matrix depicting the signal level in channels, for a given input photon energy

2.7.3. Spatial Resolution

The spatial resolution of a CCD is described by the 'modulation transfer function', MTF. The modulation depth is the difference in charge level between two sources, and the minimum charge level between them. The MTF is the relationship of the modulation depth to the image spatial frequency. The MTF is degraded by charge transfer losses and also by charge spreading. A good quality astronomical CCD needs sources to be separated by more than two pixels to have a high MTF.

2.7.4. Energy Resolution

The energy resolution of a CCD is described by the 'full width at half maximum', FWHM of a spectral feature. For a cooled CCD with good CTE, the FWHM is given by:

$$FWHM = 2.35\omega\sqrt{\sigma_{total}{}^{2} + \frac{FE_{\gamma}}{\omega}} \qquad (2.17)$$

Where σ_{total} is the total CCD readout noise in electrons. Typically σ_{total} is ~10 electrons giving a FWHM of ~140 eV for the ^{55}Fe Kα peak.

2.8. Summary

This chapter has described the CCD manufacturing process and presented the underlying physics governing charge storage, charge transport and charge readout of a device. Both surface and buried channel devices have been described, buried channel devices featuring in the work carried out for this thesis. The various sources of noise involved with CCD operation have also been discussed along with the definition of several important terms used to describe the operating characteristics of a device. The next chapter goes on to describe the various components of the space radiation environment and the effects this environment has on the operational characteristics of CCDs.

Chapter 3: The Space Radiation Environment and its Effects on CCDs

This chapter describes the near Earth space radiation environment and its effects on the operational characteristics of CCDs. The different components of the space radiation environment are described, followed by a detailed discussion of the radiation damage mechanisms relevant to CCDs and their resulting effects on CCD operation.

3.1. Introduction

For the operation of CCDs on scientific satellites and spacecraft, it is necessary to have an understanding of the radiation environment the devices will experience during their lifetime and to have a thorough understanding of the effects this environment will have on the operational characteristics of the devices. This chapter will first discuss the various components of the space radiation environment and then describe the two radiation damage mechanisms relevant to CCDs; ionisation and displacement damage. After presenting the underlying physics behind the two damage mechanisms, the effects of radiation damage on CCD operation are described in detail, along with techniques and methods of reducing radiation damage; 'radiation hardening'. A number of models used to simulate both the space radiation environment and radiation damage effects in CCDs are also discussed in this chapter.

3.2. The Space Radiation Environment

The different components of the space radiation environment are discussed in detail by Holmes-Siedle and Adams (2002). What follows is a brief summary of the main space radiation components that influence CCDs onboard spacecraft orbiting the Earth. The effect of geomagnetic and spacecraft shielding on the radiation fluxes received by a CCD are then discussed, along with an overview of some of the modelling tools available for calculating total accumulated spacecraft radiation fluxes.

3.2.1. Radiation Belts

The radiation belts consist of protons up to a few hundreds of MeV and electrons up to a few MeV that have become trapped in the Earth's magnetic field while they were travelling through the solar system. The belts were discovered by Van Allen in 1958 (Van Allen and Frank 1959) and are described in detail by Hess (1968). The trapping of protons and electrons occurs where the magnetic field lines come close together and is dependent on the incoming particle's energy and angle of incidence. Once trapped the particles spiral around the magnetic field lines bouncing back and fourth between the magnetic poles. The final component of trapped particle motion is a longitudinal drift around the Earth, electrons drifting east and protons drifting west. Figure 3.1 illustrates the motion of a charged particle trapped in the Earth's magnetic field. The channelling of particles down into the atmosphere by the strong magnetic field regions above the north and south poles gives rise to colourful aurorae, their colours caused by electrons colliding with molecules in the atmosphere.

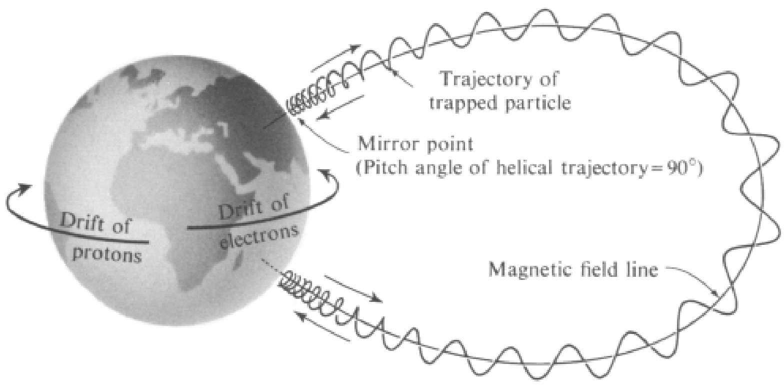

Figure 3.1 The motion of charge particles trapped by the Earth's magnetic field (Hess 1968)

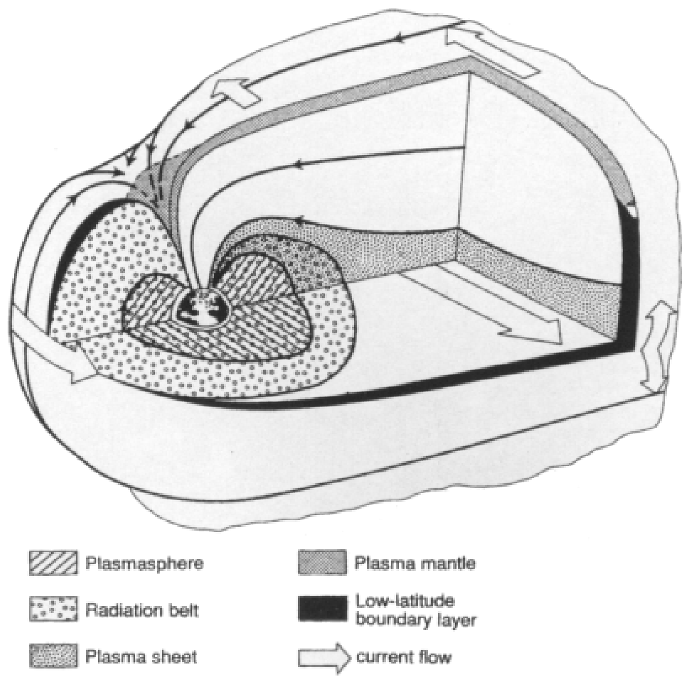

Figure 3.2 The Earth's magnetosphere and radiation belts (Daly 1989)

Figure 3.2 shows the ‘bow wave’ form of the Earth’s magnetosphere and the regions where particles become trapped forming the radiation belts. The asymmetrical form of the magnetosphere is a result of distortions caused by the solar wind, the ~11^{o} offset of the Earth’s magnetic axis from its rotational axis and also geological effects. The general shape and the distortions in the magnetic field create areas of increased trapped particle flux over the north and south poles, called the ‘auroral horns’.

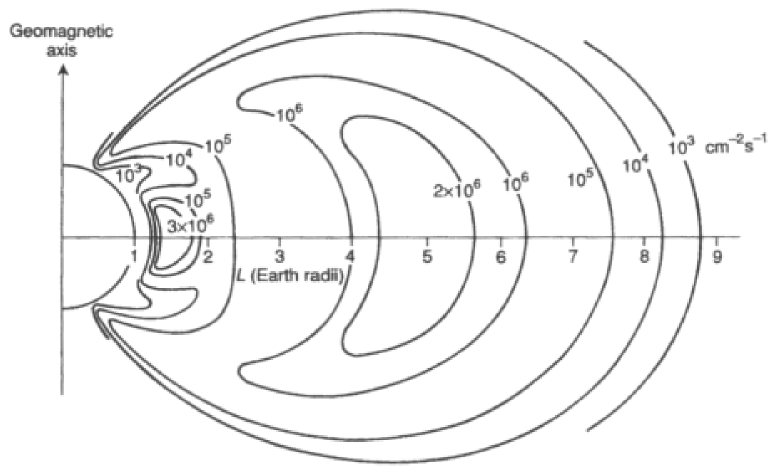

Figure 3.3 A radial profile of the trapped electron flux in the Earth’s radiation belts for electrons of energy above 1 MeV (Daly 1989)

Radial profiles of the proton and electron belts have been produced from a number of on-orbit measurements (Daly 1989). The trapped electron flux is highest in two altitude bands called the ‘inner’ and ‘outer’ zone maxima, shown in Figure 3.3. The inner zone contains electrons of energies up to ~5 MeV while the outer zone, with a flux around an order of magnitude higher, contains electrons of greater than ~7 MeV. The low flux area between the inner and outer zone is called ‘the slot’. The highest concentration of protons is found at lower altitude, shown in Figure 3.4. Unlike the trapped electrons, the trapped protons do not form distinct zones. The proton flux varies inversely with distance from Earth and monotonically with energy (Stassinopoulos and Raymond 1988). The variation of the electron and proton fluxes with particle energy are shown in Figures 3.5 and 3.6 respectively, for a low Earth orbit of inclination 60^{o} at 300 km and 500 km.

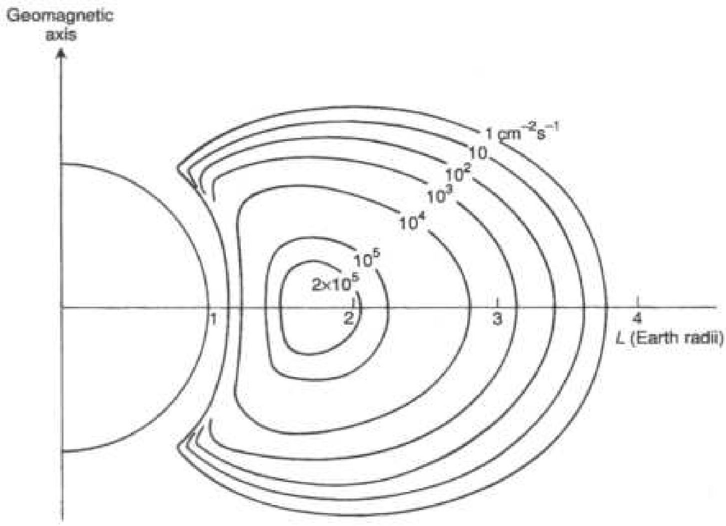

Figure 3.4 A radial profile of the trapped proton flux in the Earth's radiation belts for protons of energy above 10 MeV (Daly 1989)

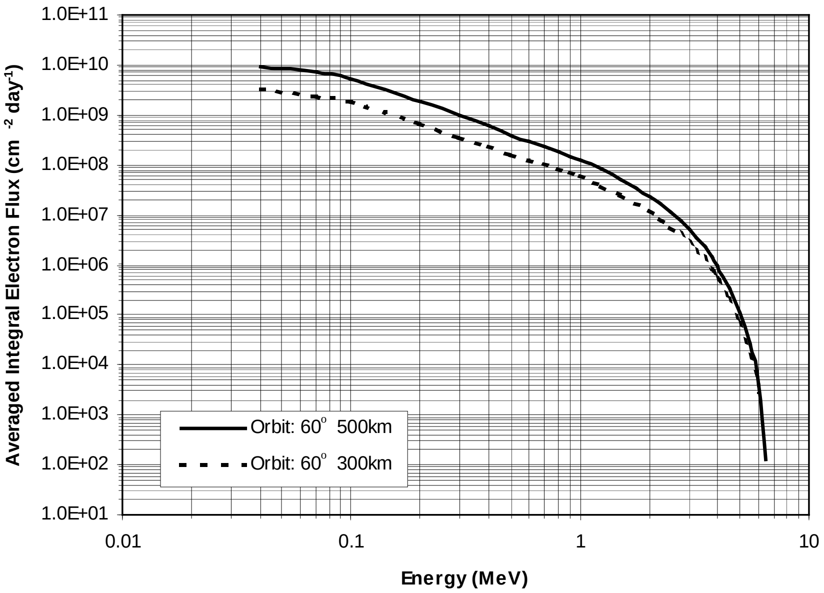

Figure 3.5 Variation of the trapped electron flux with particle energy in the Earth's radiation belts modelled by AE8

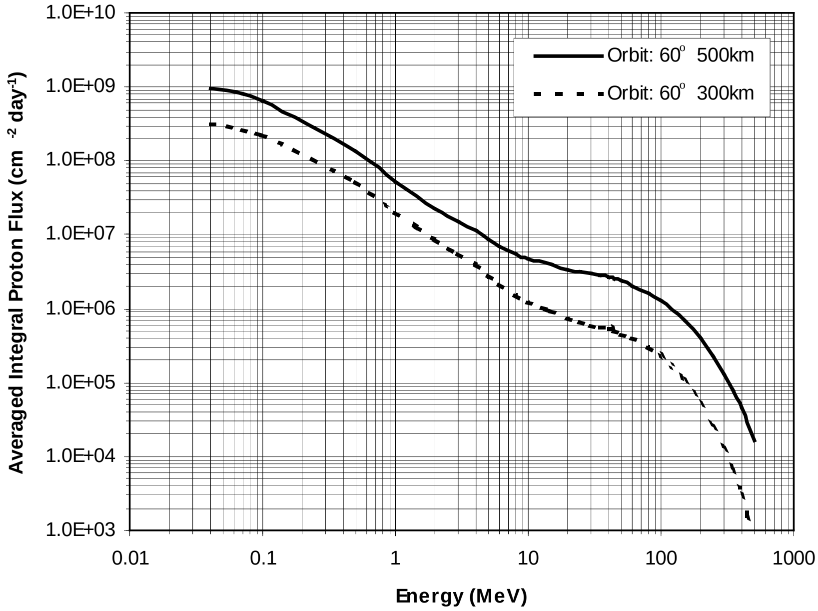

Figure 3.6 Variation of the trapped proton flux with particle energy in the Earth's radiation belts modelled by AP8

For a spacecraft orbiting the Earth it is important to spend as little time in the radiation belts as possible as the total incident spacecraft radiation flux is strongly dependent on the orbital parameters. Low Earth orbits with inclination >45^o will pass through the auroral horns and be subjected to the trapped particle environment (Stassinopoulos and Raymond 1988).

3.2.1.1. The South Atlantic Anomaly

In the same way the Earth's magnetic field creates the auroral horns, a magnetic anomaly is responsible for increasing particle fluxes by a factor >100 in a region over the South Atlantic. This region is known as the South Atlantic Anomaly, SAA. Figure 3.7 shows a 500 km altitude contour plot of proton fluxes >50 MeV over the South Atlantic, revealing the dipping of the proton belt towards the Earth's surface in this region. The SAA is important not only for satellites in low Earth orbit, but also for the many spacecraft launched that pass through the SAA on route to their final destinations. The SAA and aroural horns can only be avoided by satellites in low Earth orbits of inclination <15^o (Stassinopoulos and Raymond 1988).

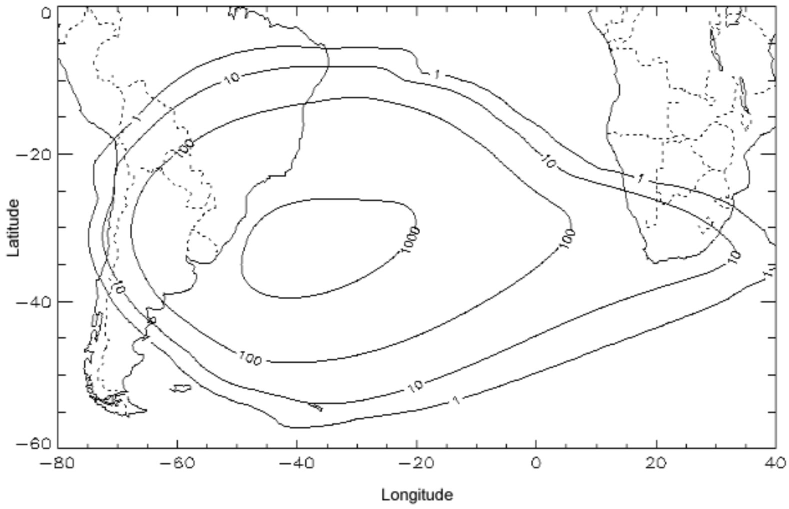

Figure 3.7 A 500 km altitude contour plot of proton fluxes >50 MeV produced by the AP8 radiation model showing the dipping of the proton belt in the South Pacific forming the SAA

3.2.2. Solar Wind

The lighter elements in the Sun's corona have enough energy to be ejected out into space forming the 'solar wind' (Parks 1991). The ejected particles consist mainly of protons and electrons of a few keV and their flux is inversely proportional to the distance from the Sun squared and may vary by a factor ~20 dependent on the 11 year solar cycle. Beyond the magnetosphere the solar wind can be of considerable flux that can cause spacecraft charging.

3.2.3. Solar Events

Energetic protons, heavy ions and electrons up to MeV energies can be ejected into space by the Sun as a 'solar event' (Tranquille 1994). The flux of particles emitted is intermittent and dependant on the solar cycle making it difficult to predict the future occurrence of solar events. Figure 3.8 shows solar event and sun spot activity over 3 solar cycles. A solar event takes around 8 minutes to reach the Earth and can last for a few hours to a few days in duration. The protons in a solar event are of lower energy than the trapped protons in the Earth's radiation belts, but they can have much higher total fluence levels. For spacecraft orbiting beyond the radiation belts, for example in geostationary, highly eccentric or planetary orbits, a substantial part of the total spacecraft radiation flux will be caused by solar events.

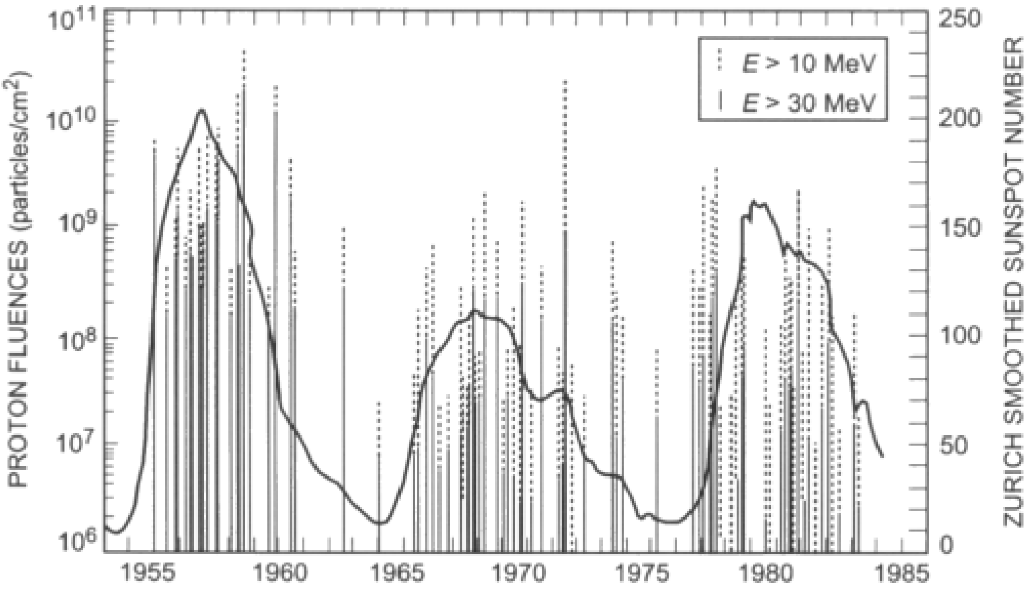

Figure 3.8 Monthly Solar event and sunspot activity over 3 solar cycles (Goswami et al. 1988)

3.2.4. Cosmic Rays

Cosmic rays are highly energetic charged particles originating from three possible sources:

- Galactic: These particles come from outside our solar system emitted from supernovae, pulsars and neutron stars. On passing through the galactic magnetic field the particles become diffuse and on arrival at Earth they are seen as a low isotropic flux. The particles are mostly protons with ~1 % heavier nuclei of up to TeV energies.

- Solar: These particles come from the Sun's chromosphere and are emitted in solar events. The composition of solar cosmic rays is different to that of galactic cosmic rays as a result of their different origin.

- Terrestrial: Galactic cosmic rays interact with the Earth's atmosphere causing secondary radiation to be emitted as a 'cosmic ray shower'. This secondary radiation is the main component of cosmic radiation at the Earth's surface.

The cosmic ray flux is attenuated by the solar wind and therefore is seen to vary with the solar cycle.

3.2.5. Geomagnetic and Spacecraft Shielding

A degree of protection from low energy radiation is provided by the Earth's magnetosphere (Daly 1994, Stassinopoulos and Raymond 1988). Cosmic rays and particles from the Sun need to have a minimum energy for penetration into the magnetosphere which results in the lower intensity of these particles nearer the Earth. The amount of shielding offered by the magnetosphere is dependent on the altitude and inclination of a spacecraft's orbit and also the intensity of the solar wind, which can compress the magnetosphere allowing particles to penetrate further. Geostationary and polar orbiting spacecraft will not experience any benefits of geomagnetic shielding as they are beyond or at the limits of the magnetosphere.

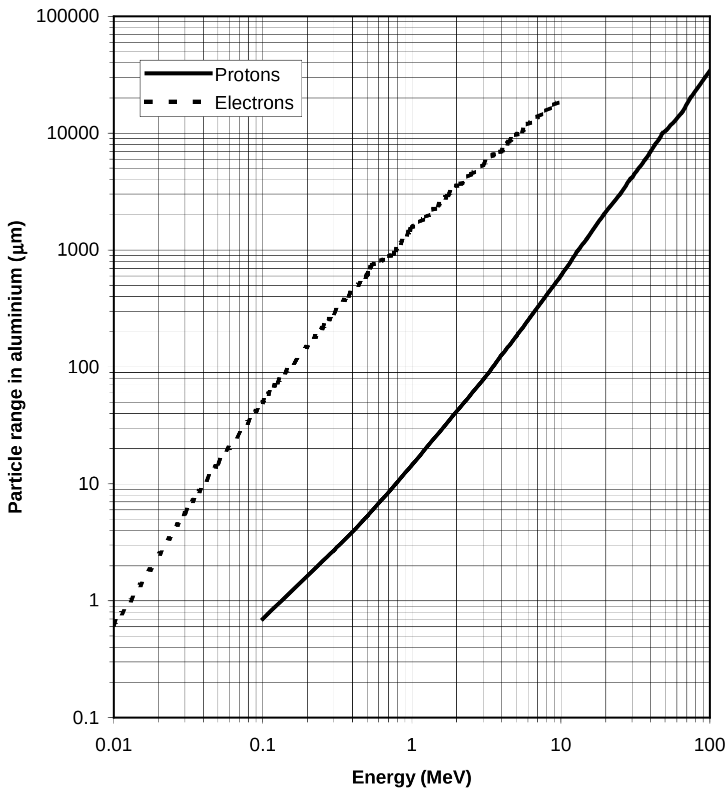

Figure 3.9 The range of protons and electrons in aluminium (Ziegler et al. 1985)

Physically shielding CCDs on a spacecraft by surrounding them with aluminium, or a high atomic number metal such as tantalum, is a common method used to reduce the expected total mission radiation fluence (Dale et al. 1993). The range of electrons and protons in aluminium is shown in Figure 3.9 (Ziegler et al. 1985). Electrons of up to ~5 MeV can be shielded out by ~5 mm of aluminium or equivalent thickness of spacecraft structure, for example any electronics or optics structure, greatly reducing the electron component of a spacecraft's total radiation fluence when orbiting within the radiation belts. Higher energy particles associated with solar events and cosmic rays are difficult to shield practically and are therefore an important factor when modelling the expected CCD radiation fluence. The use of spacecraft shielding also introduces a secondary radiation component where the energy and flux of the particles is changed through scatter and absorption in the shield material. This component also has to be considered when modelling CCD radiation fluence.

The CCD may be unshielded in the observation direction and for this reason the choice of orbit and orientation of the spacecraft are important. Some instruments, for example the X-ray Telescope onboard the NASA Swift Gamma Ray Burst Explorer satellite, employ the use of mechanical shutters that can be closed to prevent radiation entering the telescope that could cause damage to the detectors (Burrows et al. 2000), while another technique used by the EPIC instruments on the XMM-Newton satellite involves having a 'closed' position on the instrument's filter wheel (Turner et al. 2000). The use of shutters is a valuable way of protecting CCDs when travelling through high radiation flux areas, but does however introduce added complexity and mass to the spacecraft.

3.2.6. Modelling the Space Radiation Environment

To model the expected radiation fluence to be received by a CCD during a period in space it is necessary to have a model that will use the orbital parameters of the spacecraft, integrating the expected particle fluxes as the spacecraft travels around its orbit for the duration of its mission. The model needs to include information on trapped particles in the Earth's radiation belts, solar event particle fluxes, cosmic rays and the effects of spacecraft and geomagnetic shielding. One such model is the SPace ENVironment Information System, SPENVIS, which was developed by the European Space Agency in 1998 to incorporate several space radiation models into a single interface (Heynderickx et al. 2000). Orbital parameters are entered into the program and then required models are selected by the user for evaluation of the radiation environment over a specified mission duration. After selection of the spacecraft orbit, trapped proton and electron fluxes are predicted using the incorporated AP8 and AE8 models, along with a prediction of the solar proton fluence using either the King, JPL-85 or JPL-91 models. The effect of geomagnetic shielding can be included which computes an energy cut off dependent on the orbital parameters and solar cycle epoch, while the effect of different thicknesses of shielding around a CCD is modelled by SHIELDOSE. The SHIELDOSE model currently only incorporates aluminium shielding but is being expanded to include additional materials. The whole SPENVIS package can be used to obtain a first order approximation of the total radiation fluence expected to be received by a CCD during its operational lifetime.

The main drawback of using the computational models within SPENVIS results from the data the models are based on having been recorded many years ago, for example the AP8 and AE8 models use data from the 1960's which introduces large uncertainties. There is currently a drive to include more recent satellite data in the space radiation environment models and to use recent data to correct existing models. The Trapped Radiation ENvironment model Development project, TREND, has been initiated by the European Space Agency Technology Research Programme to improve upon the existing space radiation environment models of spacecraft orbiting around the Earth through the radiation belts (Lemaire et al. 1995).

Another problem with current radiation models is caused by the sporadic nature of the amplitude and frequency of solar events. Particles from solar events are hard to shield out due to their high energy spectrum, and hard to detect before causing damage to a CCD. Radiation models therefore generally incorporate either a single major solar event, or a specific number of events for a certain mission duration, giving a worst case estimate for the solar event particle flux.

3.2.7. The Non-Ionising Energy Loss Function

When discussing total proton fluence values it is useful to talk in terms of equivalent 10 MeV fluence, to allow the comparison of irradiation experiments carried out at different proton energies. The Non-Ionising Energy Loss function is a scaling factor that allows the amount of displacement damage caused by protons of different energies to be compared. The use of NIEL scaling for silicon devices has been described in detail by Burke (1986) and Van Lint (1987). The specific use of NIEL scaling in CCDs is discussed by Srour et al. (2003).

The form of the NIEL function is shown in Figure 3.10 and can be approximated by:

$$E_p < 13.5 \text{ MeV then} \qquad \text{NIEL} = \frac{8}{E_p^{\,0.9}} \tag{3.1}$$

$$E_p > 13.5 \text{ MeV then} \qquad \text{NIEL} = \frac{1.6}{E_p^{\,0.28}} \tag{3.2}$$

Where E_p is the incident proton energy in MeV.

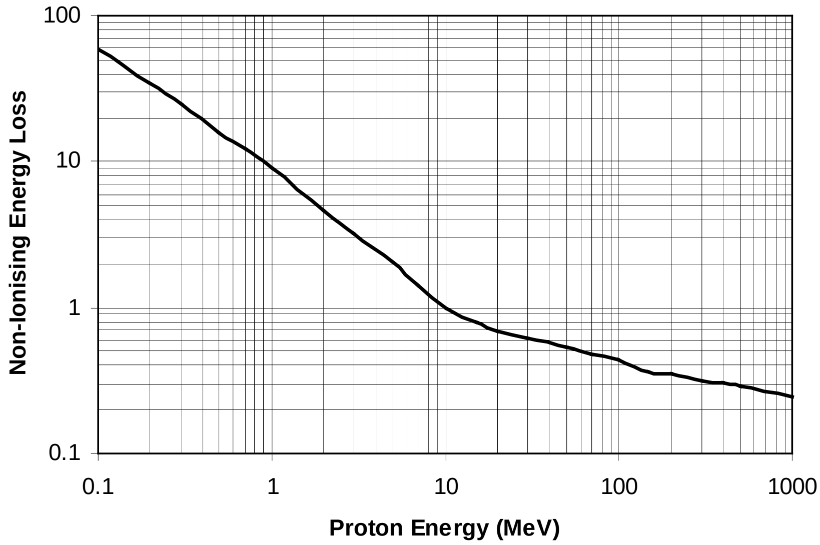

Figure 3.10 The Non-Ionising Energy Loss (NIEL) function

3.3. Radiation Damage Mechanisms in the CCD

The effect of radiation on silicon devices is discussed in detail in a number of books, for example Srour (1984), Larin (1968) and Holmes-Siedle and Adams (2002). The two damage mechanisms important for the study of radiation effects in CCDs are ionisation damage, affecting devices with oxide insulating layers, and displacement damage, which affects all semiconductor devices.

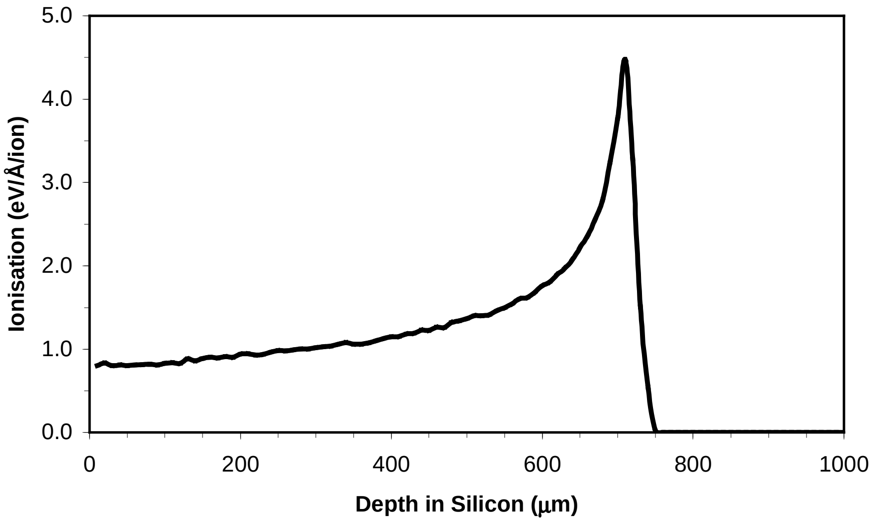

Figure 3.11 The amount of ionisation caused by a 10 MeV proton in silicon modelled using SRIM 2003

3.3.1. Ionisation Damage

Ionisation damage occurs when an incident particle can impart enough energy to an atom to excite an electron into the conduction band. As the particle travels through the CCD it leaves a trail of electron-hole pairs along its path. Figure 3.11 shows how the amount of ionisation caused by a 10 MeV proton varies with depth in silicon. This is a threshold process with an energy of ~3.65 eV required to excite an electron into the conduction band of a silicon atom and 18 eV for a silicon-dioxide atom (Emery and Rabson 1965). In the silicon of the device the holes are quickly removed by the electric fields and the electrons are collected in the potential wells under the electrodes where they become part of the signal charge. In the oxide and nitride insulating layers most electrons will recombine with holes but some carriers will be left to drift and diffuse through the lattice under the influence of the applied electric fields. The electrons are swept from the device while some of the holes will become trapped near the Si-SiO_2 interface where the concentration of impurity atoms is high. Impurity atoms in the silicon lattice have associated discrete energy levels that lie between the conduction and valence bands and it is here that carriers become 'trapped' (Grove 1967). The holes may be thermally excited and released from the shallow trap sites, drifting through the lattice again until becoming trapped at deeper levels. Holes trapped at a deep level will remain trapped for a longer period of time resulting in a change in the electric field potential at the Si-SiO_2 interface. The increase in positive charge by the accumulation of holes results in an increase in the observed leakage current of the device. If the device is unbiased during irradiation the electrons in the oxide and nitride layers are free to diffuse around allowing more recombination to occur and reducing the amount of leakage current generated (Robbins 1992). Figure 3.12 shows the amount of radiation induced charge that escapes recombination for different irradiation bias.

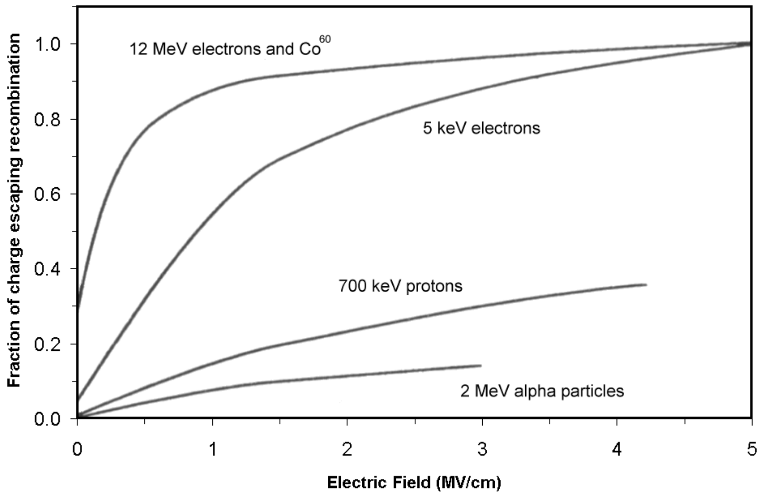

Figure 3.12 The amount of radiation induced charge escaping recombination at different irradiation bias levels (Robbins 1992)

3.3.2. Displacement Damage

Displacement damage is caused when an incident energetic photon, charged particle or neutron imparts enough energy to an atom to displace it from its lattice site (Messenger 1992). Atomic displacement is a threshold process requiring ~20 eV in silicon. The absence of an atom in the lattice is called a ‘vacancy’ and the displaced atom is called an ‘interstitial’ atom, the two components forming a ‘Frenkel pair’. If the displaced atom has enough energy, it may displace surrounding atoms creating a ‘defect cluster’. Neutrons with energies of a few MeV can cause cluster damage in silicon displacing hundreds of atoms, while MeV energy electrons and protons usually only impart enough energy to the target atom to cause an isolated defect. Figure 3.13

shows how the number of displaced atoms decreases with increasing incident proton energy. For low incident particle energies, energy is imparted to the target atom by Coulomb interaction. For incident particle energies ~10 MeV the energy is transferred by elastic scattering from the nuclear force field, while at energies of >100 MeV the transfer is by a nuclear inelastic process.

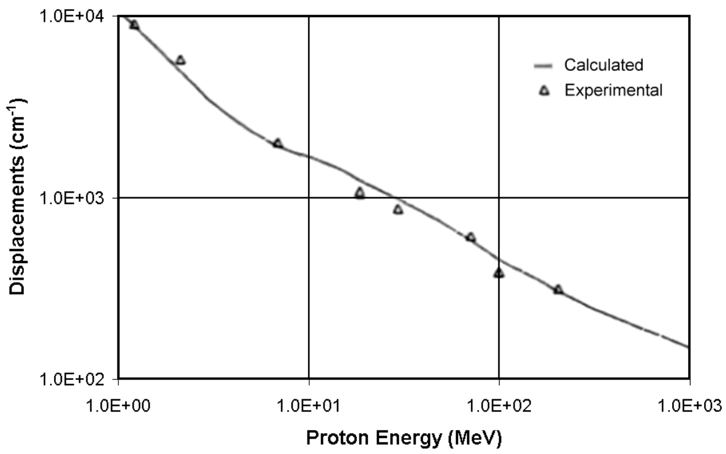

Figure 3.13 The number of atoms displaced by different energy protons in silicon (Van Lint 1987)

Defects in a CCD are also created during the manufacturing process which includes a high temperature, ~1000 ^{o}C, annealing phase to remove many of them. There are a number of known defects that can be present in CCD devices, each with a distinctive activation energy and annealing temperature, most of which can be annealed at around room temperature. Using activation energy and anneal temperature measurements the dominant defect centres can be determined.

The vacancies and interstitial sites created by displacement damage are not electrically active, but if they possess thermal energy >100 ^{o}K they can move through the crystal lattice and combine with other defects to create stable defect complexes. The defect complexes of importance in CCDs are illustrated in Figure 2.2, along with some of their properties. The three main complexes are the phosphorous-vacancy, the oxygen-vacancy and the divacancy although there are a number of other impurities that can form defects, including boron, carbon and aluminium atoms. The defects created have associated discrete energy levels, which lie within the silicon band-gap

(Grove 1967). These radiation-induced levels can give rise to five processes: recombination, generation, trapping, compensation and tunnelling. Any amount of each process can occur dependent on the carrier concentration, temperature and location in the device. Each of these processes is illustrated in Figure 3.14, and is described below:

- Recombination: Electron-hole pairs recombine at a rate dependent on the type of defect centre, reducing the minority carrier lifetime.

- Generation: Thermal generation of electron-hole pairs near the middle of the band-gap.

- Trapping: Carriers become trapped at shallow levels in the band-gap and can be re-emitted by thermal excitation. The rate of re-emission is dependent on the type of defect centre.

- Compensation: Reduction of the majority carrier concentration by carriers becoming trapped at lower level sites from donor sites just below the conduction band.

- Tunnelling: Carriers can tunnel through a potential barrier from the valence band to the conduction band. This process is only important where the electric field strength is greater than a few 10^7 V cm^{-1} and therefore does not cause a problem during usual CCD operation.

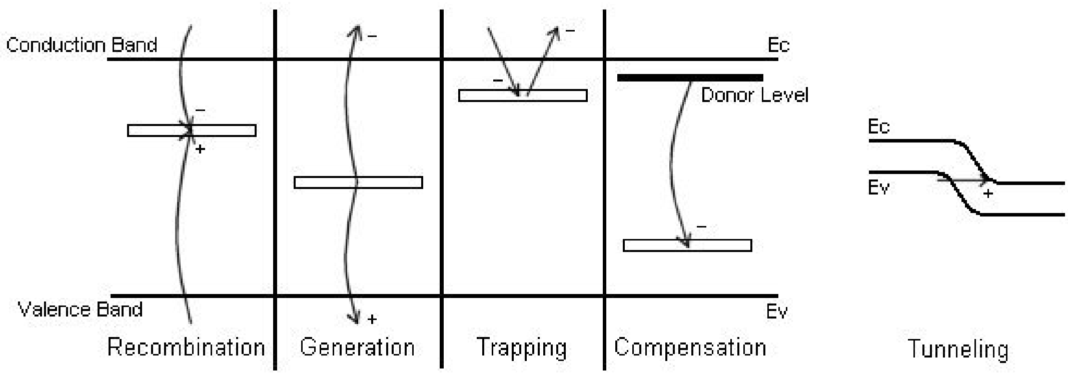

Figure 3.14 The possible effects of radiation induced levels in the silicon band-gap

3.4. The Effects of Radiation Damage on the CCD

Ionisation and displacement damage have a number of effects on the operational characteristics of the CCD that are described below. Methods of preventing and reducing the radiation damage caused to a device are also discussed.

3.4.1. Flat Band Voltage Shift

As a result of the increase in positive charge at the Si-SiO_2 interface caused by ionisation, the reset drain voltage has to be made more negative for the device to operate in the same manner. This change in threshold voltage is termed a 'flat band voltage shift'. Figure 3.15 shows the effect of oxide trapped charge on the potentials under the charge transfer electrodes and output structure of a CCD. The build up of positive charge does not effect the storage and transfer of collected charge because all the electrodes are affected similarly, the potential of the reset drain however has no insulator above it and therefore needs to be made more negative to compensate for the reduced electrode and output gate potentials (Roy et al. 1989). A flat band voltage shift reduces the charge handling capacity of the CCD and increases the device power requirement. If a large enough shift occurs as a result of ionisation damage the device may become inoperable. Figure 3.16 shows the flat band voltage shift resulting from a 50 krad proton irradiation of an E2V CCD01. The measurements were recorded by monitoring the current of the reset drain and recording at what point the current drops, indicating the point at which charge is no longer transferred.

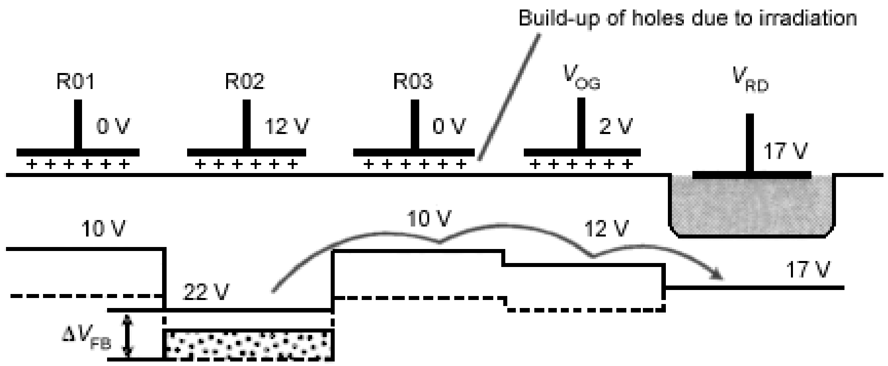

Figure 3.15 The effect of oxide trapped charge on the potentials under the charge transfer electrodes and output structure of a CCD (adapted from Roy et al. 1989)

Methods employed to reduce the required change in gate voltage caused by ionisation damage are called ‘radiation hardening’ techniques. Methods include thinning of the oxide layer reducing the number of trapping sites present (Shiono et al. 1983), high temperature annealing of the device during manufacture to remove a large fraction of the oxide trapping sites, use of a p-channel CCD structure where the holes are swept away from the Si-SiO_2 interface, and use of a planar insulator so the voltage shift is the same under all electrodes of the device. The injection of charge into a device has also been demonstrated as a successful method for ‘filling’ traps, removing the holes accumulated at the surface of the device. Charge injection is discussed in more detail below when describing methods to prevent CTI degradation. During CCD operation, reducing the operating temperature can reduce the level of ionisation damage induced leakage current by ‘freezing’ carriers in trap sites, increasing the carrier emission time constant.

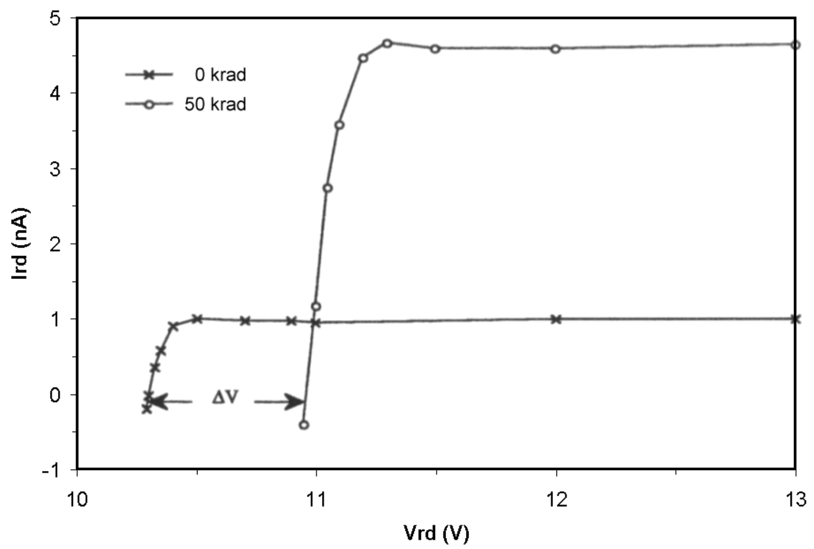

Figure 3.16 The flat band voltage shift resulting from a 50 krad proton irradiation of an E2V CCD01, where Vrd is the reset drain voltage and Ird is the reset drain current (Robbins 1992)

3.4.2. Increase in Dark Current

The increase in surface charge as a result of ionisation damage in a CCD results in an increase in the observed dark current of the device. An additional increase in the dark current results from the generation of carriers from radiation induced levels in the silicon band-gap. The generation rate equations for defects in the depleted and bulk regions of a CCD are discussed in detail by

Robbins (1992). The contribution to dark current from the depleted and bulk regions of the CCD are roughly equal, although in the depleted region it is the result of a large number of shallow traps emitting small amounts of charge while in the bulk region the dark current is generated by a few deeper level trapping sites emitting large charge levels (Burt 2002). Although there is no way to suppress the dark current generated in the bulk silicon of a device, the accumulated surface charge can be reduced by holding the surface in inversion. With the surface of a CCD in inversion the holes are attracted from the channel stops filling the trapping sites in the insulating layers of the device. The dark current spectrum is Gaussian in nature with a high energy tail composed of 'dark current spikes'. The nature of dark current spikes is discussed below.

3.4.3. Increase in Charge Transfer Inefficiency

Energy levels in the silicon band-gap generated by displacement damage of a CCD can trap charge carriers resulting in a loss of signal charge as charge is held from its associated signal packet during readout. The trapping time is dependent on the concentration and emission rate of the defect involved. Figure 3.17 shows the approximate variation in emission rate for several common defects as a function of temperature. For devices operating at optical wavelengths and at TV frame rates, the CTI can be decreased by radiation damage without significant loss of image quality. The apparent loss in CTI can be decreased by thermal generation of charge filling the traps in place of signal charge (Hopkinson 1992, Holmes-Siedle et al. 1995) or charge injection.

A number of techniques have been developed to measure the CTI of a CCD. The 'fill and spill' method involves measuring the delay in charge transfer of a specific charge packet, while the 'stacked line trace' method involves creating an array of histograms, each created from a different region of interest on the CCD, and evaluating the CTI by characterising the change in mean energy of an X-ray peak with position across the CCD array (Holland 1990). The slope of the X-ray peak in the stacked line trace is proportional to the CTI value, the shallower the slope, the lower the CTI.

The CTI of a device can be decreased in a number of ways:

- Higher Signal Charge: A reduction in the fraction of signal charge lost to trapping is brought about by higher signal charge levels.

- Faster Pixel Transfer Speed: By increasing the clocking speed of the CCD to faster than the trapping time constant of the predominant traps, less charge from the signal packet will become trapped before transfer of the charge.

- High Temperature Annealing: Trapping sites can be annealed at high temperatures to regain some charge transfer performance (Holland 1991).

- Low Temperature Operation: CTI has been seen to decrease with decreasing temperature as a result of ‘freezing’ carriers in trap sites (Holland et al. 1991).

- Changes in Device Structure: Successful CTI reduction has been observed using narrow channel (Holland et al. 1991) or supplementary channel (Bredthauer et al. 1991) electrode structures where the signal charge is confined in a smaller volume reducing the number of trapping sites in the vicinity of the signal charge.

- Defect Engineering: Several ways of reducing the amount of phosphorous-vacancy defects in a device have also been investigated in an attempt to remove the main charge trapping mechanism responsible for increasing CTI (Holmes-Siedle et al. 1995, Hopkinson 1999).

- Charge Injection: Some CCD designs incorporate a structure to allow charge to be injected into the first image row of the device. This charge is then swept through the image and store sections of the device filling many of the traps and reducing the CTI (Holland et al. 1993). A variation on this idea involves integrating signal charge in the first few rows of a device before the accumulated charge is swept through the device on readout. This method involves no extra CCD structure and instead relies on a novel CCD clocking method (Prigozhin et al. 2000).

The XMM-Newton spacecraft has taken advantage of narrow electrode and charge injection structures in the design of the CCDs employed in the two MOS European Photon Imaging Cameras onboard. Charge injection tests have been investigated in the laboratory while a reduction in operating temperature from -100 ^{o}C to -120 ^{o}C has been investigated on orbit. Both these techniques have shown beneficial reductions in CTI (Abbey et al. 2002).

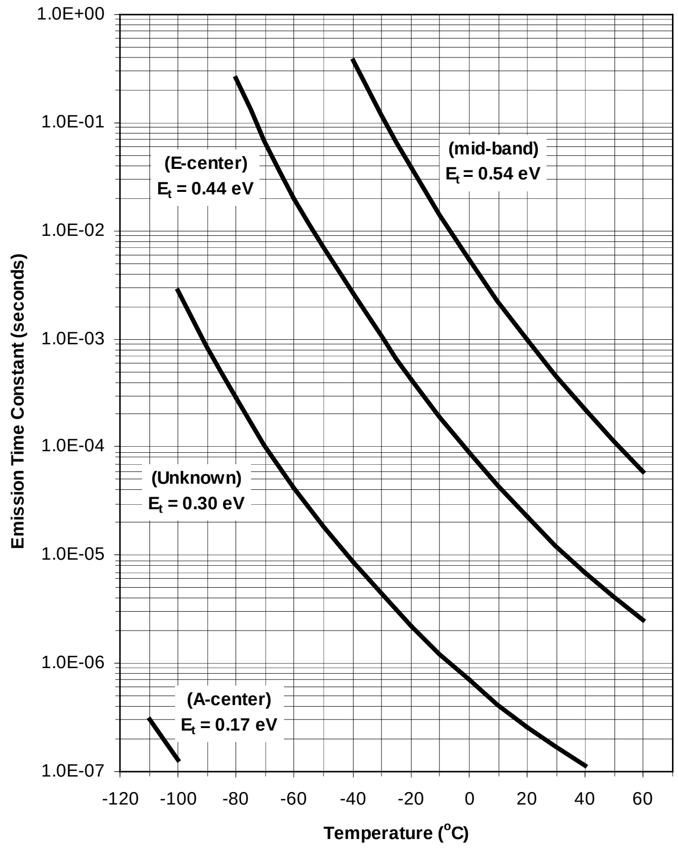

Figure 3.17 The approximate variation in emission time constant with temperature of several common defects found in the CCD (Burt 2002)

3.4.4. Bright Pixels

Bright pixels, or dark current spikes, are found to be present in a CCD prior to irradiation, but the number of bright pixels is greatly increased after irradiation, especially with protons. The bright pixel spikes found in unirradiated devices are possibly due to metal precipitates at oxidation-induced faults (Burt 2002) while the spikes found post irradiation are caused by induced carrier emission sites within the bulk and depleted silicon of the CCD. The amplitude range of bright pixels covers a broad range and is seen in the dark current histogram of a CCD as a high energy tail on the Gaussian distribution of the CCD dark current. The range in amplitudes results from the different induced mid band-gap energy levels caused by irradiation of a device, coupled with any 'Field Enhanced Emission' factor. Some bright pixels exhibit a 'switching' behaviour, changing sharply between two or more distinct charge levels with random time constants. This type of pixel fluctuation has become known as 'Random Telegraph Signal' behaviour and is the subject of Chapter 6 below.

3.4.4.1. Field Enhanced Emission

Field enhanced emission can result from three possible mechanisms: the 'Poole-Frenkel' effect, where an electron climbs over a potential barrier lowered by an applied electric field, 'pure tunnelling', and 'phonon assisted tunnelling', where an electron absorbs thermal energy from the lattice and can tunnel through the potential barrier (Martin et al. 1981). These three processes are illustrated in Figure 3.18.

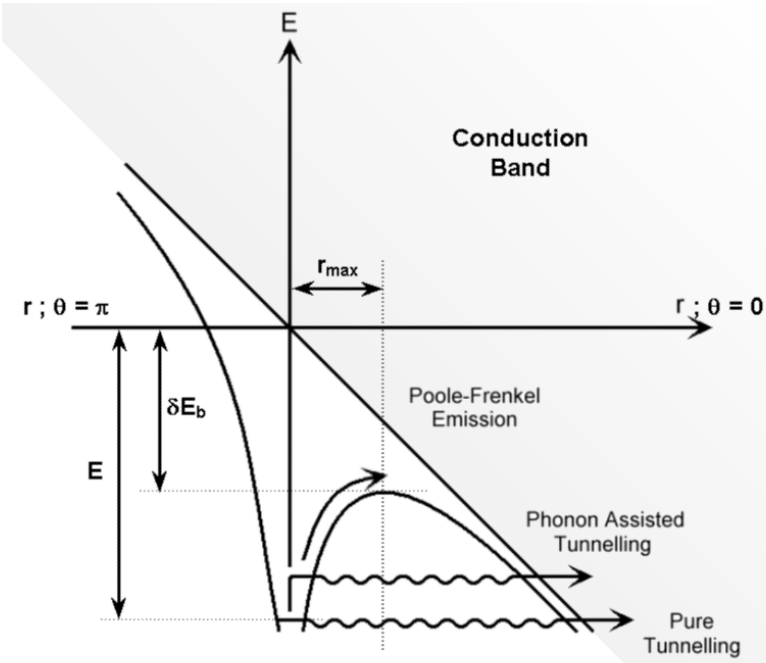

Figure 3.18 The three possible mechanisms of field enhanced emission (adapted from Martin et al. 1981)

In a CCD the electric field strength associated with the channel stop and inter-electrode regions of a pixel can be of order 10^5 - 10^6 V cm^{-1}, causing significant field enhanced emission. The enhancement factor for Poole-Frenkel emission in the case of an electron trapped at an energy level *E* below the conduction band edge, can be obtained by first considering the potential. An electron trapped by a singly charged positive ion, located at r = 0, under the influence of a uniform applied electric field, ξ, will experience a potential, *V*, given by:

$$V(r) = \frac{-q^2}{4\pi\varepsilon_{si}\varepsilon_0 r} - q\xi r\cos\theta \tag{3.3}$$

Where spherical co-ordinates are used and the arbitrary zero of energy is taken to be the conduction band edge at $r = 0$, as shown in Figure 3.19 (Hartke 1968). The potential minimum at $r = r_{max}$ is found by setting $\partial V/\partial r = 0$, to obtain:

$$r_{\max} = \left(\frac{q}{4\pi\varepsilon_{Si}\varepsilon_0 \xi \cos\theta} \right)^{\frac{1}{2}} \tag{3.4}$$

Evaluating V at $r = r_{max}$ gives an expression for the reduction in the potential barrier height, δE_b, due to the presence of an applied electric field:

$$\delta E_b = q\left(\frac{q\xi \cos\theta}{\pi\varepsilon_{Si}\varepsilon_0} \right)^{\frac{1}{2}} \tag{3.5}$$

Integrating over θ due to the spatial variation of δE_b, the reciprocal lifetime of a trapped electron in the presence of an applied electric field, $1/\tau_r$, is obtained:

$$\frac{1}{\tau_r} = \frac{1}{4\pi}\left(\int_0^{2\pi} d\phi \int_0^{\frac{\pi}{2}} \sin\theta d\theta \exp\left[-\frac{\delta E_b}{kT}(\theta) \right] + \int_0^{2\pi} d\phi \int_{\frac{\pi}{2}}^{\pi} \sin\theta d\theta \right) \tag{3.6}$$

Where it has been assumed that the electron release rate is independent of the applied electric field for $\pi/2 \leq \theta \leq \pi$, where the potential barrier height is increased by the electric field. These integrals can then be evaluated by substitution, using $t = \cos\theta$, to give an expression for the emission enhancement due to an applied electric field:

$$\frac{\tau_{r0}}{\tau_r} = \left(\frac{1}{\alpha^2} \right)\left[\exp^{\alpha}(\alpha - 1) + 1 \right] + \frac{1}{2} \tag{3.7}$$

Where the reciprocal lifetime in the absence of an applied electric field, $1/\tau_{r0}$, is $\exp\left(-E/kT\right)$ and α is given by:

$$\alpha = \left(\frac{q^3 \xi}{\pi\varepsilon_{Si}\varepsilon_0 (kT)^2} \right)^{\frac{1}{2}} \tag{3.8}$$

Figure 3.19 shows the emission enhancement for silicon over the electric field strength values of interest, calculated using equation 3.7. Of the remaining two field enhanced emission processes, pure tunnelling only becomes an important contribution at electric field strengths above a few 10^7 V cm^{-1}. Phonon assisted tunnelling is however important in the electric field strength range of interest and adds an additional component to the total field enhanced emission rate.

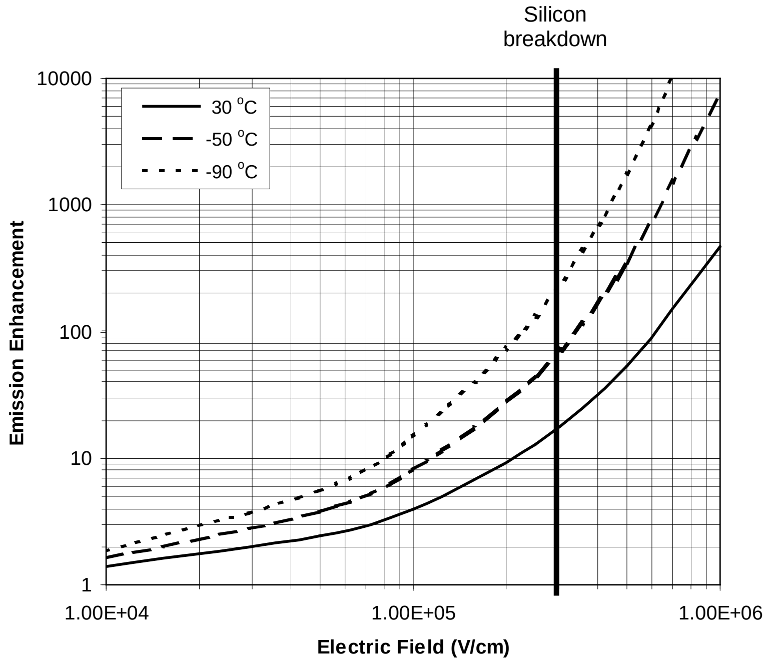

Figure 3.19 Modelled Poole-Frenkel emission enhancement for silicon

3.4.5. Transient Effects

The highly energetic particles in a cosmic ray produce a minimum ionisation of ~80 electrons μm^{-1} as they pass through a CCD causing a group of pixels in the device to appear bright, generally only for a single frame before the excess charge is swept away. Usually cosmic ray events are detected by CCD readout software and removed from the image analysis.

3.4.6. Radiation Damage Prediction Tools

The main radiation effect of concern when using CCDs for spectral sensitivity and positional science is CTI. Usually for these applications the CCD is operated cooled, for example at -90 ^{o}C, and therefore the dark current component is negligible. A number of repeatable experimental studies have been carried out investigating the variation in CTI with proton flux, temperature, irradiation bias, signal charge size and readout speed. From the experimental studies a number of models have been developed that produce results comparable to the measured CTI levels including those by Holland et al. (1991), and Dale et al. (1993). Figure 3.20 shows the modelled variation in CTI with 10 MeV proton irradiation fluence for an E2V Technologies CCD02 device operating at -90 ^{o}C.

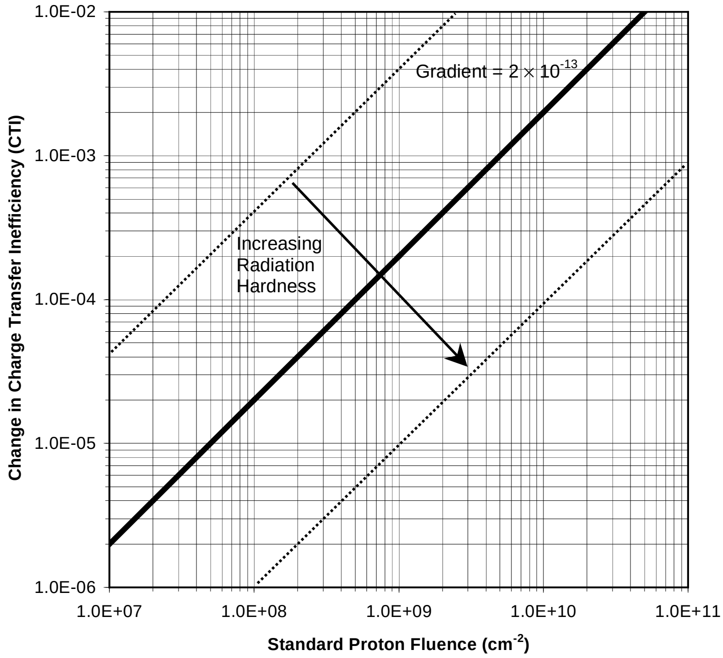

Figure 3.20 A model for CTI growth variation with 10 MeV proton irradiation fluence for a CCD02 with an 8 μm wide buried channel and 22 μm^2 pixels operating at -90 ^{o}C (Holland et al. 1991)

3.5. Summary

This chapter has presented the various components of the space radiation environment and described a number of computational models that can be used to simulate the environment. The NIEL function has been introduced as a method of normalising proton fluence to equivalent 10 MeV proton fluence, allowing the comparison of radiation damage results from different proton irradiation experiments. The two radiation damage mechanisms of importance in CCDs, ionisation and displacement damage, have been described in detail, followed by descriptions of the various effects radiation damage has on the operational characteristics of CCDs. The next chapter presents work carried out to assess the potential of using novel low light level CCD technology for space applications. Two devices featuring the novel technology were irradiated with protons and the effects of radiation damage on the operational characteristics of the devices were observed.

Chapter 4: L3Vision Radiation Testing

This chapter investigates the effects of proton irradiation on the operational characteristics of novel L3Vision CCDs in order to assess their potential for use in space. The L3Vision technology is described first, followed by the experimental method employed for the irradiation of two such devices. The experimental results are then presented and the observed radiation effects discussed in light of the possible use of L3Vision technology for space applications.

4.1. Introduction

A new CCD technology called L3Vision was developed by E2V Technologies in 2000, that reduces the effective readout noise of a device to less than one electron, even while operating at MHz pixel rates. The device works by having an additional ‘gain’ register after the readout register of the CCD in which the signal charge is multiplied by an avalanche process before reaching the output amplifier, increasing the signal to noise (Jerram et al. 2001, Mackay et al. 2001). The effective readout noise, σ_{eff}, for a gain, G, is given by:

$$\sigma_{eff} = \frac{\sigma_r}{G} \tag{4.1}$$

Where σ_r is the actual readout noise of the device.

A principle weakness of the CCD as a detector is that a faster readout time results in an increase in readout noise. The L3Vision technology addresses this problem and provides devices that have readout noise comparable to the best image intensifiers.

The L3Vision devices are suited to applications where light levels are very low and therefore there is potential for their use in space based applications for looking at faint sources. One potential space application of the L3Vision technology currently under consideration is the Radial Velocity Spectrometer, RVS, instrument for the planned GAIA astrometry mission. According to the current specification, the RVS instrument will be composed of 3 CCDs used to acquire spectra from very faint sources typically with less than one signal electron per pixel in the spectrum. The main operational constraint on the instrument is the very small charge levels associated with the faintest stars it can observe. A possible option to improve the magnitude limit that can be observed by the RVS is the application of L3Vision technology to the CCDs of the instrument.

To be a viable technology for use in the space environment it is necessary to know if the gain register of an L3Vision device is tolerant to the space radiation environment encountered by scientific satellites, and will not be susceptible to catastrophic breakdown failure as a result of radiation damage. Bright pixels generated in the high field avalanche regions of the gain register, as a result of radiation damage, could lead to 'white' images.

This chapter studies the effects of radiation on CCD65 devices incorporating the L3Vision technology and ascertains their suitability for space applications. Two such devices were obtained and subjected to proton fluences representative of total mission fluences expected to be received by typical spacecraft (Holmes-Siedle et al. 1995). This chapter first describes the architecture of the CCD65 device before detailing the experimental method employed and the results obtained.

4.2. CCD65 Structure

The CCD65 is a frame transfer device that has a standard readout register followed by a 'gain' register that multiplies the signal charge before it is sensed by the output FET. The device can be operated in inverted mode to suppress dark current. The inverted mode dark current is typically ~200 electrons per pixel per second at 20 ^{o}C. The image and store sections of the CCD are each 591 $\times$ 296 pixels, while the readout and gain registers are each 591 pixels in length plus a few reference pixels. The device characteristics are summarised in Table 4.1. The pixels in the gain register are larger than the other pixels in the device in order to handle the potentially larger signal charge after gain. Figure 4.1 shows the geometrical layout of the device.

Active image area		11.52 × 8.64 mm
Image section		591 × 296 pixels
Store section		591 × 296 pixels
Pixel size:	Image section	20 × 30 µm
	Store section	13.5 × 30 µm
	Readout register	20 × 30 µm
	Gain register	40 × 30 µm
Spectral range		400 – 1060 nm

Table 4.1 E2V Technologies CCD65 characteristics

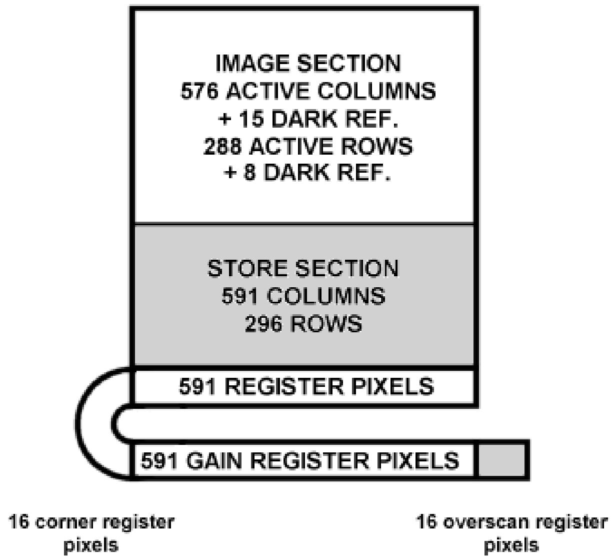

Figure 4.1 The geometrical layout of the CCD65 L3Vision device

4.2.1. The Gain Register Avalanche Process

The gain in the signal as it passes through the gain register occurs because one electrode in each of the pixels in the register is clocked with a much higher voltage than is needed to just transfer the charge. Figure 4.2 shows a cross-section of the gain register electrodes and corresponding potentials during charge transfer. An additional electrode held at ~2 volts d.c. is included before the high voltage electrode typically held at ~40 - 50 volts. The large electric field present between the high voltage electrode and the d.c. electrode causes the charge carriers to be accelerated to a high enough velocity to generate more charge carriers through the process of impact ionisation (Grove 1967).

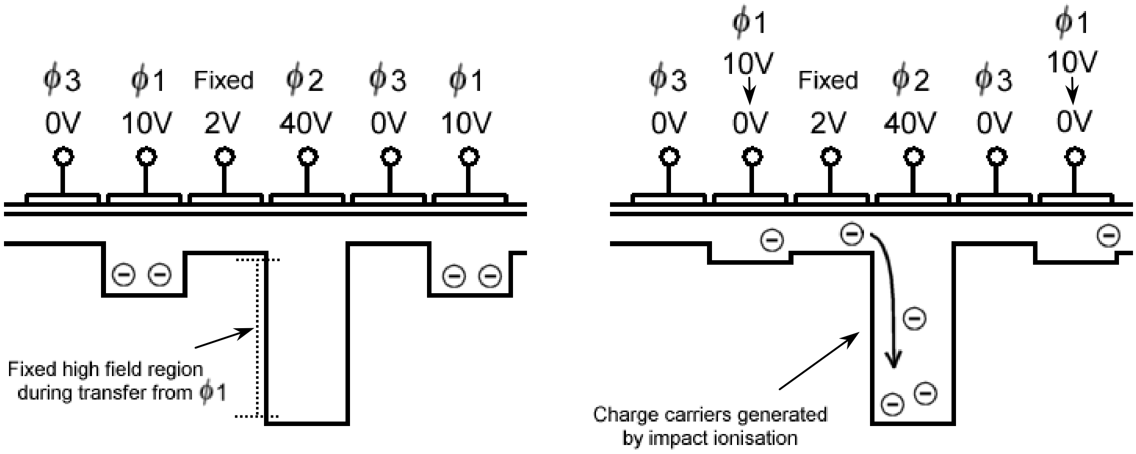

Figure 4.2 Charge transfer in an L3Vision gain register

The average gain per pixel transfer through the gain register is generally small, but on passing through the full 591 gain register elements the total gain can be of order a few hundred. The gain, *G*, is given by:

$$G = (1 + R)^{\gamma} \tag{4.2}$$

Where *R* is the mean gain per transfer and γ is the number of gain elements. For the CCD65, taking *R* as 0.01, the gain is ~358. The value of *R* is dependent on the statistical variation in the amount of impact ionisation caused by the electric field strength between the d.c. and high voltage electrodes. By varying the bias of the high voltage electrode from a standard drive voltage of ~12 volts to ~50 volts, gain values ranging from 1 to 1000 can be obtained.

With a gain of unity the L3Vision device operates in the same way as a standard device, with a single extra row in the readout sequence. The measured variation in gain with applied bias voltage at three different temperatures is shown in Figure 4.3. The gain is seen to increase with decreasing temperature at a given applied voltage due to the temperature dependence of the electron ionisation rate. For a given electric field, the ionisation rate increases with decreasing temperature as described in detail by Sze (1981).

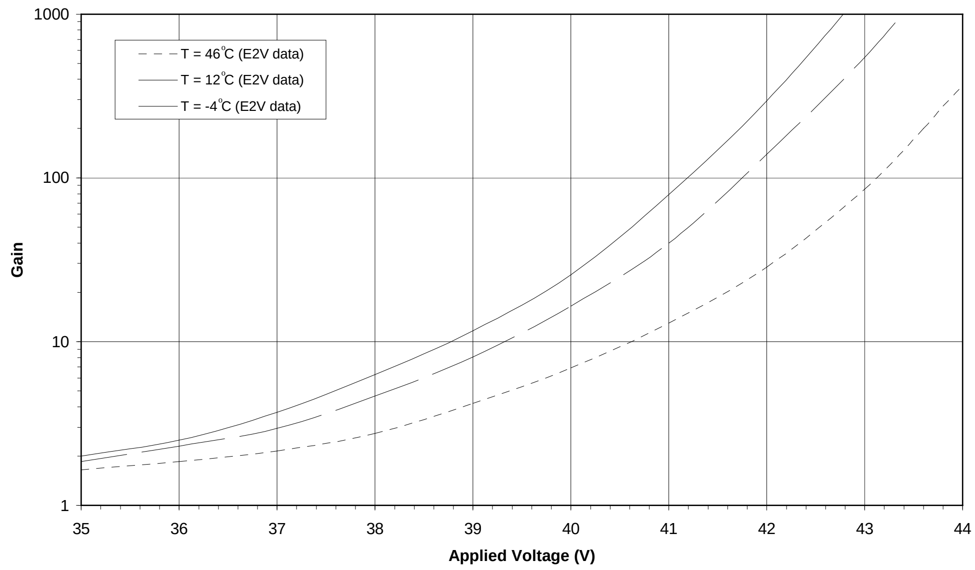

Figure 4.3 E2V Technologies measured variation of gain with applied bias voltage for a CCD65

The statistical variation in the gain makes it difficult to reconstruct the number of electrons in the original signal packets detected. A device using the L3Vision technology can only be successfully used for optical photon counting purposes when the incident photon flux is low enough to only generate a single electron in a pixel during image integration without pile-up occurring. If this is the case, the gain of the device can be set to ~1000 to clearly discriminate single electron events from the output amplifier noise. Figure 4.4 shows the distribution of output signal size for input events of 1, 2 and 3 electrons, with a 1 % probability of gain per stage in the L3Vision gain register. The data shown was generated using a simple Monte Carlo model. The 5σ noise threshold is also shown, indicating that for this particular gain level, 1 and 2 electron events may not be discernible from the noise peak after gain.

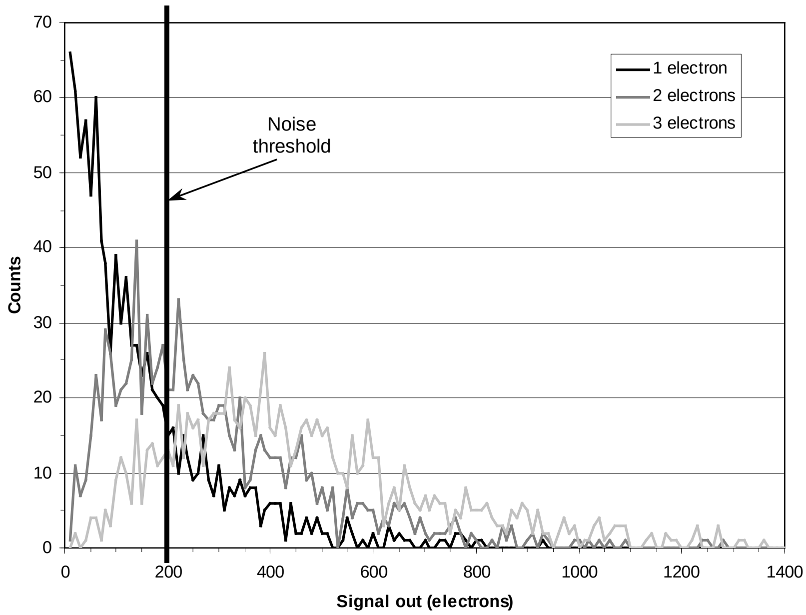

Figure 4.4 The distribution of output signal size for input events of 1, 2 and 3 electrons after transfer through the L3Vision gain register, with a 1 % probability of gain per transfer

4.3. Experimental Method

4.3.1. The Accelerator Facility and Dosimetry

Irradiation of two L3Vision CCD65 devices was carried out using the cyclotron accelerator facility at Birmingham University, UK. Figure 4.5 shows a schematic of the Birmingham beam line.

Figure 4.5 A schematic of the Birmingham cyclotron beam line

Prior to irradiation of the devices, the uniformity of the proton beam over the target region was examined by using a photodiode in pulse counting mode. The spectrum analyser used was a Nucleus Inc. PCA-II card and software, the photodiode used was a UDT Sensors diode, part number PIN-3CD. The photodiode characteristics are summarised in Table 4.2.

Active area	3.2 mm^2
Active thickness[a]	27 μm
Capacitance	10 pF (at 10 V/1 kHz)
Leakage current	2 nA
Rise time	15 ns (50 Ω load)

[a] As determined by Holmes-Siedle et al. (1995)

Table 4.2 UDT Sensors PIN-3CD photodiode characteristics

The photodiode was mounted on a support arm attached to the inside face of the cryostat front plate which allowed the diode to be positioned on a locus passing through the centre of the beam line. The flux per cm^2 reaching the photodiode in 1 minute was measured several times both in the centre of the beam and at a position 5 mm away from the centre, representative of the CCD target area to be irradiated. The variation in beam uniformity across the target area was measured to be ±15 %. The mean energy of the proton beam was 6.5 MeV for the irradiations carried out. An example of a typical recorded spectrum is shown in Figure 4.6.

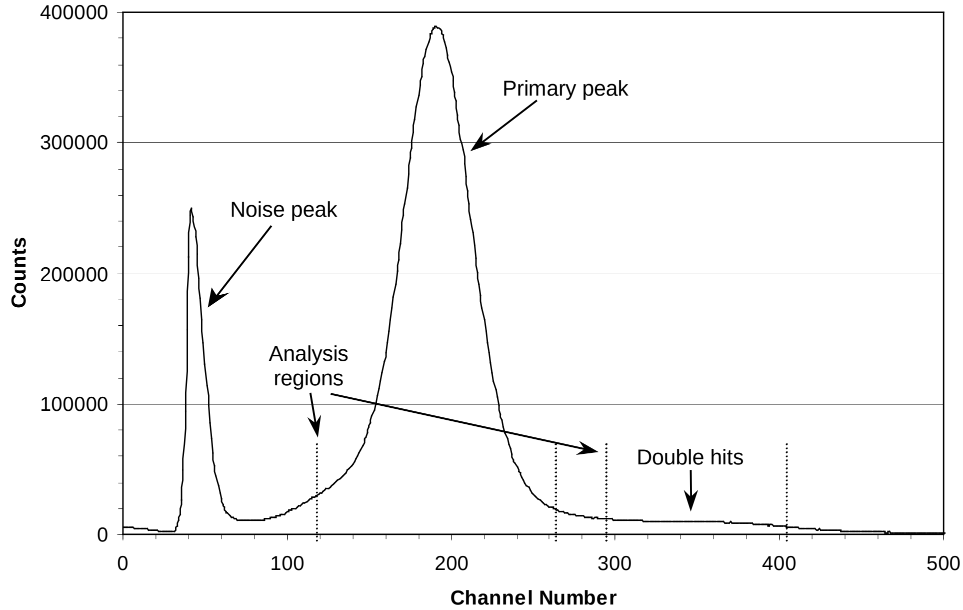

Figure 4.6 A PIN-3CD photodiode pulse height spectrum

The primary ionisation peak is clearly discernible from the noise peak allowing accurate determination of the number of photons being counted in the active region of the photodiode. Protons that interact with the diode twice during the same shaping period, ~1 μs, are also seen in the recorded spectrum, forming a secondary 'pile-up' peak. The number of counts in the secondary peak was doubled and added to the number in the primary peak to estimate the total proton fluence. The analysis regions for each peak are indicated in Figure 4.6.

During each irradiation the photodiode was positioned ~2 cm in front of the shielded section of the target CCD and used to accurately monitor the proton fluence reaching the CCD in real time. The system live time, T_{live}, and the actual elapsed time, $T_{elapsed}$, for each irradiation were both monitored and used to account for the dead-time in the system (typically ~20 %). Using the NIEL function, the final 10 MeV equivalent proton fluence received in each irradiation, F_{10MeV}, was calculated by:

$$F_{10MeV} = \left(\frac{N_{total}}{A_{diode}}\right)\left(\frac{T_{elapsed}}{T_{live}}\right)\left(\frac{NIEL(10MeV)}{NIEL(6.5MeV)}\right) \tag{4.3}$$

Where N_{total} is the number of counts in the primary proton peak plus two times the number of counts in the secondary peak and A_{diode} is the area of the diode. The error associated with the dosimetry of each irradiation was taken to be ~20 %, based on the beam uniformity measurements and the lack of including counts in any tertiary peaks beyond the primary and secondary peaks in the measured photodiode pulse height spectra.

4.3.2. Irradiation of CCDs

After determination of the proton beam characteristics, the two CCDs were irradiated one after the other. Previous studies have shown that device temperature during irradiation does not influence the radiation damage effects observed (Holmes-Siedle et al. 1995). The irradiations were therefore carried out at 22 ^{o}C requiring no cooling equipment. In each case the target CCD was mounted in a vacuum chamber attached to the end of the beam line. The beam line and target chamber were under vacuum during the irradiations to prevent loss of protons to ionisation with air. All CCD pins were grounded to avoid potential static damage. Aluminium shields were used to cover parts of the CCDs that were to be kept unirradiated as control areas. Figure 4.7 shows the area of each device irradiated and the 10 MeV equivalent proton dose each area received.

The whole of the readout and gain registers, and half of the image and store sections, of device 00463-10-12 were irradiated with a 10 MeV equivalent proton fluence of 5.1×10^8 protons cm^{-2}. A 10 MeV equivalent proton fluence of 1.0×10^8 protons cm^{-2} was given to the left half of device 00463-10-13, with an additional dose of 2.0×10^9 protons cm^{-2} given to just the left half of the readout and gain registers. Figure 4.6 shows the photodiode spectrum recorded for the 1.0×10^8 protons cm^{-2} irradiation of device 00463-10-13.

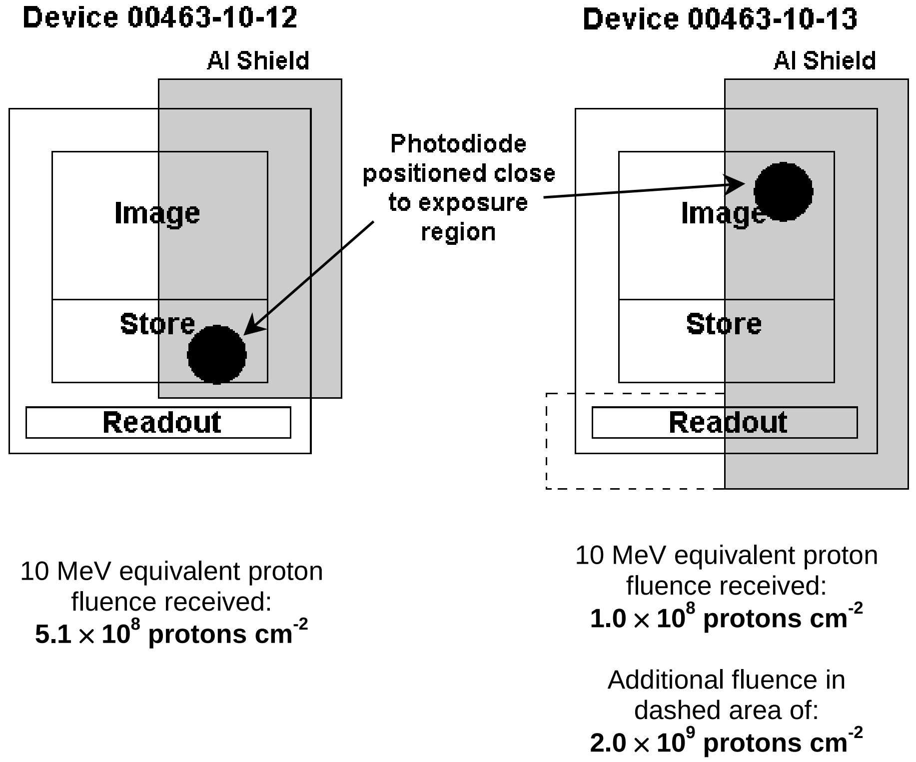

Figure 4.7 A schematic showing the proton irradiated areas of two L3Vision CCD65 devices and the associated 10 MeV equivalent proton doses received

4.4. Experimental Results

After irradiation both CCDs remained functional and at a temperature of 22 ^{o}C showed increased dark current and bright pixel counts comparable to those observed in CCDs subjected to similar proton doses (Ambrosi et al. 2002).

For device 00463-10-13 a sequencer program was used to readout only the readout and gain register pixels of the device. The image clocks were suspended during readout to avoid thermal leakage current from the image and store sections entering the readout register. A series of short 3 ms row integrations were then taken. Figure 4.8 shows an accumulation of 200 such rows, together with annotations indicating the different device and proton exposure regions.

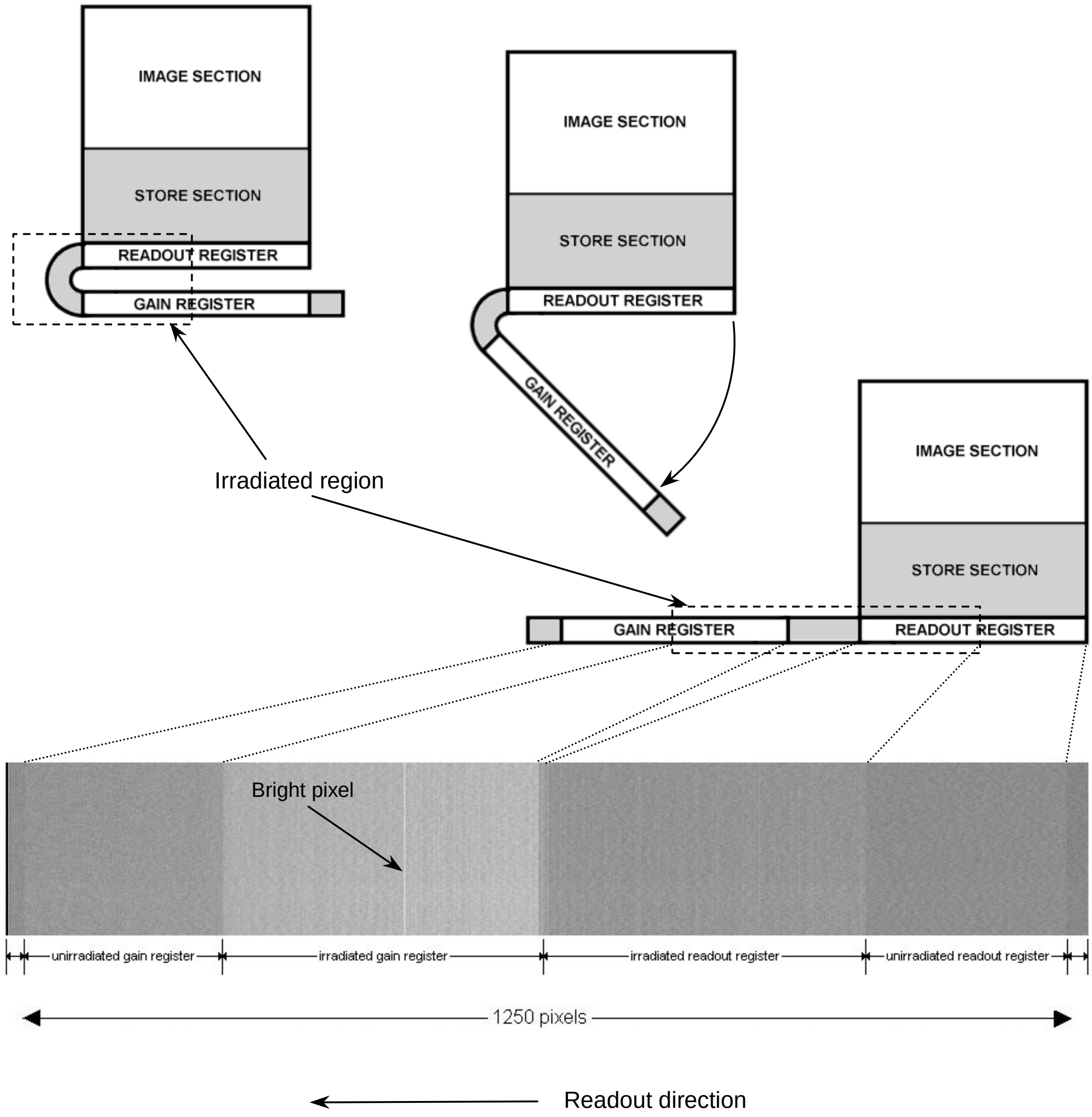

Figure 4.8 An image taken using a sequencer program that only reads out pixels in the readout and gain registers of the device. The irradiated and unirradiated sections of the readout register can be seen, along with under and overscan pixels. The figure includes diagrams of the L3Vision device to correlate the sections of the recorded image with the physical sections of the device

Figure 4.9 shows the average of the rows in the recorded image of Figure 4.8. The figure has four sections, which are from right to left: non-irradiated readout register; irradiated readout register; irradiated gain register; non-irradiated gain register. The slope of the signal in the gain register, the increase in number of bright pixels and the increase in base dark current level due to proton irradiation can all be seen in this figure. The factor of ~2 increase in dark current level between the gain register and readout register is due to the factor of ~2 increase in pixel size from those in the readout register compared to those in the gain register. At low applied voltage levels an indication of proton beam non-uniformity, slopes *A* and *B* in Figure 4.9, can be seen.

Comparison of the measured post irradiation gain curves with those for the L3Vision CCD65 as measured by E2V Technologies, Figure 4.10, show that the irradiations have not significantly affected the behaviour of the device.

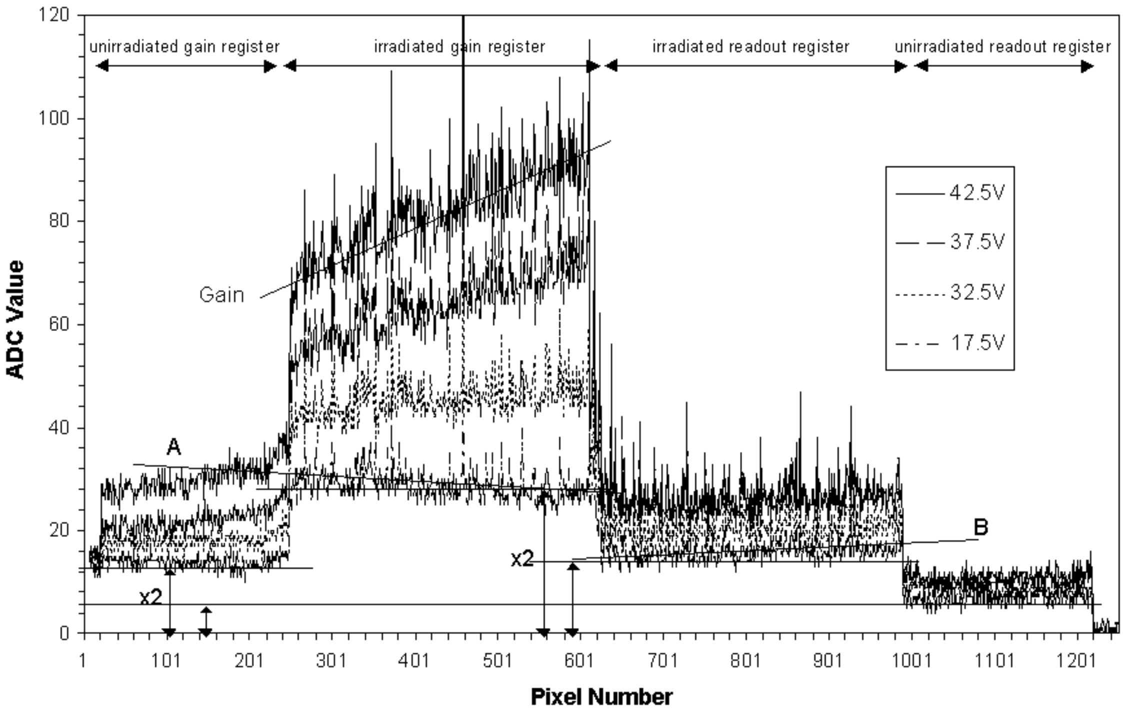

Figure 4.9 The effect of different applied voltage on the L3Vision readout and gain registers. Slopes A and B show an indication of proton beam non-uniformity with low applied voltage. The gain is seen to increase sharply once the applied voltage is increased above 30 volts. The factor 2 increase in dark current level between the gain register and readout register due to different pixel sizes is also indicated

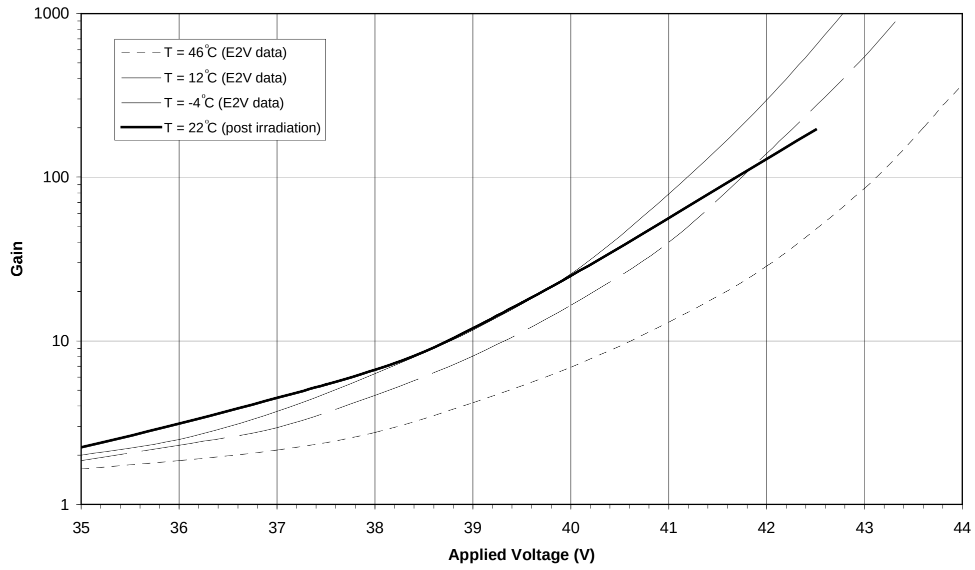

Figure 4.10 Measured variation of gain with applied bias voltage post irradiation. Gain curves as measured by E2V Technologies for the L3Vision CCD65 are shown for comparison

4.5. Discussion

After irradiation with protons the L3Vision device is found to operate normally, with the resulting change in dark current and number of bright pixels comparable to previous proton irradiation studies. The behaviour of the gain register did not change as a result of proton irradiation. Bright pixels generated in the gain register were found to increase in amplitude in the same way as the normal gain register pixels, showing no evidence of extraneous field enhancement effects. It is therefore assumed that the observed bright pixels generated were not located in the vicinity of a high field avalanche region.

After studying the effects of proton irradiation on two L3Vision devices, there appear to be no problems that would inhibit the use L3Vision technology for space based applications. There is however a need to irradiate further devices in order to deduce if emission sites generated in the high field regions of the gain register pixels can cause device failure. This study can not be carried out by irradiating a single device to a high fluence as this would result in all the pixels in the gain register becoming bright.

In terms of area, 25 % of the gain register is comprised of the high voltage electrode. The probability of obtaining a bright defect in an avalanche region of the gain register after irradiation is therefore approximately 0.25. After irradiation with 2.1×10^9 protons cm^{-2}, 3 bright pixels were generated in the gain register of device 00463-10-13. An irradiation of 2.8×10^9 protons cm^{-2} will therefore generate 4 bright defects in the gain register, one of which should lie in the avalanche region. Irradiation of 20 devices to this level will yield ~20 bright defects in the avalanche region of the device giving good statistics on whether such a defect can cause device failure. Conversely, using an irradiation level of 2.1×10^9 protons cm^{-2} as in the presented study, 27 devices would need to be irradiated to generate ~20 bright defects in the avalanche region of the device.

If the CCDs chosen for the RVS instrument on GAIA use the L3Vision technology, assuming the gain register is the same as that of the CCD65 devices, there may be a 1 in 4 chance of device failure when irradiating the whole gain register to a level of 2.1×10^9 protons cm^{-2}, if a bright defect in the avalanche region does indeed cause device failure. This statement emphasises the need for irradiation of a large number, ~25, L3Vision devices.

Previous proton irradiation studies on conventional CCDs have shown that irradiation with the device unbiased, as in this study, induces significantly lower voltage shifts than if the device were operational during the irradiations. The magnitude of these voltage shifts and their effect on L3Vision device performance also needs to be investigated in the future irradiation study.

4.6. Summary

This chapter has presented work carried out to assess the potential for use of CCDs featuring L3Vision technology in space. Two test devices were irradiated with proton fluences representative of mission doses received by typical Earth orbiting spacecraft. The L3Vision technology and the irradiation methodology have been described followed by a detailed analysis of the radiation damage effects caused by the proton irradiations. The two devices tested were found to operate as expected after irradiation with no significant changes in the behaviour of the gain register, proving the L3Vision technology has potential for use in future low light level space applications. The next chapter describes another series of proton irradiation studies with a different CCD type. The aim of this second study was to assess the effects of low energy proton irradiation on the operational characteristics of the devices.

Chapter 5: The Effects of Low Energy Protons on CCDs

This chapter investigates the effects of low energy proton irradiation on the operational characteristics of E2V Technologies CCD22 devices. The reasons behind the work and the experimental method are described in detail along with a computational model that was developed to model the expected CTI changes resulting from the experimental soft proton irradiations. The experimental and modelled results are then presented and discussed.

5.1. Introduction

The Chandra spacecraft demonstrated that not only X-ray photons, but soft protons with energies below 500 keV could be focused by the spacecraft's X-ray mirrors, onto the AXAF CCD Imaging Spectrometer (ACIS) (Prigozhin et al. 2000, O'Dell et al. 2000). Chandra's mirrors are arranged in a Wolter Type 1 arrangement that allows the focusing of X-rays by shallow angle grazing incidence onto the focal plane detectors. A similar mirror module design was used for the XMM-Newton spacecraft and a study by Rasmussen et al. (1999) showed that, as for Chandra, soft protons could be scattered by single or double grazing interactions with the mirrors onto the European Photon Imaging Camera (EPIC) MOS X-ray focal plane detectors. Figure 5.1 shows the design of a Wolter Type 1 optic and shows the path of incoming photons as they are focussed by the two mirror sections onto the focal plane detector. The figure shows a single mirror 'shell', the actual XMM-Newton mirror module containing 58 nested mirror shells in a coaxial and confocal arrangement.

A comparison between the space environment induced degradation of the Chandra instruments and the possible effect on XMM-Newton showed that the EPIC MOS CCDs on XMM-Newton are susceptible to the same low energy protons that have caused damage to the ACIS CCDs on Chandra (Nartallo et al. 2001). The procedure for prevention of proton damage to the CCDs on XMM-Newton involves moving the filter wheel of each instrument to a 'closed' position when the radiation monitor onboard detects a proton flux above a threshold level. The insensitivity of the radiation monitor to soft protons results in a delay of order tens of minutes in closing the filter wheels, allowing soft protons to reach the detectors. In response to these findings, a critical investigation into the effects of soft protons on EPIC MOS CCDs was initiated to assess the impact of soft protons on the operational characteristics of the CCDs.

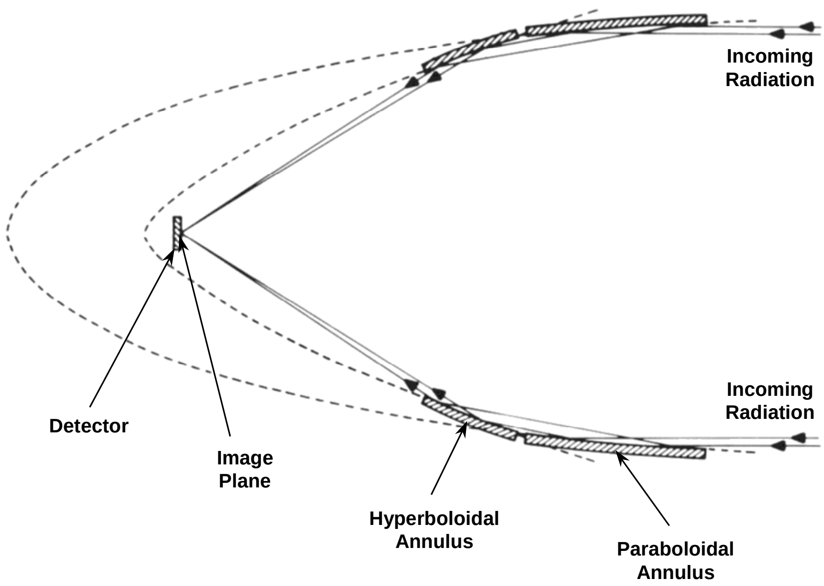

Figure 5.1 The Wolter Type 1 optic arrangement used for the mirror modules of the Chandra and XMM-Newton spacecraft

A study of the effects of soft protons was particularly important because soft protons have the potential for increasing CTI more than higher energy, MeV range, protons due to their higher scattering cross-section. Soft protons therefore penetrate only a short distance into a CCD, depositing most of their energy in the vicinity of the buried channel, where charge is transported.

Two CCD22 devices, the same as those used in the EPIC MOS cameras of the XMM-Newton satellite (Turner et al. 2001), were taken to the University of Tübingen to be irradiated with protons using a 3.5 MeV Van de Graaff accelerator facility. The CCD22 structure is presented below, followed by detailed descriptions of the irradiation methodology and data analysis. A Monte Carlo model developed to simulate the observed CTI changes that resulted from the proton irradiations is also presented.

5.2. CCD22 Structure

The CCD22 device is a front illuminated three-phase frame transfer device manufactured by E2V Technologies (Short et al. 1998). The CCD22 uses high resistivity silicon and an open electrode structure to obtain good quantum efficiency between 0.2 keV and 10 keV. The image section of the CCD consists of 600 × 600 pixels of 40 μm square with an additional 2 charge injection rows. The store section consists of 600 × 602 pixels, each measuring 39 μm × 12 μm. The device characteristics are summarised in Table 5.1. Each of the two XMM-Newton EPIC MOS focal plane cameras is comprised of 7 CCD22 devices arranged as shown in Figure 5.2.

Active image area		24 × 24 mm
Image section		600 × 600 pixels
Store section		600 × 602 pixels
Pixel size:	Image section	40 × 40 μm
	Store section	39 × 12 μm
	Readout register	39 × 12 μm
Spectral range		0.1 – 15 keV

Table 5.1 E2V Technologies CCD22 characteristics

Figure 5.2 The XMM-Newton EPIC MOS focal plane camera CCD arrangement

5.3. Experimental Method

5.3.1. The Accelerator Facility and Proton Damage Beam Line

The 3.5 MeV Van de Graaff accelerator at the Eberhard-Karls-Universität Tübingen, Germany, has a beam line dedicated to soft proton damage tests and was commissioned for evaluating the effect of soft proton damage on the pn-CCDs used in the EPIC program (Kendziorra et al. 2000). Figure 5.3 shows a schematic diagram of the experimental set up used for the CCD22 irradiations.

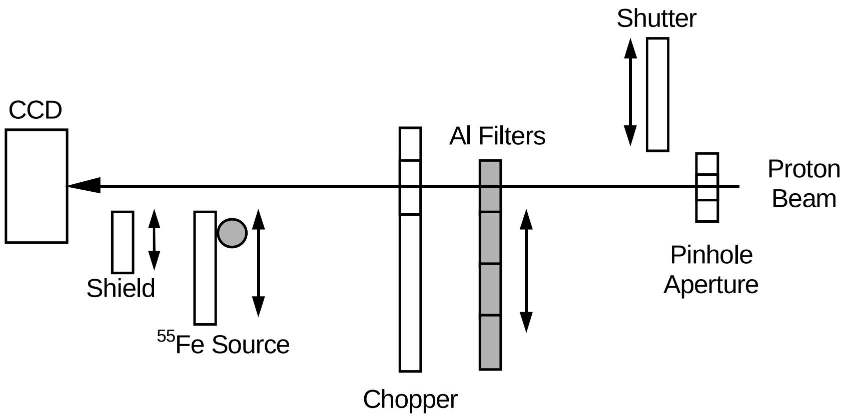

Figure 5.3 A schematic of the Tübingen proton damage beam line

A monoenergetic 900 keV nano-amp proton beam with a flux of ~1.0×10^{11} protons cm^{-2} s^{-1} was reduced to ~10^4 protons cm^{-2} s^{-1} by a copper pinhole aperture of 1.5 mm diameter. Aluminium foil filters of 10 μm, 12 μm, 13 μm and 14 μm thickness on a sliding holder were used to attenuate and broaden the spectral distribution of the beam. The mean energy of protons transmitted through each foil is given in Table 5.2 (Clauβ 2000). A rotating beam chopper with a 0.3 mm wide slit reduced the flux by a further factor of ~10^3. For calibration purposes a ^{55}Fe source could be moved in and out of the field of view of the CCD. A shutter was available to shield the CCD from the proton beam when not carrying out an irradiation.

Al Foil Thickness (μm)	*Mean energy of transmitted proton spectrum (keV)*
14	10
13	70
12	170
10	330

Table 5.2 Mean proton energy transmitted through different Al foil thicknesses (Clauβ 2000)

The final component of the beam line was a movable shield that could be positioned to cover the top or bottom half of the CCD by turning a dial on the outside of the beam line. The dial prevented the need to open the beam line and break the vacuum when changing the shield position to irradiate different sections of a CCD.

Proton spectra measured by a pn-CCD using 12 μm and 13 μm Al foils are shown in Figure 5.4 (Clauβ 2000).

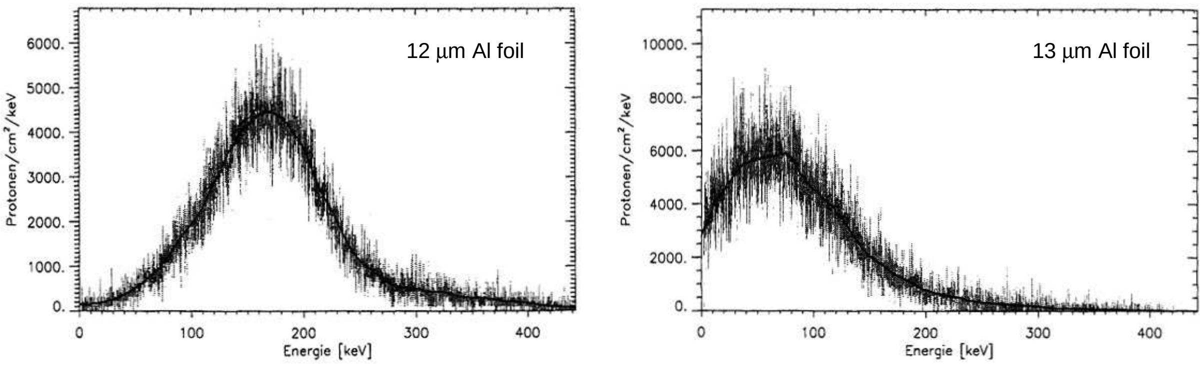

Figure 5.4 Proton spectra measured by a pn-CCD using 12 μm and 13 μm Al foils (Clauβ 2000)

5.3.2. Irradiation and Calibration of CCDs

Two EPIC CCDs were selected for irradiation. In each case the target CCD was fixed within a cryostat chamber bolted to the end of the beam line and cooled to -100 ^{o}C, the operational temperature of the devices on XMM-Newton. The CCD was located approximately 200 mm from the end of the beam line with an aluminium shield placed in front of the CCD store section to prevent X-rays or protons falling on it and causing CTI changes in the serial register. Although the CCDs selected for these tests were characterised in terms of CTI and response to various X-ray energies between 200 eV and 10 keV prior to irradiation with soft protons, the use of the movable shield in the beam line allowed certain areas of each CCD to be kept undamaged, providing a control for the damaged sections. The beam line and cryostat containing the target CCD were under vacuum during irradiation to prevent loss of protons to ionisation with air.

Prior to each irradiation, the position of the proton beam was measured to ensure an even spread of protons across the area to be irradiated. This was achieved by irradiating the CCD operating in photon counting mode for ~1 s with a very low flux rate, using the 14 μm aluminium foil. The observed distribution of protons in the resulting CCD image was used to deduce where the CCD should be moved to obtain the desired uniformity. The 14 μm foil and very short irradiation time were used for the beam positioning to prevent any damage to the CCD. The mean energy of protons transmitted through the 14 μm foil was 10 keV. This energy is low enough to be attenuated by 0.3 μm of silicon preventing any significant amount of energy being deposited in the buried channel of the device.

Before an irradiation, the target CCD was exposed to a short burst of protons in order to determine the proton flux, P_{flux}, passing through the aluminium foil being used:

$$P_{flux} = \frac{N_p}{T_f A_{ROI}} \tag{5.1}$$

Where N_p is the number of protons detected in an area of interest in a single frame, T_f is the frame time, and A_{ROI} is the size of the region of interest. The exposure time, T_d, for each section of the CCD to receive the required proton dose, η, could then be calculated:

$$T_d = \frac{\eta}{P_{flux}} \tag{5.2}$$

The total fluence received by each section of the two CCDs is shown in Figure 5.5. The white panels in the figure refer to the irradiated areas of the CCDs. The mean proton energy transmitted through each foil filter is also given in each panel. Each irradiation was preceded and followed by a calibration check with the ^{55}Fe source in order to measure changes in the parallel CTI.

At the end of each day of testing the CCDs were warmed to room temperature and maintained at this temperature overnight. Any annealing effects were observed each morning when the devices were again cooled to -100 ^{o}C and calibrated with the ^{55}Fe source.

Estimates from solar event spectral measurements taken by the EPIC pn-CCD camera on XMM-Newton (for protons between 100 keV and 200 keV) indicate that the EPIC MOS CCDs may have already received a soft proton dose of the order of 10^5 protons cm^{-2} in the worst case (Kendziorra et al. 2000). In this experiment, total doses exceeded 10^6 protons cm^{-2}, a value representative of the total dose the EPIC MOS devices are expected to receive over 10 years of operation.

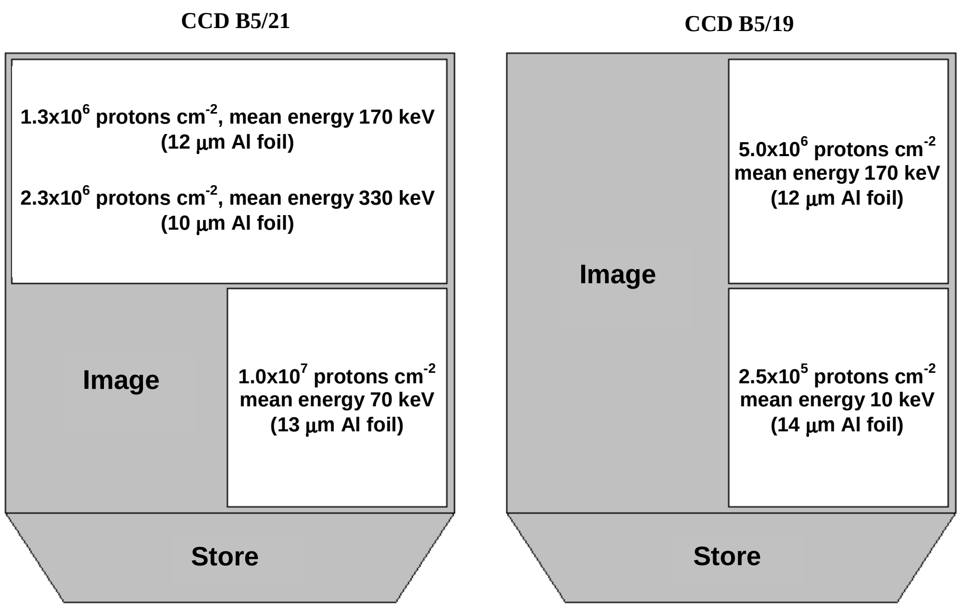

Figure 5.5 Total doses given to each section of the irradiated CCDs

5.3.3. Recorded Proton Spectra

The proton spectra obtained with the two CCD22 devices using the four available aluminium foils are shown in Figure 5.6. In each case, the count rate at the CCD had to be low enough to avoid pile-up during the 5.4 s frame time of the CCD. To avoid ADC saturation, the system was controlled by adjustment of the charge integration time. The complete proton spectrum through each aluminium foil could not be measured by the CCD due to limitations in pixel integration time and gain reduction. These limitations can be seen in the plots of Figure 5.6, where the highest energy measured through the 10 μm aluminium foil is 480 keV and through the 12 μm, 13 μm and 14 μm foils it is 182 keV.

The double peak in panel D of Figure 5.6 is not a real effect and is caused by the saturation of the analogue to digital converter. The peak at 200 keV is caused by multi-pixel events where the central pixel is saturated and charge has spread into adjacent pixels. The digital value of this pixel is therefore not representative of the total energy deposited by the proton in the pixel. At proton energies above 200 keV the penetration depth is higher in silicon and most of the events will be spread between several pixels as a result of charge being deposited in the field free region.

In comparing the measured CCD22 proton spectra through the 12 μm and 13 μm Al foils with those measured by the pn-CCD (Figure 5.4), an additional large low energy component is seen in the CCD22 spectra. This difference is the result of charge loss effects observed in the CCD22 device where electrons generated near the surface of the device become redistributed by tapping sites at the oxide interface. The amount of charge loss is more prevalent at lower temperatures and is a strong function of decreasing incident particle energy (Short et al. 2002).

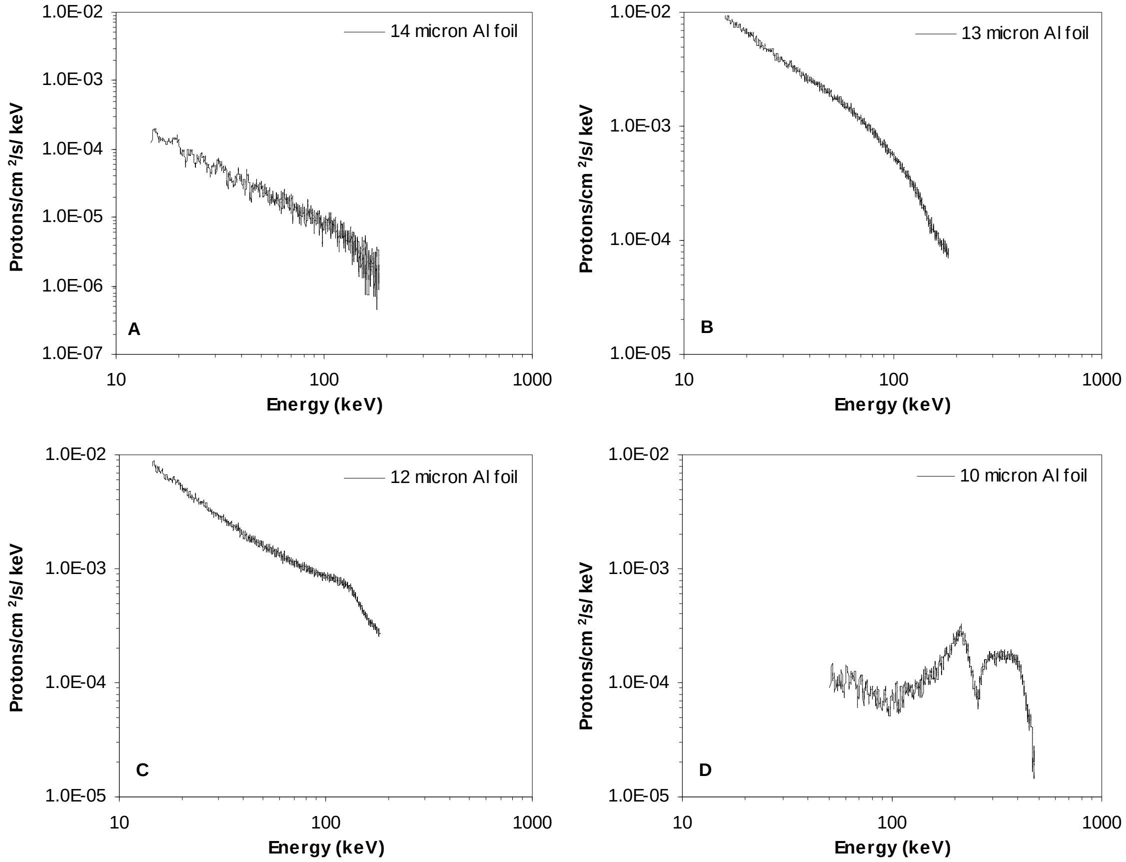

Figure 5.6 Proton spectra measured with EPIC MOS CCDs after irradiation through four different aluminium foil thicknesses

5.4. Computational Model

Predicting the CTI change in the CCDs irradiated with low energy protons was not possible using the standard Non-Ionising Energy Loss, 'NIEL', method of obtaining the 10 MeV equivalent proton dose. NIEL displacement damage scales with dose as the proton energy decreases (Dale et al. 1993). Below 1 MeV however, NIEL ceases to be an effective method of predicting CTI change as a function of proton dose. This is as a result of lower energy protons physically stopping in the vicinity of the CCD buried channel, depositing their maximum energy in the place where it will cause the most damage. NIEL also does not take the geometry of the CCD into account. Another method of modelling the CTI change was required. The solution was to use the Stopping Range of Ions in Matter (SRIM) program (Ziegler et al. 1985) to model the effect of low energy protons in a representative CCD structure.

5.4.1. Modelling Expected CCD Damage Using SRIM

The SRIM program was first used to model 1000 protons interacting with a representative CCD22 structure at a number of input energies between 0.1 MeV and 100 MeV. Due to the limitations of the SRIM program and the available knowledge of the layered structure of the CCD22, the buried channel was taken to be 0.4 μm wide at a depth of 1.57 μm below the hypothetical CCD surface (Holland 1994, Ambrosi et al. 2002). The input parameters of the model are given in Table 5.3.

Layer	*Material*	*Depth (μm)*	*Thickness (μm)*	*Density (g/cm^3)*
Oxide and VAPOX	SiO_2	0.000 - 0.500	0.500	2.27
Electrode	Si	0.500 - 1.000	0.500	2.33
Nitride Passivation	Si_3N_4	1.000 - 1.085	0.085	3.44
Oxide Protection	SiO_2	1.085 - 1.170	0.085	2.27
Active Region	Si	1.170 - 2.670[a]	1.500	2.33

[a] The buried channel is within this region at a depth of 1.57 μm

Table 5.3 SRIM Monte Carlo model input parameters

The SRIM output data allowed calculation of the percentage of a given input proton's energy deposited into the chosen buried channel volume. The output of this simulation and the fit to the data are shown in Figure 5.7. The fit consists of a Gaussian, representing the standard distribution of energy deposited by protons actually stopping within the CCD buried channel volume, and a split power law representing the NIEL function. The figure shows that protons below 140 keV will not penetrate far enough into the CCD22 structure to reach the buried channel of the CCD, and therefore they will not contribute to an increase in CTI. The largest amount of energy is deposited in the CCD buried channel when the incoming proton has an energy of 223 keV at the surface of the CCD. Figure 5.8 shows data from four of the many SRIM simulations used in the Monte Carlo model. The four panels of the figure show the ionisation tracks of incident protons, with energies of 100, 200, 300 and 1000 keV respectively, interacting with the simulated CCD22 structure. The position of the buried channel is indicated in each panel showing that incident protons of ~200 keV will deposit most of their energy in the vicinity of the buried channel volume. Incident protons of energy >1 MeV pass far beyond the buried channel before depositing the majority of their energy, the resulting displacement damage scaling with the NIEL function.

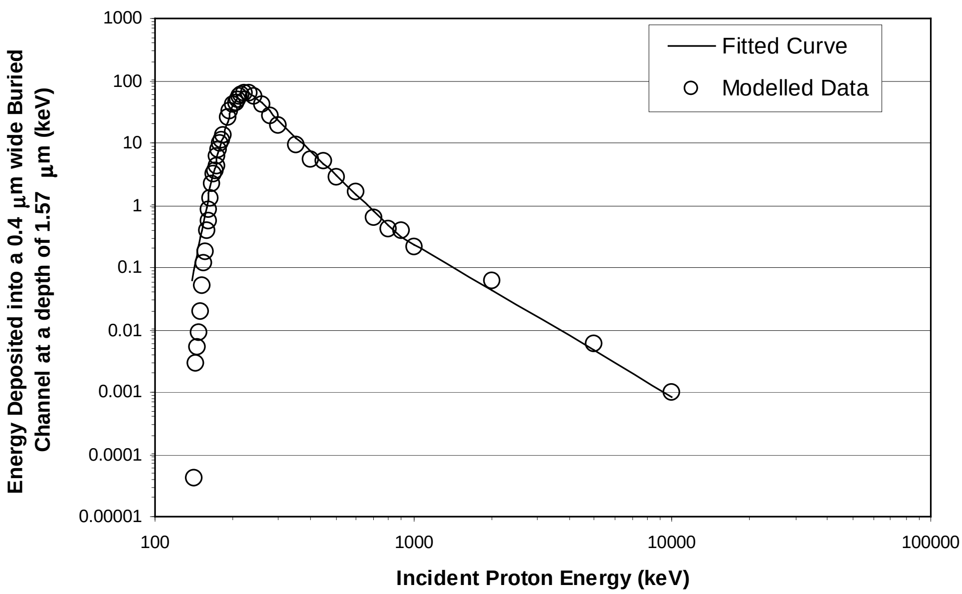

Figure 5.7 The amount of energy deposited into a 0.4 μm wide buried channel at a depth of 1.57 μm from the surface of a representative CCD22 structure as a function of interacting proton energy

If the depth of the CCD22 buried channel is in fact deeper than the modelled depth, then the peak in Figure 5.7 becomes shifted to the right, a converse shift occurring if the depth of the channel is shallower. If the buried channel is narrower, while still fixed at the modelled depth, the peak remains in the same place, but the fraction of energy deposited at each input energy decreases. Conversely, the deposited energy fraction increases if the channel is wider. This emphasises the fact that the radiation hardness of buried channel CCDs scales with the width of the buried channel, as shown by Watts et al. (1994).

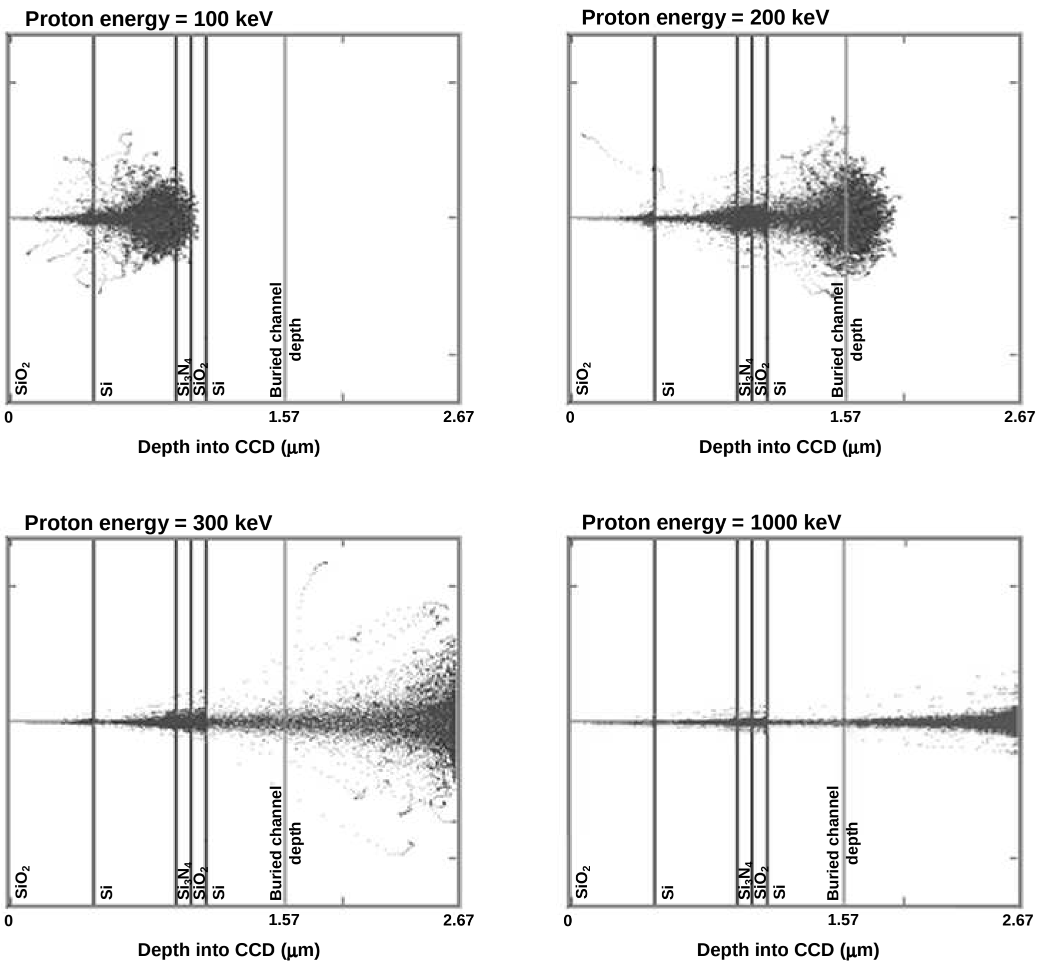

Figure 5.8 The ionisation depth of protons interacting with a representative CCD22 structure over the charge transfer path. The buried channel depth is indicated in each panel, showing that protons of ~200 keV deposit the most energy into the buried channel volume

5.4.2. Modelling CTI

The SRIM model was used in conjunction with the experimentally measured energy spectra to calculate the total amount of energy, E_{bc}, in keV deposited within the specified buried channel volume by the proton beam, given by:

$$E_{bc} = \sum_{1}^{i} \left(N_{bin} E_p \frac{\xi}{100} \right) \tag{5.3}$$

Where i is the total number of energy bins in the spectrum, N_{bin} is the number of counts in each energy bin, E_p is the input proton energy (in keV) associated with the energy bin and ξ is the percentage of the input energy deposited in the buried channel, obtained from the SRIM model.

For each of the CCD22 irradiations E_{bc} was calculated and then used to deduce the 10 MeV equivalent proton fluence, F_{10MeV}, deposited in the buried channel:

$$F_{10MeV} = \frac{E_{bc} A_{irr}}{100 \xi_{10MeV}} \tag{5.4}$$

Where A_{irr} is the area of the CCD irradiated and ξ_{10MeV} is the value obtained from the SRIM model for an input energy of 10 MeV and is 8.57×10^{-6} %.

The corresponding parallel CTI change was then deduced using:

$$CTI = XF_{10MeV} \tag{5.5}$$

Where X is the rate of change of CTI with proton dose for an EPIC MOS CCD operating at -100 ^{o}C. In this case $X = 1.62 \times 10^{-14}$ and was determined experimentally in a study by Ambrosi et al. (2002), where an EPIC MOS CCD was exposed to increasing doses of 10 MeV protons and the CTI was measured as a function of progressive amounts of damage. Linear relationships between CTI change and proton dose have also been reported by Watts et al. (1994).

5.5. Experimental Results

Two CCDs were irradiated with varying proton energy distributions. The CTI for each device was measured prior to each irradiation and for device B5/21 this is shown in panel A of Figure 5.9. Panel B shows the change in CTI of the same device after irradiation with a proton spectrum passing through the 13 μm aluminium foil. Panel C shows a more dramatic CTI change observed when the device was exposed to a spectrum of protons that could inflict more damage to the buried channel, while panel D confirms that as the number of protons that can contribute damage in the buried channel increases, the CTI increases. No new bright pixels were present in the two devices after irradiation, operating at -100 ^{o}C.

The ^{55}Fe calibration source illuminating the image section of the CCD was used to determine changes in the resolution of the Kα peak at 5898 eV after irradiation through the 12 μm aluminium foil as a function of proton dose. The intrinsic resolution prior to damage was measured to be ~150 eV. The increase in CTI degraded the resolution to ~170 eV, a 13 % reduction.

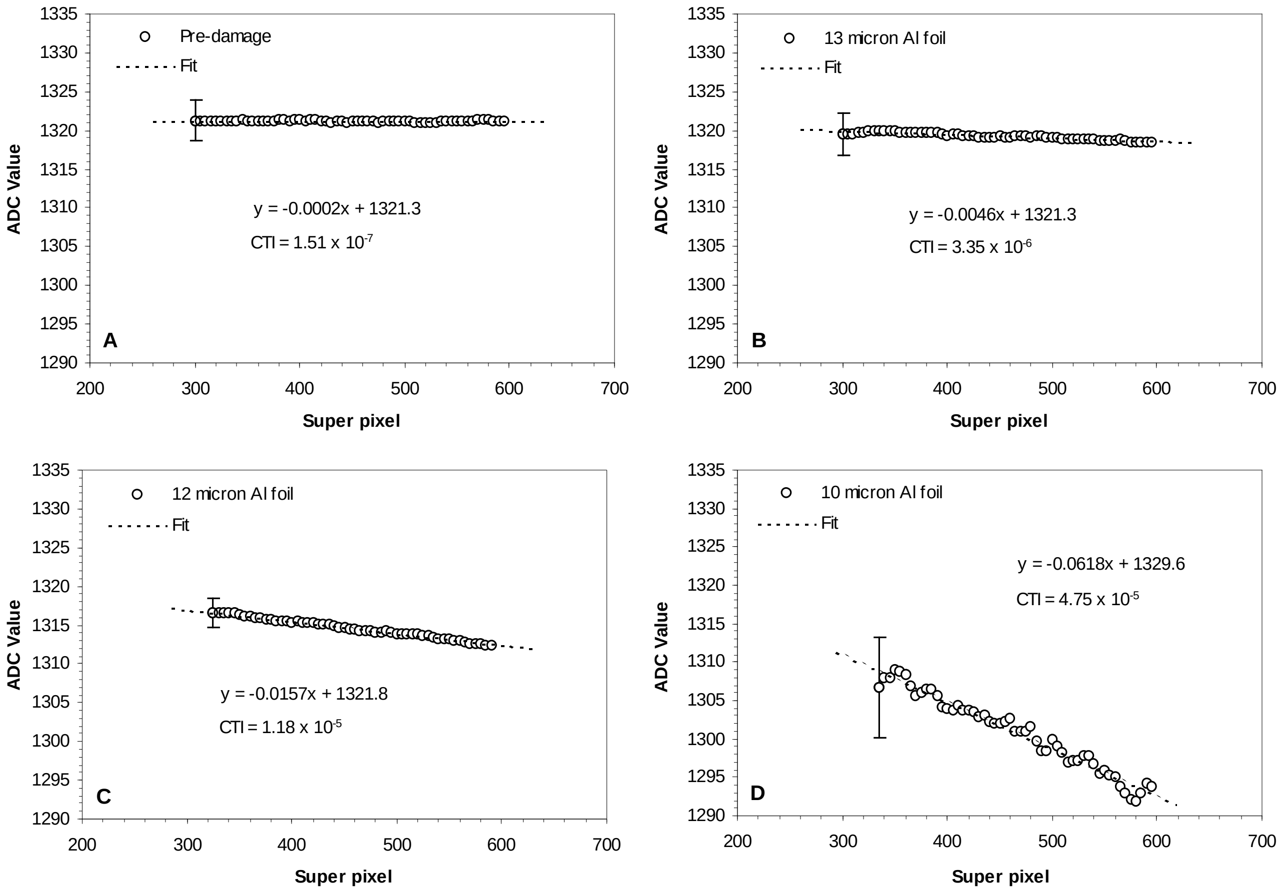

Figure 5.9 The four panels depict the measured CTI before and after proton irradiation of device B5/21 through different thickness aluminium foils. The error bar in each panel is the same for each data point in that panel. Pixels have been binned in fives to create 'Super Pixels'

5.5.1. Comparison of Model and Experiment

The experimental and modelled CTI results for the irradiated devices are compared in Table 5.4.

CCD	*Al Foil Thickness (μm)*	*Mean Proton Energy (keV)*	*Experimental CTI Change (±5%)*	*Modelled CTI Change (±20%)*	*Ratio (±25%) (Experimental/Modelled)*
B5/21	13	70	3.35×10^{-6}	2.55×10^{-6}	1.3
B5/21	12	170	1.18×10^{-5}	6.79×10^{-6}	1.7
B5/21	10	330	4.75×10^{-5}	6.13×10^{-6}	7.7
B5/19	14	10	9.20×10^{-7}	5.34×10^{-8}	17.2
B5/19	12	170	5.25×10^{-5}	3.32×10^{-6}	15.8

Table 5.4 Comparison of experimental and modelled CTI changes

The differences between modelled and experimental CTI values were as expected. The modelled values are a lower limit for the CTI owing to the fact that the input spectra are incomplete, for example the spectrum associated with the 12 μm foil, stops at 182 keV. The full spectra will have a higher proton energy component traversing the CCD, depositing a small amount of additional energy in the buried channel and this would account for part of the difference. The difference between modelled and experimental CTI values may also be explained if the representative CCD22 structure and the location and width of the CCD buried channel are slightly different to the parameters used in the model. Figure 5.10 shows how changing the modelled buried channel width, or depth below the CCD surface, affects the percentage of the input proton's energy deposited into the buried channel volume. Device B5/19 was taken from a different silicon wafer than that of B5/21 most likely resulting in the buried channel of one device being wider or in a slightly different location to that of the other (Gardiner 2003). This explains why the experimental to modelled ratios for device B5/19 are higher than those for device B5/21. The increase in experimental to modelled ratio for the 14 μm foil irradiation of device B5/19 is due to the 'double peak' occurring in the input spectrum to the SRIM model caused by saturation of the ADC.

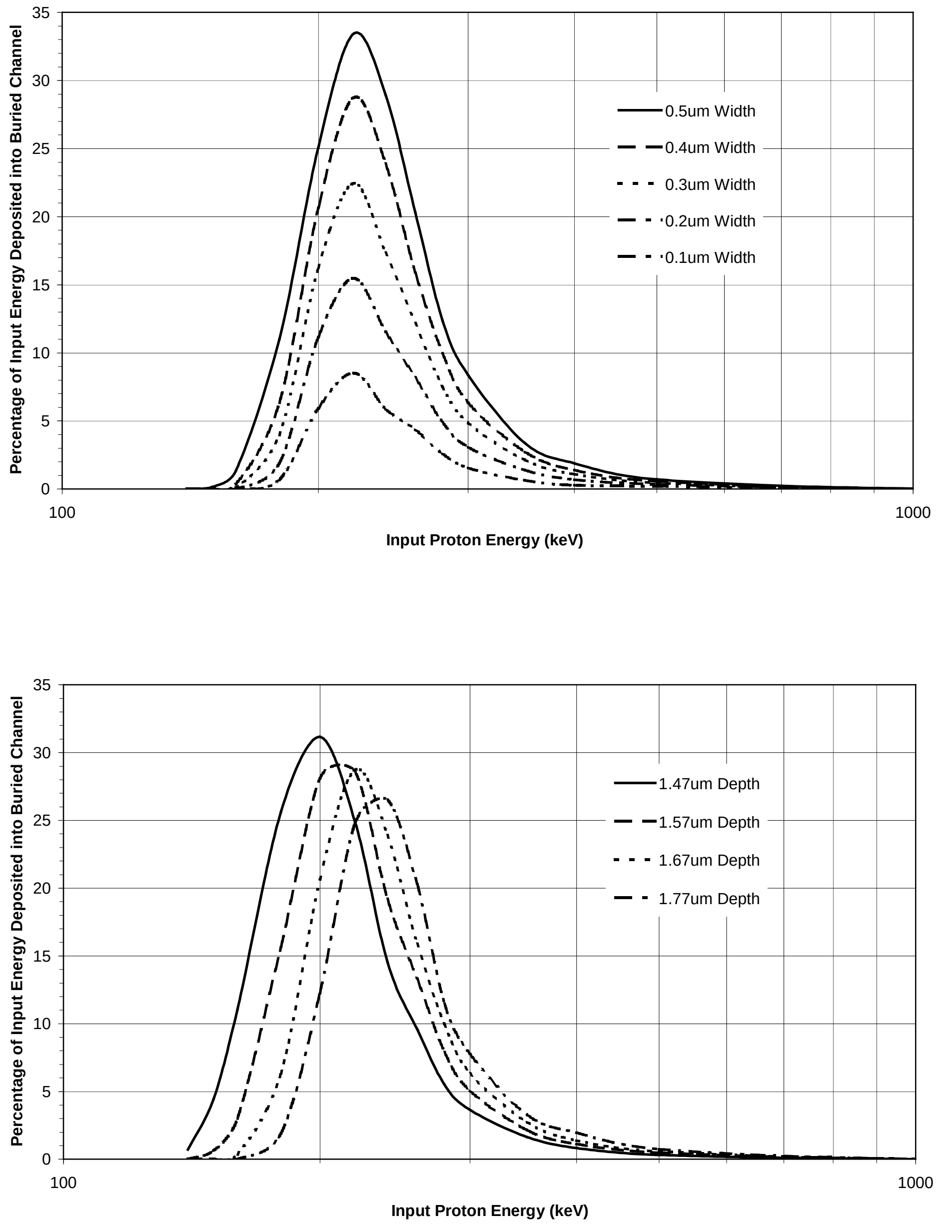

Figure 5.10 The effect of varying buried channel width and depth below the CCD surface on the amount of energy deposited in the buried channel

5.6. Discussion

Soft protons of a few hundred keV can rapidly damage the charge transfer capabilities of CCD22 devices due to the higher cross sections associated with protons of energies below 900 keV. This is emphasised by the Monte Carlo model developed for this study, which showed the greatest amount of damage to the buried channel is associated with the highest amount of energy deposited within it. For an input proton energy of ~220 keV most of these particles will come to rest in the CCD buried channel, causing maximum damage. As the input proton energy increases, the fraction of energy deposited in the buried channel decreases and hence larger doses are required to produce the same observed amount of damage.

The results of on-orbit CTI measurements for both MOS cameras onboard XMM-Newton over the first 1070 days of the mission have now been documented. All 7 CCDs of both the MOS 1 and MOS 2 cameras show a steady increase in CTI over the current duration of the mission. Figure 5.11 shows the gradual increase in parallel transfer losses for Mn-Kα X-rays, for CCD 1 of MOS 2. The general 'slope' of the data is due to displacement damage caused by protons in the radiation belts. XMM-Newton passes through the Earth's radiation belts during each 48 hour revolution, each time encountering some high energy protons that have enough energy to penetrate the shielding around the detectors and cause displacement damage in the CCDs. The larger 'steps' in the data are associated with periods of increased solar activity where displacement damage is caused by high energy solar protons. Figure 5.11 also indicates parallel loss values recorded during charge injection and cooling tests. The charge injection test was carried out in revolution 330 and showed that the technique could reduce the CTI by ~50 % (Abbey 2002). The use of charge injection did not restore the CTI to the pre-launch value and also introduced 10 – 200 additional bright pixels into the CCD frames recorded when charge injection was used. The cooling test in revolution 448 was used to investigate the change in CTI resulting from a decrease of 20 ^{o}C in the operating temperature of the EPIC CCDs from -100 ^{o}C to -120 ^{o}C (Abbey et al. 2002). This technique reduced the CTI by slightly more than 50 % and after revolution 533 was implemented permanently, indicated by the last two measurements in Figure 5.11.

The average CTI values associated with MOS 1 and MOS 2 at day 580 were 1.3×10^{-5} and 1.7×10^{-5} respectively (Bennie 2001). Estimates made by Kendziorra et al. (2000) from solar event spectrum measurements made with the pn-CCD camera at that time, showed the MOS cameras should have received doses of ~10^{5} protons cm^{-2}, where the proton energy was estimated to be between 100 keV and 200 keV. By folding a value between 1×10^5 protons cm^{-2} and 2×10^5 protons cm^{-2} through the SRIM model, the equivalent 10 MeV fluence can be calculated and hence the expected CTI, which in this case lies between 7.3×10^{-6} and 1.5×10^{-5}. The upper limit of this range is within the average CTI changes for the two MOS cameras, quoted by Bennie (2001).

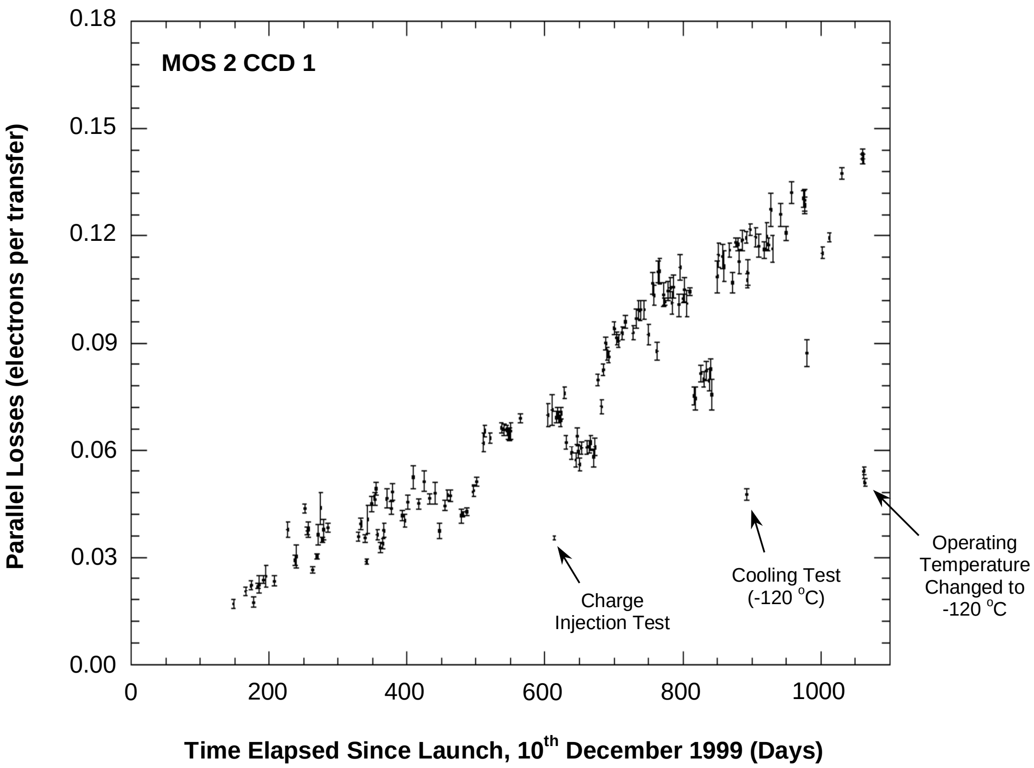

Figure 5.11 On-orbit measurements of the Mn-Kα parallel transfer losses of MOS 2 CCD 1 as a function of time

Figure 5.12 shows the average CTI trend over the duration of the mission for the 7 CCDs of MOS 2. The on-orbit trend is extrapolated from day 1066 after the operational temperature was reduced to -120 °C using the CTI value obtained for the cooling test in revolution 448 and the CTI values obtained since the change in operational temperature. For comparison, the dashed line of the figure shows the 90 % confidence level CTI trend that was predicted before launch for operation of the MOS CCDs at -120 °C. This predicted trend was based on CCD22 irradiation tests carried out before the launch of XMM-Newton that concluded the CTI after 7 years of operation should be ~2×10^{-5}. The measured trend at -120 °C is below the level predicted before launch, indicating that soft protons only account for a minor fraction of the observed CTI increase, <20 %, the MOS CCDs being subjected to a predominantly hard proton spectrum. This low level of soft protons indicates that the operation of the spacecraft with regard to preventing soft protons reaching the CCD detectors is optimal and no operational changes need to be made. As reported by Kendziorra et al. (2000), the EPIC pn-CCD detector on XMM-Newton was used to measure the proton spectra of solar events and the results showed typical fluxes of 0.2 protons cm^{-2} s^{-1} between 100 keV and 200 keV. Given these measurements, it would take 2.5×10^6 s (~29 days) of continuous staring at such events to sustain the total changes in CTI given in Table 5.4.

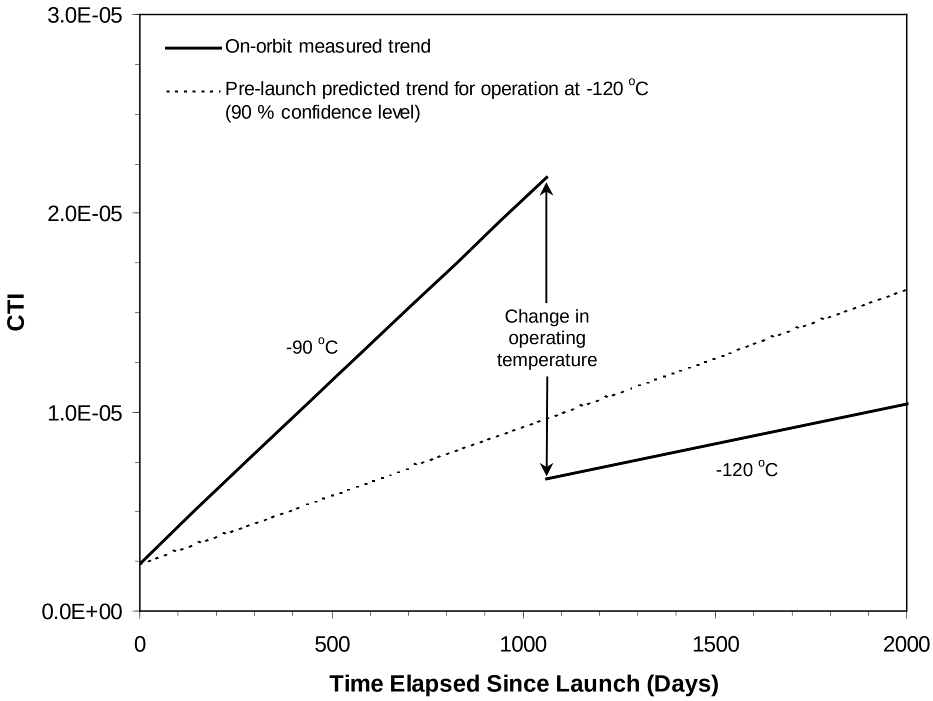

Figure 5.12 The pre-launch predicted and on-orbit measured Mn-Kα parallel CTI change over time for the CCDs of MOS2

5.7. Summary

This chapter has described an investigation into the effects of low energy protons on CCD22 devices, the same devices as those used in the EPIC MOS detectors of the XMM-Newton spacecraft. The CCD22 structure and irradiation methodology have been presented followed by a detailed discussion of the radiation damage induced CTI changes caused by the irradiations. The development of a computational model to simulate the CTI changes that resulted from the proton irradiations has also been presented and shown to produce useful results. The soft proton damage component to the on-orbit CTI measurements taken from the EPIC MOS devices was found to be small, the current operation of the spacecraft during solar events being sufficient to keep the observed CTI change comparable to that expected pre-launch. The next chapter presents a detailed investigation of a specific radiation induced phenomenon, that of fluctuating bright pixels. The irradiation of two CCD47-20 devices is described, followed by an in-depth analysis of the collected data and a discussion of several models put forward to explain the mechanism behind fluctuating pixels.

Chapter 6: Random Telegraph Signals

This chapter investigates fluctuating pixels resulting from proton irradiation of two E2V Technologies CCD47-20 devices. The device structure is described first followed by a description of the experimental set up and the irradiations carried out. A preliminary study of one device is then presented followed by a detailed investigation of fluctuating pixels in the second device. The characteristics of flickering pixels are discussed in detail and the proposed models explaining the mechanism behind the phenomenon are viewed in light of the collected data.

6.1. Introduction

The generation of bright pixels as a result of irradiation of a CCD has been discussed in the preceeding chapters of this thesis. This chapter deals with a specific type of radiation-induced bright pixel; those observed to have a fluctuating charge level. The apparent random nature of the fluctuation period has resulted in such pixels being called ‘flickering pixels’ which are said to exhibit ‘Random Telegraph Signal’ (RTS) behaviour. The term RTS has also been applied to ‘flicker’, or ‘1/f’ noise, as described in Chapter 2 (Kandiah 1985, Kandiah et al. 1989). Flicker noise, however results from electron and hole emission and capture from interface traps adjacent to the channel region of any CCD FETs, while the RTS phenomena under study in this chapter are shown to result from bulk traps, showing well defined time constants and characteristics independent of the surface conditions of the CCD. Little study has been made of the RTS phenomenon, the main reference sources for information being the published papers by Hopkins and Hopkinson (1993, 1995) whose investigation of RTS was initiated as a result of other authors reporting CCD pixels exhibiting fluctuating dark current levels (Srour et al. 1986, Marshall et al. 1989).

The period of amplitude fluctuation is shown later in this chapter to be proportional to the temperature of the CCD. As the operational temperature of a device is reduced, the mean time constants for the low and high amplitudes of the fluctuation are increased. CCDs used in X-ray applications are usually cooled to around -100 ^{o}C where the mean time constants are of order several days and will not cause significant concern in the collection of data. RTS pixels are however still observed at such low temperatures, for example 5 % of background events in the MOS 2 camera of XMM-Newton, operating at -120 ^{o}C, are the result of flickering pixels in 5 of the 7 CCDs (Ballet 2003). At temperatures above -20 ^{o}C the time constants become of order hours and start to become more of a problem in data analysis. RTS has already caused significant problems for the optical CCD detectors of the GOMOS instrument on the ENVISAT satellite and may also become more significant in future X-ray missions where the trend is for warmer operation CCDs, for example the Demonstration of a Compact Imaging X-ray Spectrometer (D-CIXS) instrument on the SMART1 mission to observe the Moon and its subsequent development for the Bepi Colombo mission to Mercury.

The mechanism behind RTS is still not well understood and the work described in this chapter was initiated to provide information to improve the current proposed models of RTS. This chapter first describes the CCD47-20 devices used for the study and the proton irradiations carried out before describing the techniques used to characterise the resulting pixels exhibiting RTS behaviour.

6.2. CCD47-20 Structure

The E2V Technologies CCD47-20 is a front illuminated frame transfer device that can be operated in inverted mode to suppress dark current. The image and store sections of the CCD each contain 1024 × 1024 pixels of 13 μm square. The device characteristics are summarised in Table 6.1.

Active image area		13.3 × 13.3 mm
Image section		1024 × 1024 pixels
Store section		1024 × 1024 pixels
Pixel size:	Image section	13.0 × 13.0 μm
	Store section	13.0 × 13.0 μm
	Readout register	13.0 × 13.0 μm
Epitaxial silicon thickness		20 μm
Resistivity		20 – 30 Ω cm
Spectral range		400 – 1100 nm

Table 6.1 E2V Technologies CCD47-20 characteristics

6.3. Irradiation of CCDs

Irradiation of one CCD47-20, device number 9211-5-3, was carried out using the Birmingham University cyclotron facility described in Chapter 4. The same dosimetry techniques were again used, the error associated with the dosimetry of each irradiation taken to be ~20 %. Two irradiations were carried out with CCD 9211-5-3 at room temperature. A 6.5 MeV proton beam was used to give a 10 MeV equivalent proton fluence of 1.5×10^8 protons cm^{-2} to one third of the CCD. The rest of the CCD was covered with an aluminium shield to prevent the protons damaging that part of the device. It should be noted that the store section of the CCD47-20 has its own aluminium shield, although this is not thick enough, ~1μm, to stop the protons passing through it.

A second irradiation was carried out with two thirds of the CCD shielded with aluminium while the rest of the device was irradiated through 100 μm of copper foil. The copper had the effect of reducing the mean energy of the proton beam to 2.0 MeV. The same flux of protons was given to the CCD as for the 6.5 MeV irradiation. The 10 MeV equivalent proton fluence given in this case was 3.6×10^8 protons cm^{-2}. For the second irradiation the photodiode was also covered with 100 μm of copper in order to measure the same proton flux and mean energy as that reaching the CCD. The central part of the CCD remained unirradiated as a control area. The shielding regime and 10 MeV equivalent proton dose received by each area of device 9211-5-3 are shown in Figure 6.1. The exposure time for each irradiation was ~80 seconds.

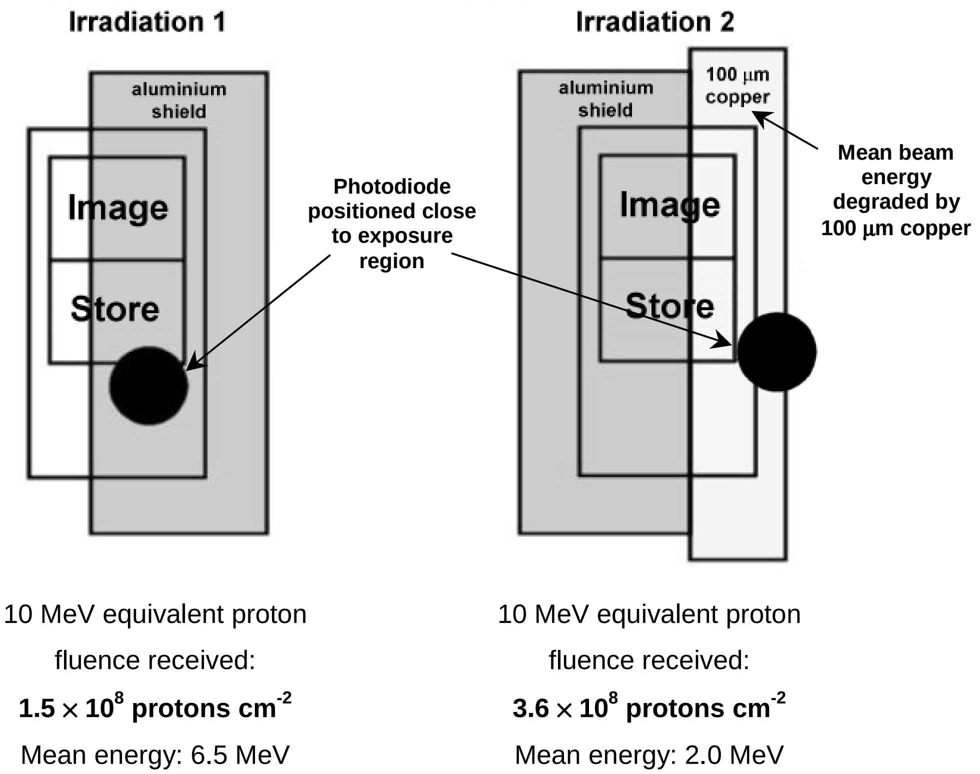

Figure 6.1 A schematic showing the proton irradiated areas of device number 9211-5-3 and the associated 10 MeV equivalent proton doses received

A second CCD47-20, device number 9211-4-4, was irradiated using the dedicated 10 MeV proton damage beam line at the tandem Van de Graaff accelerator facility run by AEA Technologies in Harwell, UK. Figure 6.2 shows a schematic of the Harwell beam line.

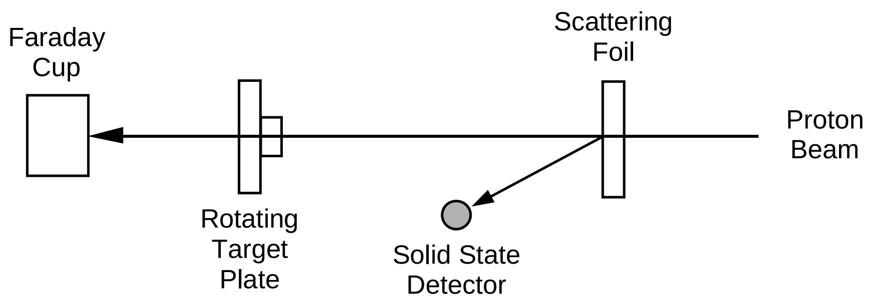

Figure 6.2 A schematic of the Harwell tandem Van de Graaff beam line

Before irradiation, an even distribution of protons across the target area was achieved and verified by use of a series of scattering foils. By rotating the sample plate out of the beam, the charge accumulated in the Faraday cup at the end of the beam line and the number of scattered particles in the solid state detector were used to determine the number of particles reaching the target area. This calibration was carried out by Harwell staff and was used to determine the exposure time needed to give the required proton dose to the target detectors. The dosimetry error associated with each irradiation was taken to be ~20 % based on the beam uniformity measurements. An E2V Technologies CCD02 device was also irradiated in the same way as the CCD47-20 device to provide a rough check that the proton flux received was in agreement with previous irradiation studies.

The CCD was mounted onto the sample plate and rotated into the proton beam for irradiation, with all CCD pins grounded to avoid static damage. The irradiation was carried out at room temperature under vacuum. The shielding regime and 10 MeV equivalent proton dose received by the irradiated area of device 9211-4-4 are shown in Figure 6.3. The exposure time for the irradiation was ~10 seconds.

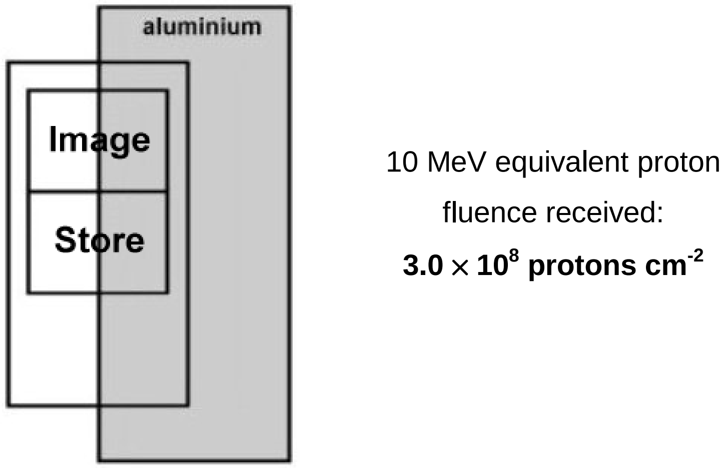

Figure 6.3 A schematic showing the proton irradiated area of device number 9211-4-4 and the associated 10 MeV equivalent proton dose received

6.3.1. Dark Current Changes

The mean dark current level increased in the areas of each CCD that were irradiated. Figure 6.4 shows the average pixel amplitude in each column of the two CCDs which scales with the mean energy and the fluence of the protons received by each irradiated area. The increase in dark current resulting from the 1.5×10^8 and 3.0×10^8 10 MeV equivalent proton doses given at the two different accelerator facilities are comparable to within the 20 % dosimetry error. The dark current increase in the area of device 9211-5-3, irradiated through 100 μm of copper foil, is far higher due to the very large number of bright pixels generated by the 2.0 MeV protons increasing the average pixel amplitude in these columns. The 'curve' of the line in the 2.0 MeV irradiated region is due to the copper foil being positioned at a slightly off vertical angle across the device. At a temperature of 24 ^{o}C, the unirradiated region in the centre of device 9211-5-3 had a dark current level of ~2600 electrons, while the dark current levels for the 6.5 MeV and 2.0 MeV mean proton energy irradiations were ~3400 electrons and ~14,000 electrons per pixel respectively. The dark current level of device 9211-4-4 increased from ~2200 to ~2900 electrons.

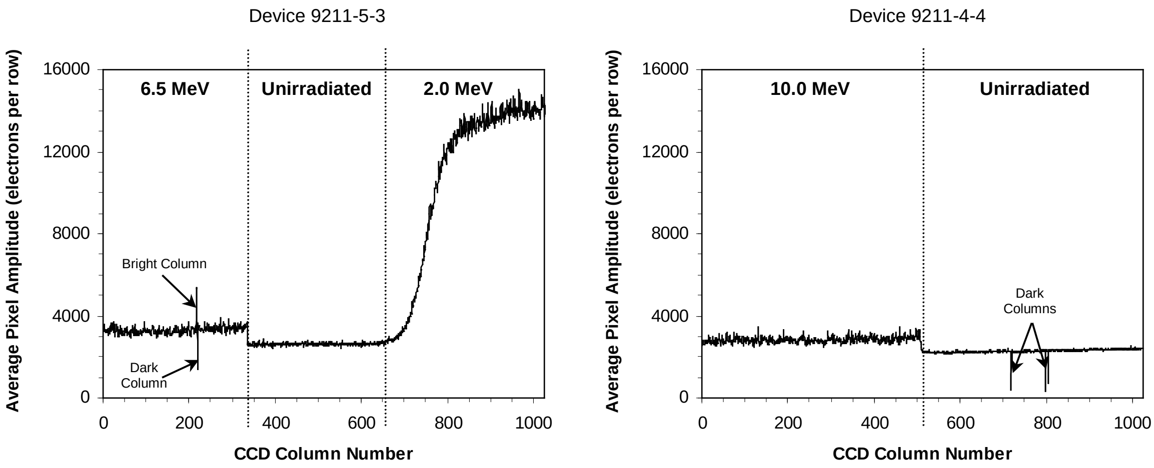

Figure 6.4 Each graph shows the average pixel amplitude of 1000 rows in the image section of the proton-irradiated CCDs

6.4. Preliminary RTS Study

An initial RTS analysis of device 9211-4-4 was carried out to assess the general characteristics of the radiation-induced RTS pixels. This information was then used as a basis for the development of CCD sequencer and analysis software designed for a more detailed study of device 9211-5-3. The 600 brightest pixels of the CCD were selected and monitored every 12 seconds over a period of 12 hours. The CCD was stabilised at a temperature of -10 ^{o}C during data collection. Of the 600 pixels studied, 342 were found to exhibit a fluctuating charge level. Figure 6.5 shows a section of the irradiated area of the CCD showing the uniform spread of the observed bright pixels and fluctuating pixels resulting from the irradiation and demonstrating the uniformity of the Harwell proton beam.

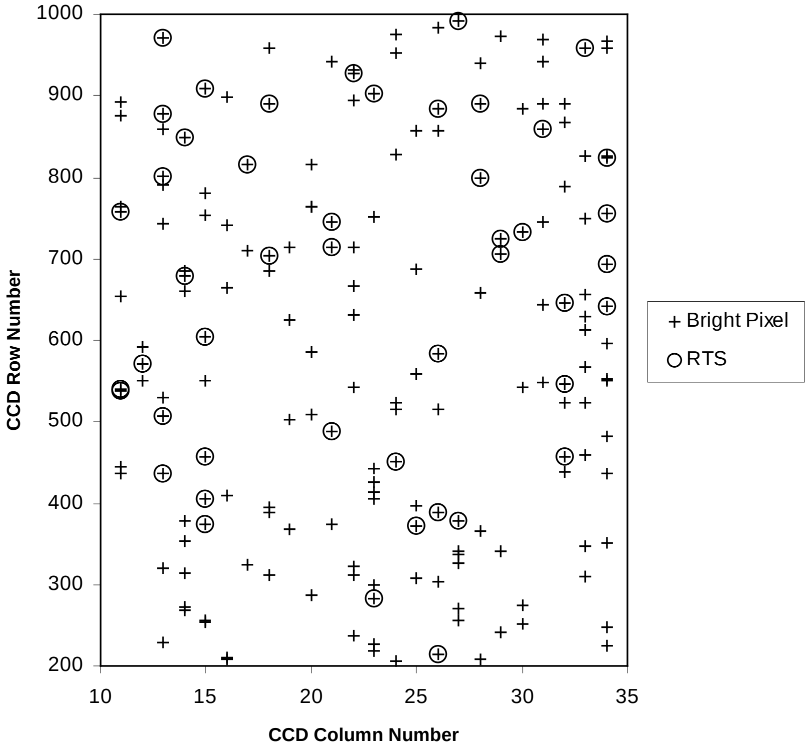

Figure 6.5 The post-irradiation distribution of bright pixels and fluctuating pixels in device 9211-4-4

A number of different types of fluctuation were observed that could be classified into one of five different categories. For each classification the amplitude of the oscillation or transition was above 5σ of the mean pixel level of a ‘Flat’ reference bright pixel, where σ was 50 electrons, and the noise distribution was Poissonian in nature. The categories were called: Wave, Bi-Stable, Multi-Stable, Bi-Stable with Wave, and Stable. The characteristics of each are described below:

- Wave: The pixel amplitude varies with a sinusoidal oscillation.

- Bi-Stable: The pixel shows sharp amplitude transitions between 2 distinct levels.

- Multi-Stable: The pixel shows sharp amplitude transitions between more than 2 distinct levels.

- Bi-Stable with Wave: The pixel shows sharp amplitude transitions between 2 distinct levels while the amplitude also varies in a sinusoidal fashion.

- Flat: The pixel shows no oscillatory nature, or transitions, that are visible above the pixel noise.

Examples of each fluctuation type are shown in Figure 6.6, spaced out to avoid overlap. Gaps in the data were caused by loss of frame synchronisation for short periods during data collection. The number of pixels in each of the five categories is shown in Table 6.2.

Classification	*Number of Pixels*	*% of Total Pixels*
Stable	258	43.0
Wave	71	11.8
Bi-Stable	150	25.0
Multi-Stable	22	3.7
Bi-Stable with Wave	99	16.5
Total	600	100

Table 6.2 The number of pixels exhibiting different types of fluctuation, from a total sample of 600 pixels

The pixels classified as 'Bi-Stable' pixels in this study were RTS pixels exhibiting standard RTS behaviour (Hopkins and Hopkinson 1993), the amplitude of the pixel switching between two distinct levels. The high and low state time constants were predominantly of order several tens of minutes to hours at the -10 ^{o}C monitoring temperature. This is in agreement with previous work that investigated the affect of temperature on RTS pixels, showing that the time constants increase as the temperature is lowered, the time between amplitude changes becoming many hours and even days when operating at -20 ^{o}C (Hopkins and Hopkinson 1995).

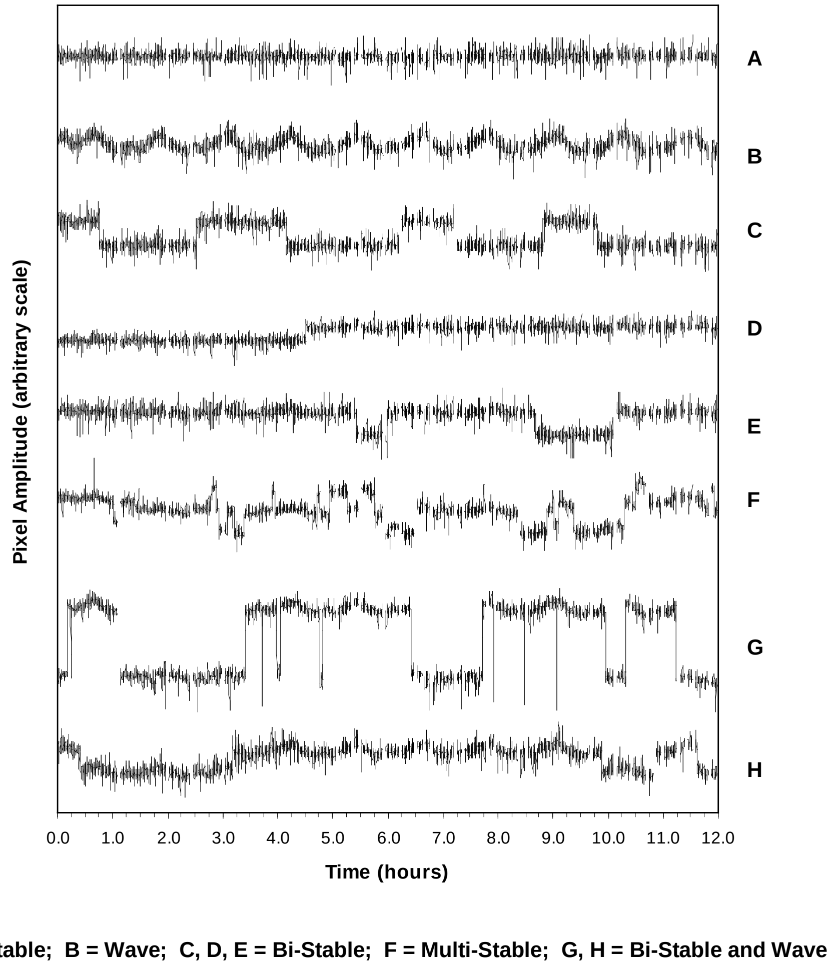

Figure 6.6 Examples of recorded random telegraph signals from a CCD47-20 operating at a temperature of -10 ^{o}C

Pixels showing more than two distinct amplitude levels were also observed and classified as 'Multi-Stable' pixels. Of the RTS pixels generated after proton irradiation, ~3.5 % were 'Multi-Stable'. This is comparable to measurements made in previous studies where the fraction of generated RTS pixels exhibiting multi-stable behaviour after irradiation with different 10 MeV proton doses was found to be between ~1 % - 15 % (Bond 1996).

The smooth oscillation observed in a number of pixels had a period of ~70 minutes, and was due to thermal drift introduced by the temperature controller. The amplitude of the oscillation increased proportionally with the mean pixel dark current level, becoming visible above the noise in all pixels with a mean dark current level above ~2200 electrons. The oscillation is not a radiation induced effect, and removing the 'Wave' classification from the collected data reveals that ~45 % of the monitored pixels had generated RTS characteristics. This is in good agreement with a study involving E2V Technologies CCD02 and Hamamatsu S5466 CCDs irradiated with neutrons (^{252}Cf), where the fraction of generated bright pixels exhibiting RTS properties was found to be 40 % (Stefanov 2001).

6.5. Development of Analysis Software

The results obtained from the preliminary study indicated that the RTS pixels were behaving as expected but also indicated ways of improving the method of analysis. Better temperature control hardware was obtained to remove unwanted oscillations from the data, while a novel CCD sequencer program was developed to remove the synchronisation problem causing data loss and decrease the time between samples to 0.25 seconds. The reduction in the sample time was to ensure that high frequency transitions were adequately sampled. Another practical problem encountered during testing was the amount of time required to obtain large data sets for statistical analysis. Previous studies have shown that the time constants of RTS pixels decrease with increasing temperature (Hopkins and Hopkinson 1993). The same number of switches from high to low charge state can be observed in ~1 hour at 45 ^{o}C compared with 12 hours at -10 ^{o}C. The data collected from device 9211-5-3 was therefore taken at temperatures in the range 45 ^{o}C to 55 ^{o}C.

The new CCD sequencer code allowed readout of individually selected CCD rows in 0.25 second intervals. The resulting images revealed any RTS pixels in the CCD, showing the variation in pixel amplitude over time for each pixel in the selected row of the device. Figure 6.7 shows an example of a recorded CCD image taken at 55 ^{o}C using the RTS analysis sequencer program.

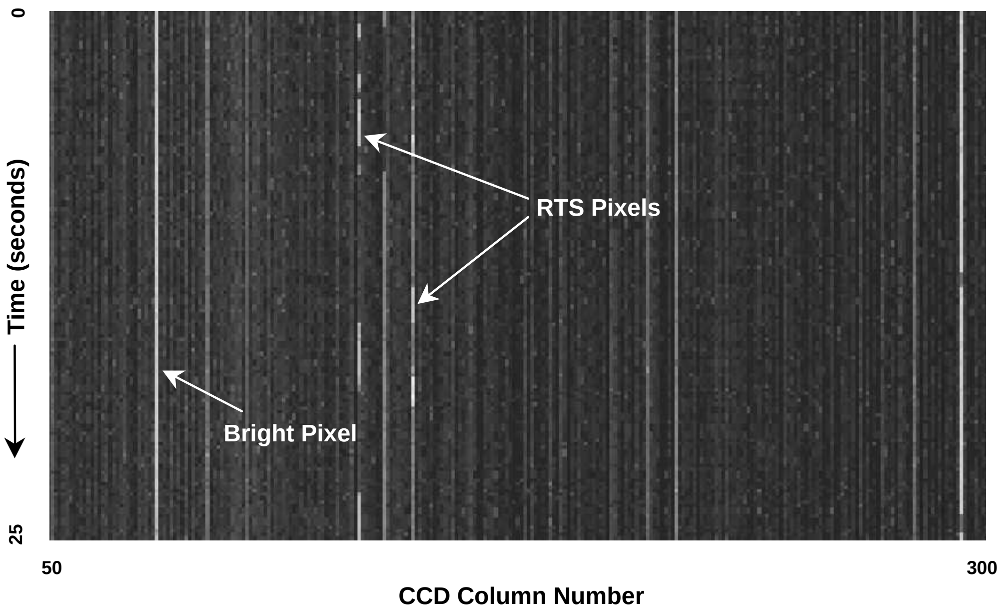

Figure 6.7 An image taken using a sequencer program that only reads out pixels in a selected row of the CCD. Each row in the image is recorded at 0.25 second intervals revealing the change in amplitude over time of RTS pixels

Each column in the recorded images was then input into RTS analysis software that characterised the number of distinct amplitude levels present by convolving the measured amplitude spectrum with a matched Gaussian and observing the number of peaks and troughs in the gradient of the convolution. The matched Gaussian was generated by fitting a Gaussian function to the average amplitude spectrum of 10 ‘stable’ pixels. The raw data and the fitted Gaussian function are shown in Figure 6.8. The analysis software allowed the association of each CCD pixel with a number of distinct amplitudes, giving the mean ADC value of each amplitude level and the time between amplitude switches. The four panels of Figure 6.9 illustrate the output from the RTS analysis software showing the raw pixel amplitude variation over time, the measured amplitude spectrum, the convolved amplitude spectrum and the gradient of the convolution. The raw data used for the figure is that of a 2-level RTS pixel, the two distinct amplitude levels being clearly resolved by the analysis software.

The following bullet points summarise the steps taken to characterise RTS pixels:

- CCD row selected and RTS sequencer used to obtain an image of the amplitude variation over time of all the pixels in the row

- Each column from the recorded image is read into the RTS analysis software

- Variation in pixel amplitude over time plotted

- Amplitude spectrum recorded and plotted

- Amplitude spectrum convolved with a matched Gaussian function and plotted

- Gradient of the convolution plotted and used to determine the number of distinct amplitude levels present

- Time between amplitude switches recorded for each distinct amplitude level

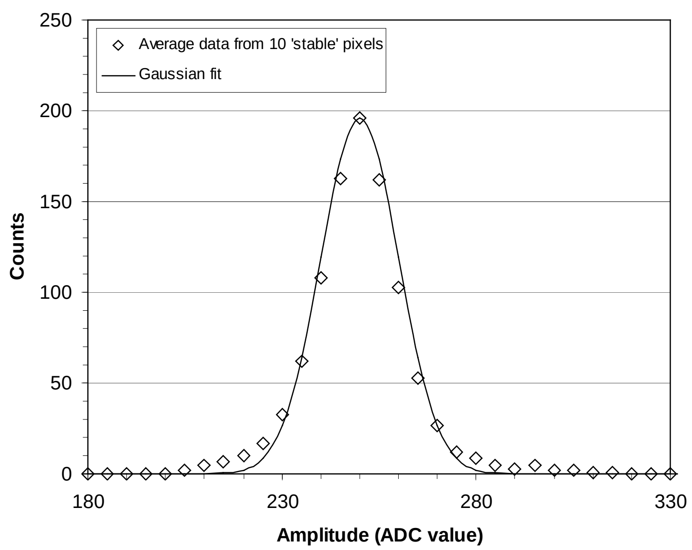

Figure 6.8 The average amplitude spectrum of 10 ‘stable’ CCD pixels fitted with a Gaussian function. The fit shown has a σ of 10 and was used as the matched Gaussian in the RTS analysis software

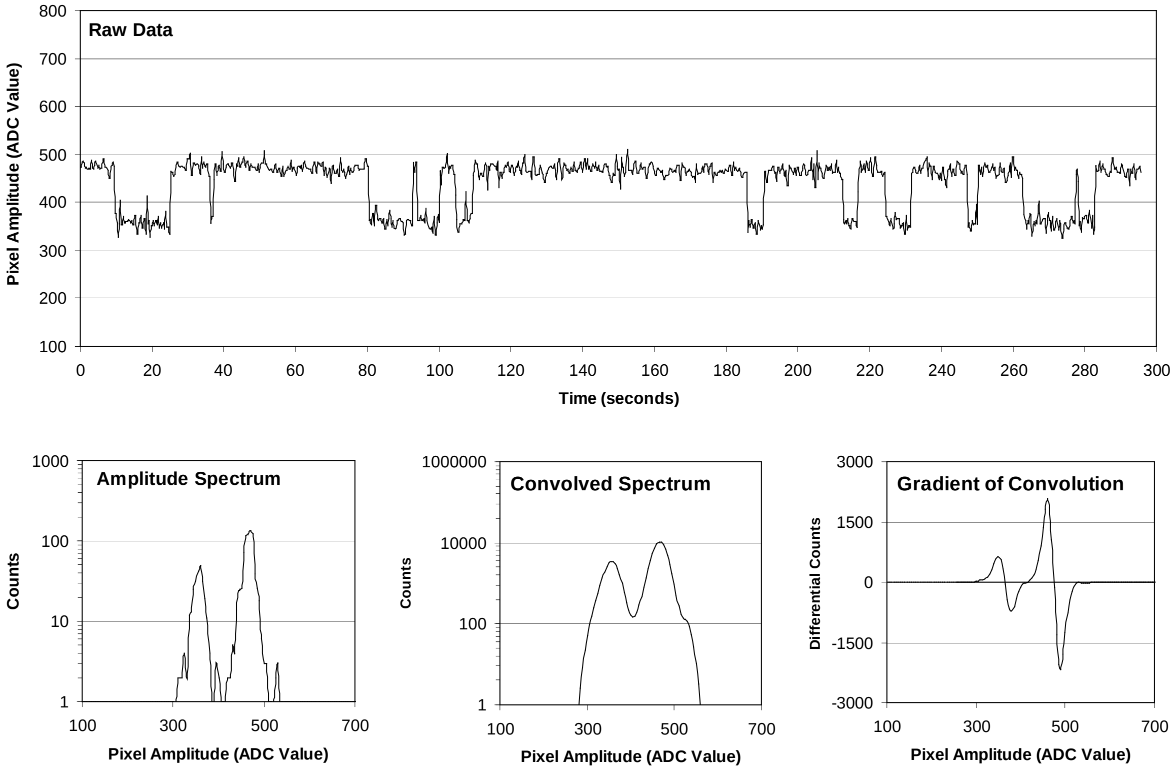

Figure 6.9 Output from the RTS analysis software showing the sensitivity of the software to picking out the number of distinct amplitude levels present in the raw pixel amplitude data. The raw data was recorded with the CCD operating at 55 ^{o}C

6.6. Characterisation of RTS Pixels

6.6.1. General Properties

From a sample of 1800 pixels in the 3.6×10^{8} protons cm^{-2} irradiated region of device 9211-5-3, the number of RTS pixels and the number of distinct amplitude levels in each RTS pixel were recorded. The number of amplitude levels was investigated to determine if the occurrence of RTS pixels with more than two amplitude levels scaled with the statistical probability of more than one RTS defect occurring in a given pixel. If the measured number of 3 or 4 level RTS pixels was the same as the number expected by the statistical probability, all fluctuating pixels should be the result of one or more 2-level transitions within a given pixel. If the observed number of RTS pixels with more than two amplitude levels was significantly greater than the expected number it would indicate that RTS pixels with more than two levels are the result of additional processes.

Figure 6.10 shows the variation in amplitude with time for an RTS pixel with more than 2 distinct amplitude levels.

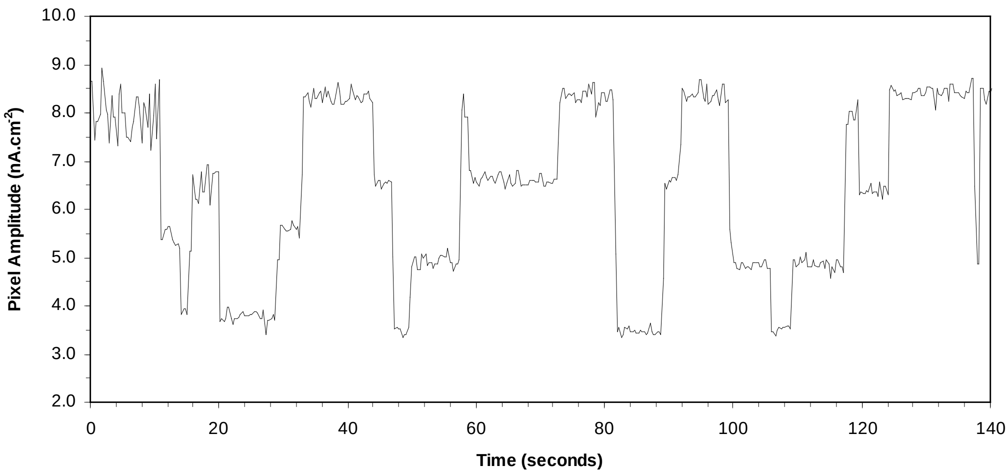

Figure 6.10 Amplitude variation with time of a multi-level RTS pixel at 50 ^{o}C

An amplitude spectrum was obtained from raw data collected at 50 ^{o}C for each RTS pixel and the RTS analysis software used for the detection of distinct amplitude levels. Figure 6.11 shows the measured distribution of RTS pixels with 2, 3, 4 and 5 amplitude levels and the statistically expected fraction that should be present if the explanation for 3-level or 4-level RTS pixels is simply that two 2-level RTS phenomena are located within the same pixel. The observed number of pixels showing more than two distinct amplitude levels is significantly below the expected value due to the level of noise in the data reducing the detection efficiency. Detection thresholds from 5σ to 10σ were investigated, all producing data with the same power law fit. No clear evidence that additional processes are responsible for the higher number of amplitude levels observed was found, the most likely explanation for multi-level RTS being a number of 2-level RTS phenomena residing in a single pixel.

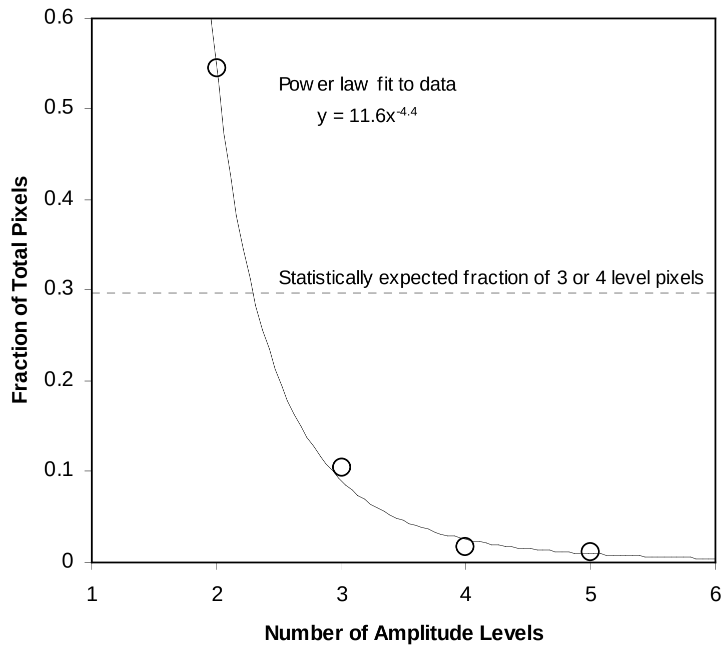

Figure 6.11 The fraction of RTS pixels exhibiting 2, 3, 4 and 5 distinct amplitude levels

To deduce if the RTS phenomenon could be linked to the high field regions within a CCD pixel, the 'event' size of the bright pixels containing RTS was investigated. If a high proportion of RTS pixels were found to be located in single pixel events it would indicate that the defect causing RTS is located in the inter-electrode or the channel stop high field regions, where it is very difficult for charge to diffuse into adjacent pixels. If a large proportion of horizontal or vertical split events were observed, the defect causing RTS may be concentrated in the lower field regions of a pixel, where the charge generated can diffuse into adjacent pixels before being collected into the charge storage region.

From a total of 921 RTS pixels observed in the 1.5×10^8 protons cm^{-2} irradiated region of device 9211-5-3, only a very small number of the RTS pixels were located adjacent to another bright pixel. Figure 6.12 shows the percentage of the observed RTS pixels having different 'event' sizes. The number of 2 pixel events is consistent with the probability of obtaining two single events in adjacent pixels, providing evidence for the location of RTS in the inter-electrode or channel stop high field regions.

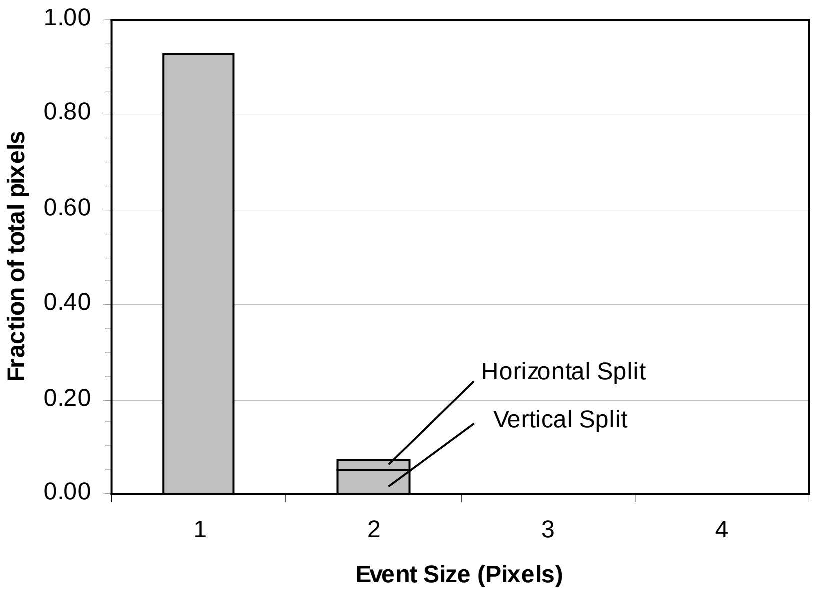

Figure 6.12 The distribution of event sizes from a total of 921 RTS pixels

Further evidence for the location of RTS in the high field regions of a pixel can be obtained by considering the physical structure of a pixel and the charge storage and transport volumes. Figure 6.13 is a diagram of the CCD47-20 3-phase pixel structure, indicating the charge storage region, the inter-electrode and channel stop high field regions and the associated movement of charge for the potential situation shown.

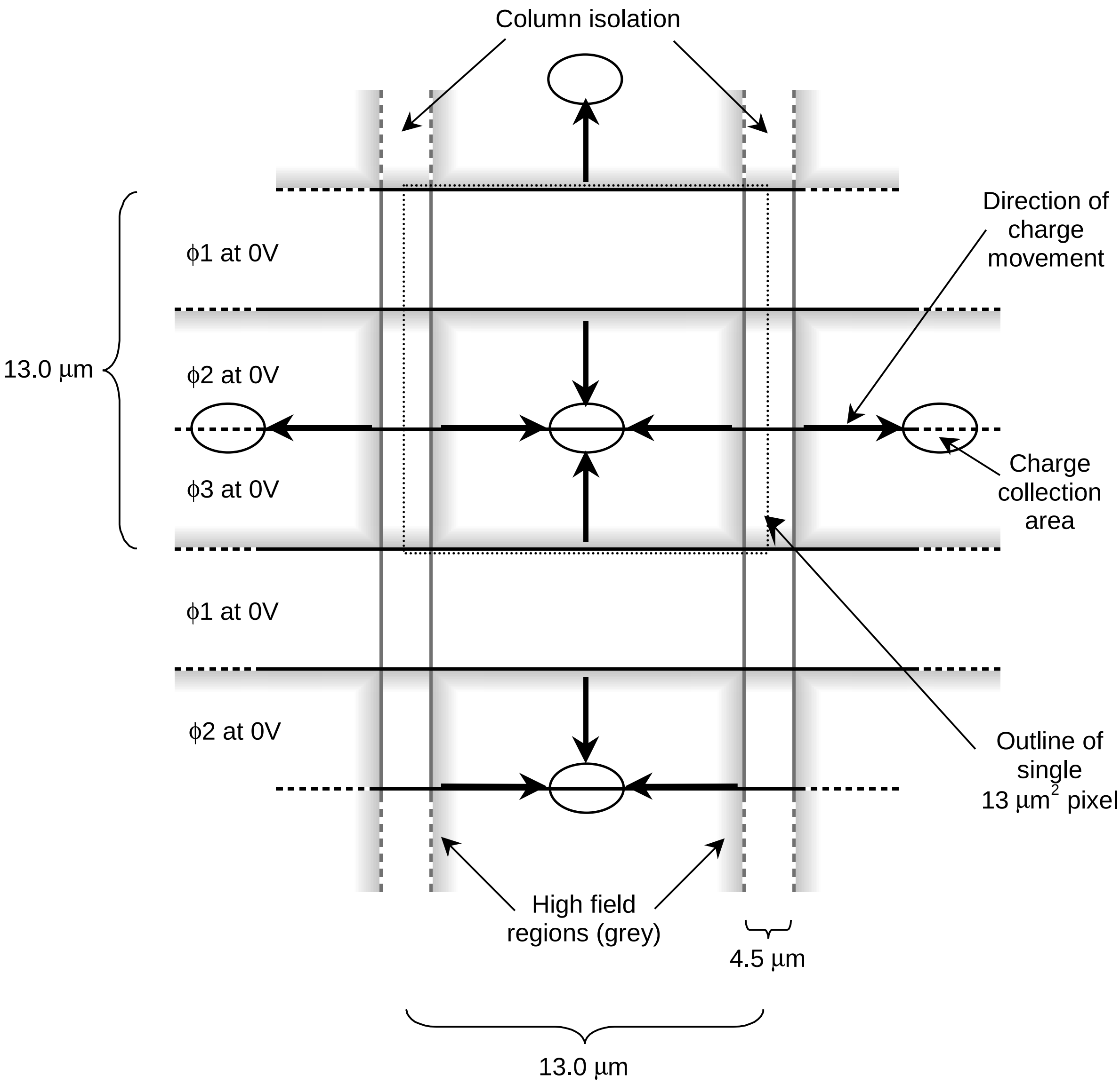

Figure 6.13 The structure of a CCD47-20 pixel indicating the inter-electrode and channel stop high field regions and the movement of charge into the charge storage region of each pixel

Assuming the depth and width in each case to be the same, the ratio of the volume of the charge storage region in a CCD47-20 pixel during a single pixel transfer, V_{cs}, to the volume of the high field region within, V_{hf}, can be approximated by:

$$\frac{V_{cs}}{V_{hf}} = \frac{D_{transfer}}{D_{hf}} \tag{6.1}$$

Where $D_{transfer}$ is the distance travelled during a single pixel transfer and D_{hf} is the distance travelled through a high field region during the transfer. Substituting in suitable values of 13 μm and 0.2 μm respectively, V_{cs}/V_{hf} is found to be 65. If this value is comparable to N_{traps}/N_{RTS}, where N_{traps} is the number of traps in a given sample of pixels and N_{RTS} is the number of pixels in the sample showing RTS characteristics, this provides indirect evidence that the RTS phenomenon may be linked with traps located in the high field regions of a CCD pixel.

After irradiation of device 9211-4-4 with 3×10^{8} protons cm^{-2}, from an area containing 18400 pixels ~1.2 % had a charge level greater than 5σ of the mean dark current level. Of this fraction, ~45 % will exhibit RTS characteristics, i.e. ~100 of the sample pixels. An irradiation fluence of 1×10^{9} protons cm^{-2} results in a CTI of ~2×10^{-4} electrons per pixel (Holland et al. 1991). For a Mn Kα X-ray this CTI value results in the loss of a single electron per transfer through 3 pixels. In a sample of 18400 pixels there will therefore be ~6000 traps. In this instance N_{traps}/N_{RTS} is found to be 60, comparable with the V_{cs}/V_{hf} value 65 supporting the high field location of RTS phenomena.

6.6.2. Amplitude Properties

The mean RTS transition amplitude over a 1 hour period was recorded at 5 ^{o}C intervals from 45 ^{o}C to 55 ^{o}C for 85 RTS pixels. The transition amplitude is the change in dark current level from the bright pixel pedestal level to the high RTS amplitude. In 1 hour ~80 RTS transitions are observed at 45 ^{o}C, the number increasing to ~150 at 55 ^{o}C. Figure 6.14 shows histograms of the observed amplitudes at 45 ^{o}C, 50 ^{o}C and 55 ^{o}C. As temperature is increased the mean RTS transition amplitude also increases with the distribution of amplitudes becoming more widely spread. The mean RTS amplitude at each measured temperature is shown in Table 6.3. Figure 6.15 shows an example amplitude versus time plot for an RTS pixel at the three different temperatures, highlighting the transition amplitude change. The figure also shows how the bright pedestal amplitude increases with increasing temperature as a result of the extra dark current in the pixel.

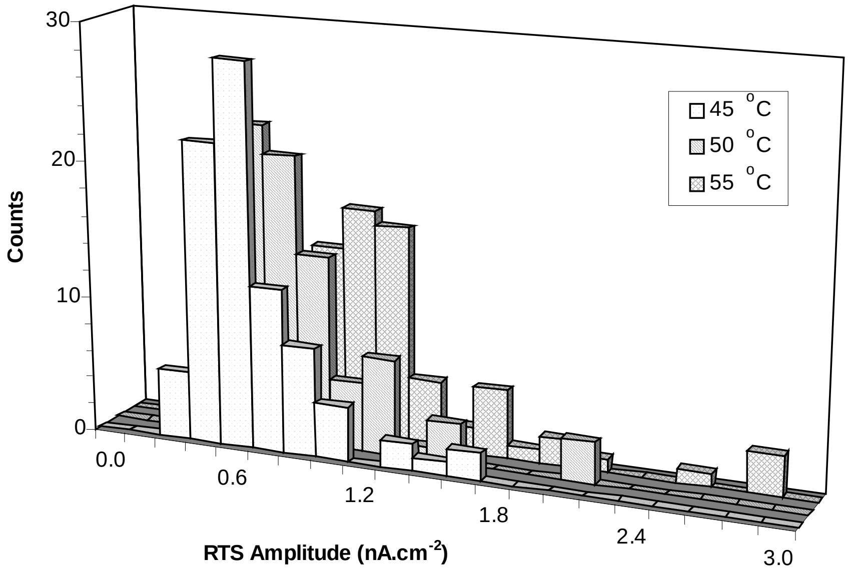

Figure 6.14 Histograms of RTS transition amplitudes of 85 RTS pixels at three temperatures

Temperature (°C)	*Mean RTS Transition Amplitude (nA.cm^{-2})*
45	0.60
50	0.75
55	1.05

Table 6.3 The mean RTS transition amplitude at different temperatures

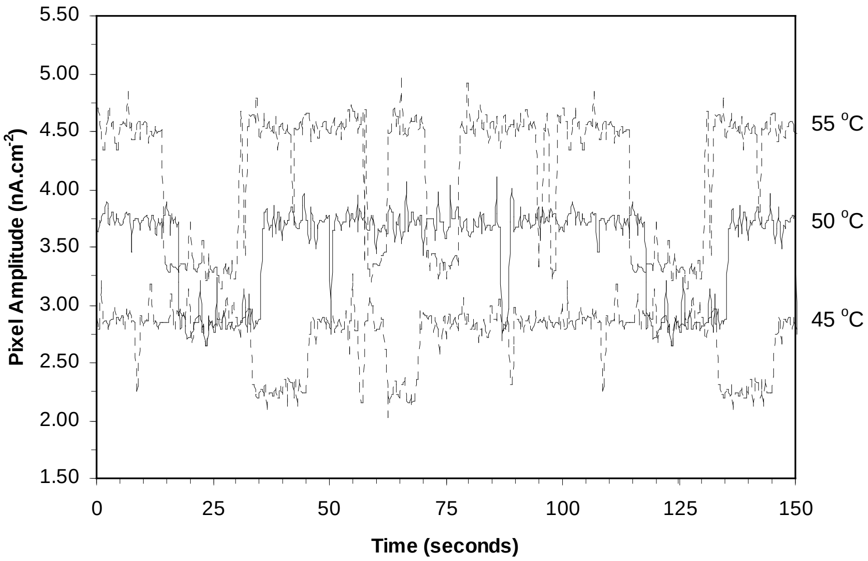

Figure 6.15 The variation in transition amplitude and bright pedestal amplitude with temperature of an RTS pixel

A previous investigation into RTS pixels in a TH7895M device, with pixels of 19 μm^2, looked to see if there was a correlation between the RTS transition amplitude and the dark current pedestal amplitude (Bond 1996). No correlation was observed for the data collected at 10 ^{o}C. Figure 6.16 shows the relationship between RTS transition amplitude and dark current pedestal amplitude for 24 RTS pixels of device 9211-5-3 at 45 ^{o}C and 55 ^{o}C and also displays the data recorded by Bond at 10 ^{o}C (1996). As the temperature increases the spread in the observed transition amplitudes becomes larger for higher pedestal amplitudes. A power law trendline can be fitted to all three data sets indicating a power law relationship between the temperature of the device and the spread in the transition amplitude and pedestal amplitude correlation.

The mean transition amplitude of 10 RTS pixels was evaluated at 2.5 ^{o}C intervals from 45 ^{o}C to 55 ^{o}C. Plotting the $\log_e$ of the transition energy as a function of 1/kT, the RTS transition amplitude was found to follow an Arrhenius relationship with a mean activation energy of 0.53 ± 0.13 eV. The results for 10 RTS pixels are shown in Figure 6.17. The errors associated with each data point are indicated for one data set and arise from the temperature stability error and the noise variation in the mean amplitude level of a given RTS pixel. This mean activation energy value is comparable with the activation energy of 0.57 ± 0.03 eV found by Bond (1996) and lies near the mid-band energy of 0.55 eV, indicating the E-center or the J-center as the defect most likely responsible for RTS.

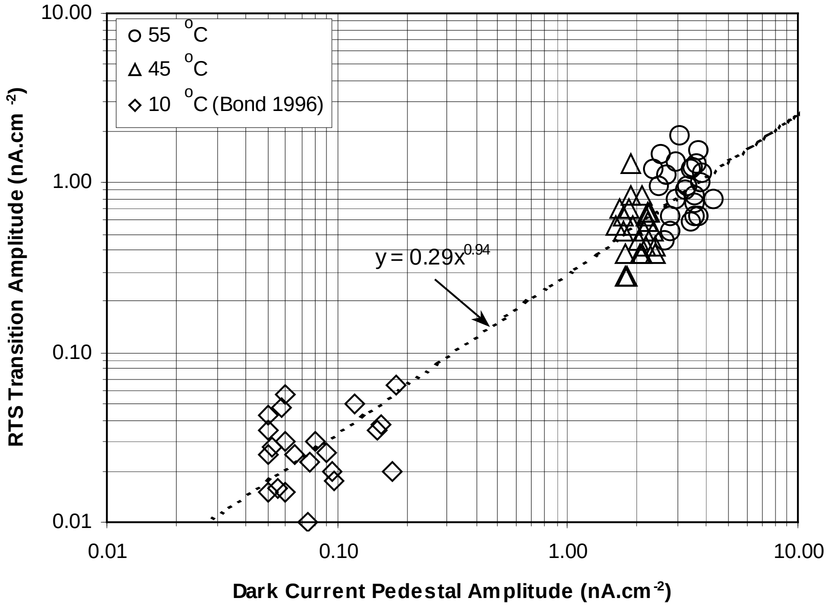

Figure 6.16 RTS transition amplitude variation with dark current pedestal amplitude

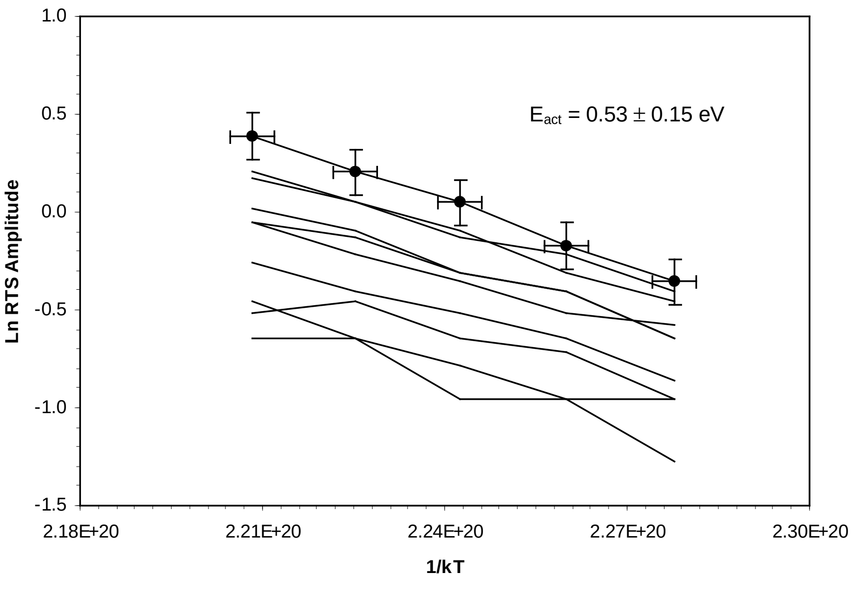

Figure 6.17 RTS transition amplitude activation energy

6.6.3. Period Properties

The period of time spent in the high and low amplitude states during each RTS transition was recorded for eight 2-level RTS pixels. A ‘switch’ from one level to another was defined as an amplitude change above 5σ of the mean dark current pedestal level of the given pixel, the length of time at a given amplitude level was defined as the ‘period’. Data were recorded at 2.5 ^{o}C intervals from 45 ^{o}C to 55 ^{o}C. Figure 6.18 shows an example amplitude verses time plot for an RTS pixel at the three different temperatures highlighting the high and low state period changes. Figure 6.19 shows histograms of the recorded low and high period measurements at 45 ^{o}C, 50 ^{o}C and 55 ^{o}C. The bin size for the low state period histogram is 2 seconds and the bin size for the high state period histogram is 10 seconds.

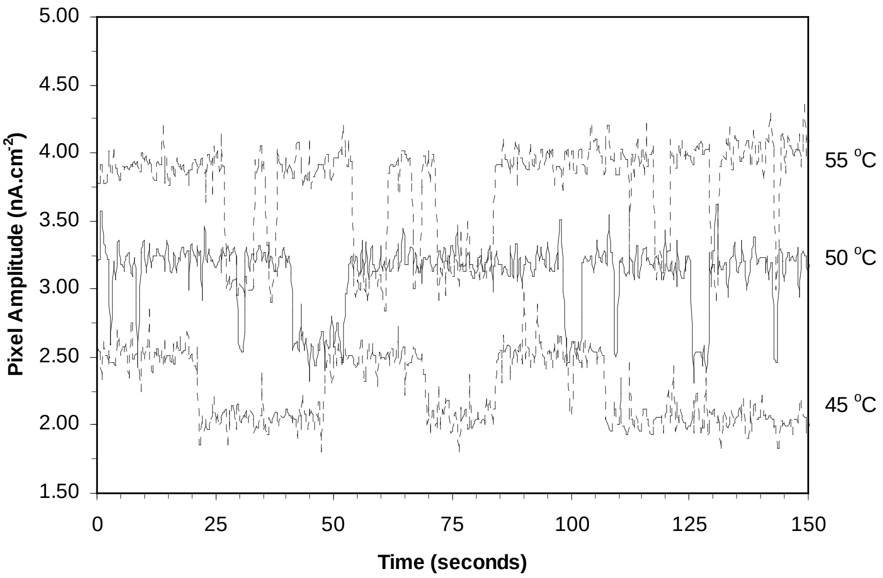

Figure 6.18 The variation in high and low state period with temperature of an RTS pixel

As temperature is increased the distribution of observed high and low state periods becomes narrower, the mean time spent in a high or low state becoming shorter. Chi^2 fitting was used to determine the time constant for each state at the five measured temperatures. The mean time in the low state was best fit by a single exponential in each case. Plotting the $\log_e$ of each measured low state time constant as a function of 1/kT reveals an Arrhenius relationship with an activation energy of 0.2 ± 0.1 eV.

The high state data are better fitted by a combination of two exponential functions, revealing one time constant that varies with temperature in a similar way to that of the low state and a second time constant that varies more markedly. Figure 6.20 shows the Arrhenius relationship of the two high state time constants that have activation energies of 0.1 ± 0.1 eV and 0.2 ± 0.1 eV and also shows the low state data. The error associated with each data point is shown. All three measured period activation energies are within the measured error, indicating that an activation energy of ~0.2 ± 0.1 eV is common to all three measured time constants. The RTS study by Bond (1996) found a single time constant for the low state and also only a single time constant for the high state. In each case the period activation energy was found to be 0.9 ± 0.1 eV, much larger than the observed value in this study.

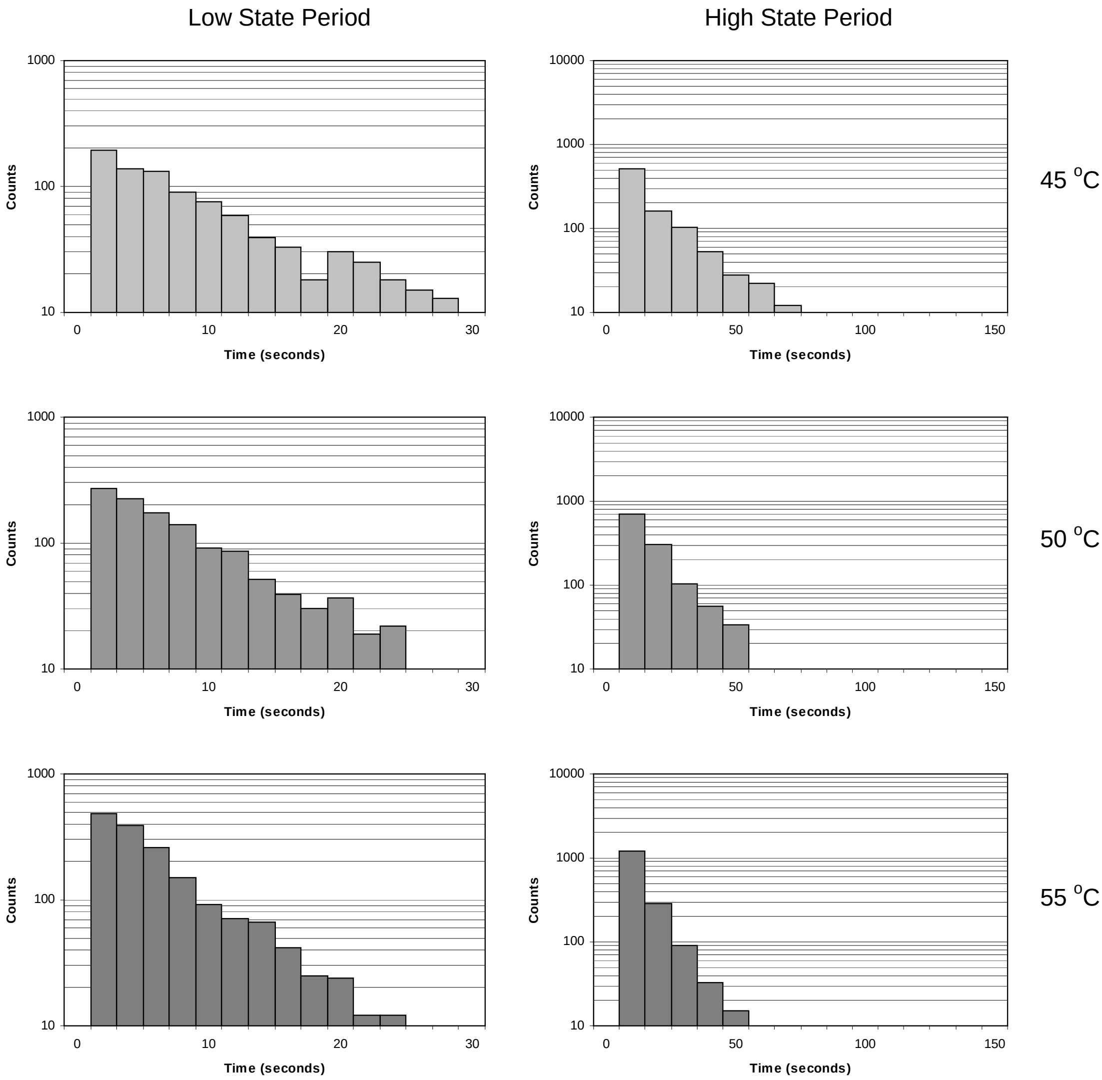

Figure 6.19 Histograms of RTS high and low state periods from a sample of 8 RTS pixels at three temperatures

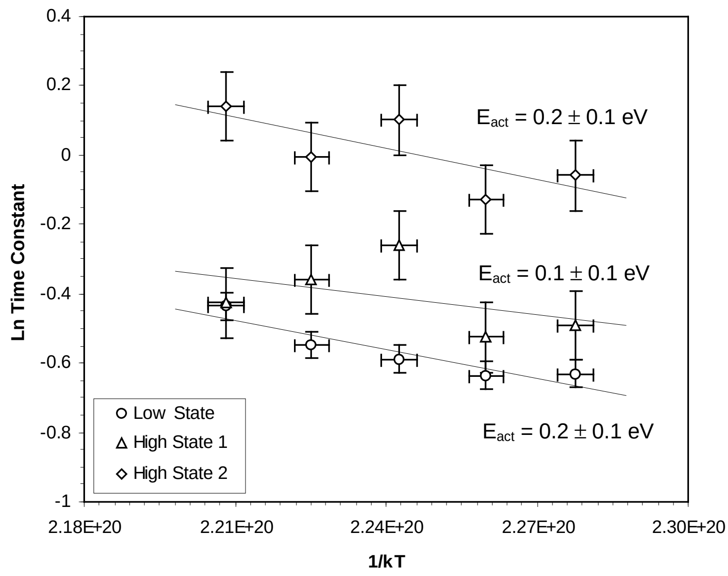

Figure 6.20 RTS high and low state period activation energies

6.6.4. Annealing

The possible link between the RTS phenomenon and the E-centre, suggested by the comparable RTS amplitude and E-centre activation energies, was further investigated by an annealing study. Device 9211-5-3 was subjected to an unbiased anneal at a temperature of 120 ^{o}C for a period of 2 hours. The characteristic anneal temperature of the E-centre is ~120 ^{o}C. If the mechanism behind the RTS phenomenon is linked to the E-centre, a significant fraction of the RTS pixels observed before heating the device should have annealed when investigated afterward.

Characterisation of 69 RTS pixels, of which 6 had >2 distinct amplitude levels, took place both before and after the anneal. The characterisation involved recording the amplitude of the selected RTS pixels at 0.25 second intervals for 5 minutes. All the selected RTS pixels were from the 3.6×10^{8} protons cm^{-2} irradiated area of the CCD. The data was collected at 50 ^{o}C.

Post-anneal Classification	*Number of Pixels*	*% of Total Pixels*
RTS completely annealed	50	72.5
RTS partially annealed	3	4.3
RTS still present	16	23.2
Total	69	100

Table 6.4 Post-anneal characteristics of a sample of 69 RTS pixels

Table 6.4 summarises the state of the 69 monitored RTS pixels after the anneal. Of the total sample, 28 % of the pixels still showed RTS characteristics, while 72 % were completely annealed. This is comparable to the value of ~80 % obtained by Holland (1990) when annealing bright pixels at 160 ^{o}C for 16 hours. The large fraction of RTS pixels annealed strongly supports the case for the underlying mechanism behind the phenomenon being linked to the E-centre. It is also interesting to note that of the 6 RTS pixels with more than 2 distinct amplitude levels, three annealed completely while 3 only annealed 2 of their amplitude levels. This observation strongly supports the idea that multi-level RTS is the result of more than one bi-stable defect occurring within a given pixel, a single RTS defect annealing away reducing the number of observed amplitude levels by two in each of the observed cases. Figure 6.21 shows the variation in amplitude over time for six of the monitored pixels both before and after annealing.

Previous work by Bond (1996) observed changes in the amplitude and period of 7 monitored RTS pixels during a stepped anneal study. The study found that RTS defects are gradually annealed, the time in the high state amplitude became increasingly long until it eventually became infinite. In contrast, of the 50 RTS pixels that were annealed in the work carried out for this thesis, 42 displayed amplitudes very close or below the pre-anneal low state amplitude. Of the remaining 8 annealed RTS pixels, only 1 was annealed to an amplitude level comparable to the pre-anneal high state amplitude, the rest annealing to amplitude levels between that of the pre-anneal high and low amplitudes.

There were 16 pixels that still exhibited RTS characteristics after annealing. In each case the flickering period and transition amplitude had decreased slightly, with the exception of 2 pixels where the RTS transition amplitude had become much larger than it was before annealing, as shown in Figure 6.22.

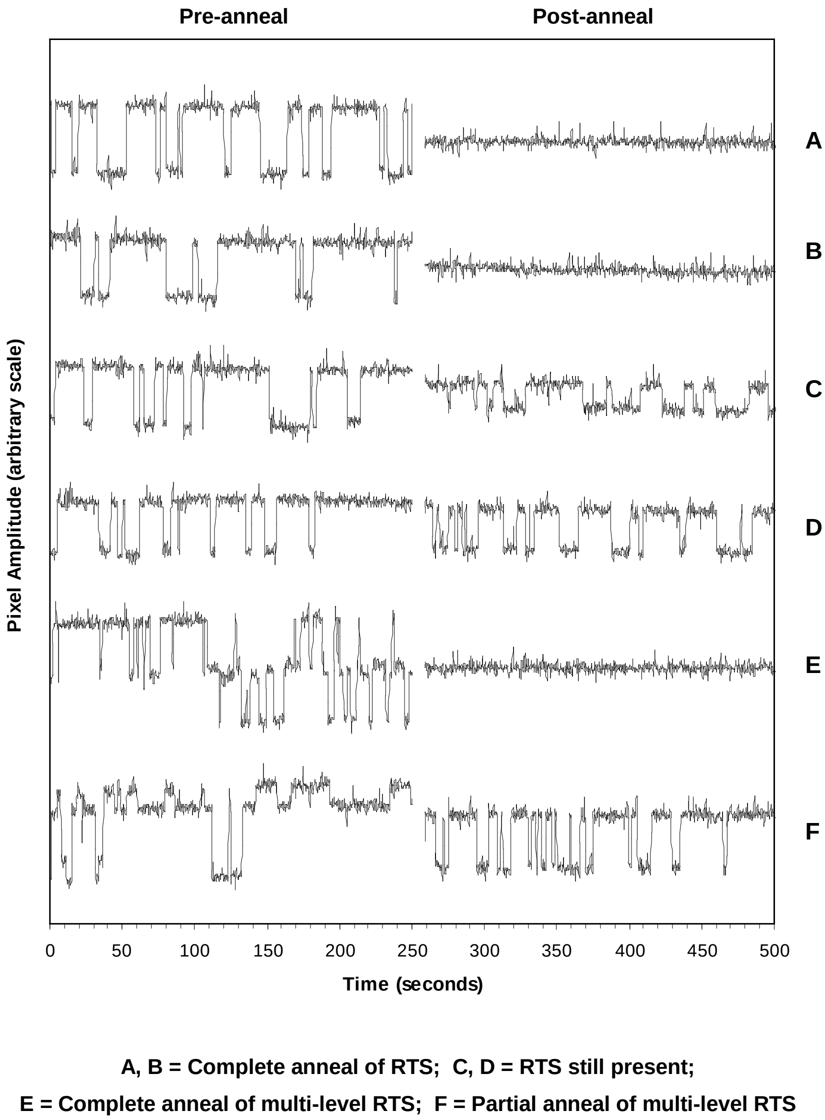

Figure 6.21 The amplitude variation with time of RTS pixels monitored before and after annealing. The amplitude scale is arbitrary to allow the presentation of the data, however the relative amplitude scale of each data set is the same

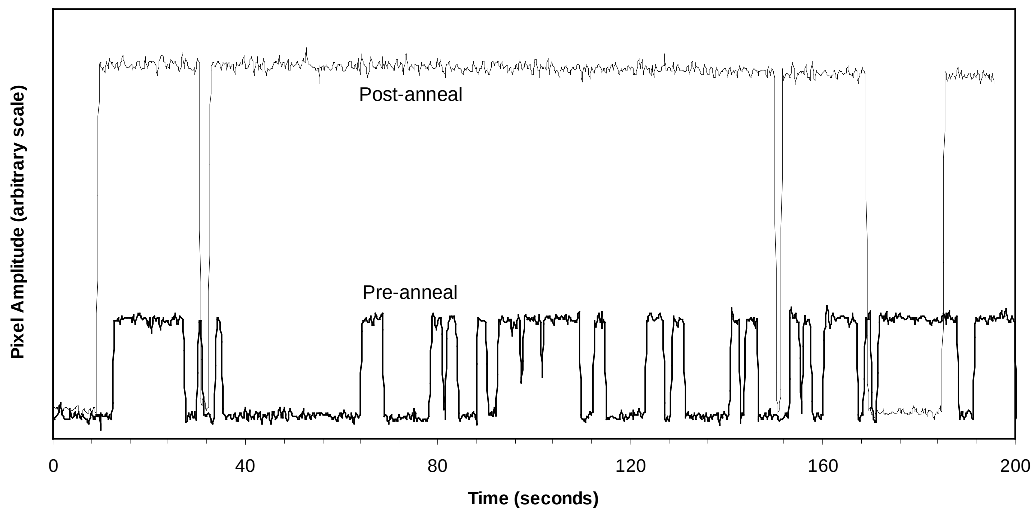

Figure 6.22 The amplitude variation with time of an RTS pixel showing a large increase in transition amplitude after annealing

6.7. Discussion

The RTS pixels observed after proton irradiation of CCD47-20 devices display very sharp amplitude transitions between distinct levels with high time constants and well defined activation energies. After a 10 MeV equivalent proton dose of ~3×10^8 cm^{-2}, approximately 45 % of the bright pixels in the irradiated area show signs of dark current fluctuation between two or more distinct amplitude levels above 5σ of the mean dark current level. The spread of bright pixels and pixels exhibiting RTS characteristics is uniform throughout the area of irradiation. Of the observed RTS pixels >90 % were isolated events, indicating the mechanism behind the RTS phenomenon may physically lie inside the inter-electrode and channel stop high field regions of a given pixel. Consideration of the physical structure and the extent of the high field regions within a CCD pixel also support this hypothesis, the ratio of the charge storage volume to the volume of the high field region in a pixel being comparable to the ratio of the number of traps to the number of RTS defects observed within a pixel. These ratios are 65 and 60 respectively.

The number of RTS pixels with >2 distinct amplitude levels is lower than the statistically expected number if >2 levels is the result of two or more 2-level RTS mechanisms residing within a given pixel. This is due to the thermal noise on the dark current level making it hard for the analysis software to detect the distinct amplitude levels. This fact does however support the idea that multi-level RTS is not due to a separate mechanism to that of 2-level RTS, the most likely cause being a number of 2-level RTS being present within the same pixel. The observed partial annealing of multi-level RTS is also in agreement with this hypothesis. RTS pixels exhibiting 3 distinct amplitude levels and not a multiple of 2 can be explained not only by the inability of the software to detect other amplitude levels above the noise in the data, but also by consideration of the magnitude of the high and low state amplitudes of each defect in the pixel. The observed pixel amplitude at any given time is the superposition of the amplitude of each defect in the pixel at that moment. If there are two bi-stable defects within a given pixel the resulting pixel amplitude can show 4 amplitude levels or 3. The observation of 3 levels arises when the transition amplitude of each of the bi-stable defects is within the measurement resolution. A similar superposition argument can be used to deduce that for three bi-stable defects within a given pixel, any number of amplitude levels between 4 and 8 can be observed.

The RTS transition amplitude does not show a strong correlation with the dark current pedestal amplitude, with transition amplitudes varying over a range of ~1 nA cm^{-2} for a given pedestal amplitude at 45 ^{o}C. As temperature is increased the dark current increases, the spread in the observed transition amplitudes becoming larger for higher pedestal amplitudes.

The above observed RTS properties indicate the likely mechanism behind RTS involves discrete transitions between two states separated by an energy barrier. A number of theoretical explanations of the RTS phenomenon have been proposed and these models are described below:

- **Field Enhancement:** The defect must be field enhanced, accounting for the large transition amplitudes, low activation energies and correlation to bright pixels. The defect responsible may be located in the inter-electrode or channel stop regions of a pixel where the electric field is larger due to Poole-Frenkel enhancement. Another suggestion is that charge captured by a defect may create an electric field around itself which then influences nearby defects. However, the field created would not reach very far and the resulting number of defects influenced would not be enough to account for the large transition amplitudes seen. This idea is also statistically unlikely if there are not many defects present in the silicon lattice.

- **Multiple Defects:** The high transition amplitudes may be the result of many bulk defects contributing charge at the same time. Work has shown that around 50 defects would be required to act together to generate the amplitudes seen and so this theory is thought to be unlikely (Kirton et al. 1989).

- **Multi-stable Defect:** The observed well defined time constants suggest that a multi-stable defect, with two or more states separated by an energy barrier, may be responsible for the RTS phenomenon. The defect must be common as it is widely seen after, and in some cases before, proton irradiation of a device. There are however, no known defects with the appropriate activation energy and energy states. Normally the time constants of capture and emission of charge are thermally independent. This is not true for the observed RTS time constants, which show a strong temperature dependence. The RTS switching phenomenon therefore involves a mechanism that is independent of simple electron capture and emission probabilities.

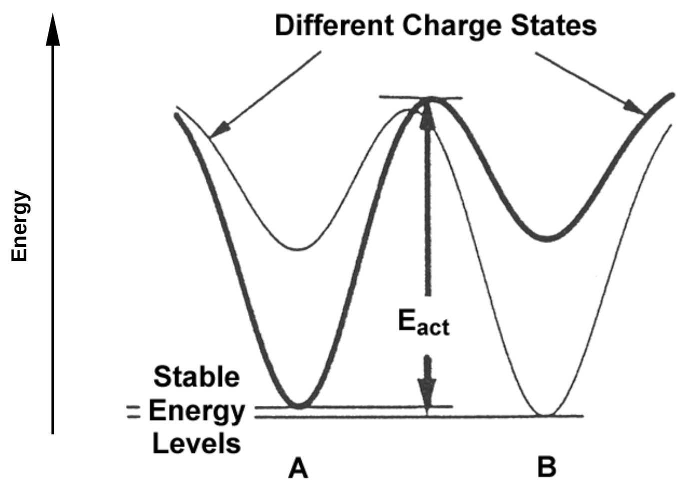

Figure 6.23 Energy verses defect configuration for a defect with two stable states, A and B

A proposed model is a multi-stable defect with the stable configuration dependent on the charge state: state A being stable for one charge state, and state B being stable for another

(Chantre 1989, Watkins 1991). The configuration can be flipped over the potential barrier from state A to state B by thermal fluctuations. The energy level of each state, along with any field enhancement, will determine the level of thermally generated conduction band electrons and therefore the dark current amplitude level. If one state is nearer the mid gap than the other there will be two clear dark current levels observed after field enhancement. This model can not explain the multi-level RTS pixels observed, if they are the result of a different process to 2-level RTS, and also does not account for the second high period time constant observed in the data. Figure 6.23 illustrates the proposed defect. In one charge state, state A has the lower energy, while in the other charge state, state B has the lower energy.

- **Reorientation of the E-centre:** This model was suggested by Bond (1996) and involves the reorientation of the E-centre in a strong electric field. The correlation between RTS behaviour and dark current spikes indicates that the defect responsible for the dark current spikes may also be the cause of RTS. The E-centre is a common bulk defect in proton irradiated silicon and is generated in numbers large enough to explain the large fraction of pixels exhibiting RTS after irradiation. It has been shown that the E-centre in its neutral charge state has an extra positive charge on the P-atom, and a corresponding extra electron orbital (Watkins and Corbett 1964). The defect has a resulting dipole moment, and the field enhancement factor caused by the defect will depend on its orientation within the applied electric field (Martin et al. 1981). The E-centre has been observed to reorient its axis, the vacancy taking the place of any one of the four nearest silicon atoms to the phosphorous atom, moving through the silicon lattice by thermally overcoming potential barriers (Watkins and Corbett 1964). Figure 6.24 shows the structure of the silicon lattice containing an E-centre defect and one possible reorientation. The level of dark current generation is dependent on the orientation of the defect within the applied electric field. A movement of the vacancy from a small angle to a large angle relative to the electric field vector will result in large amplitude RTS signals and vice-versa.

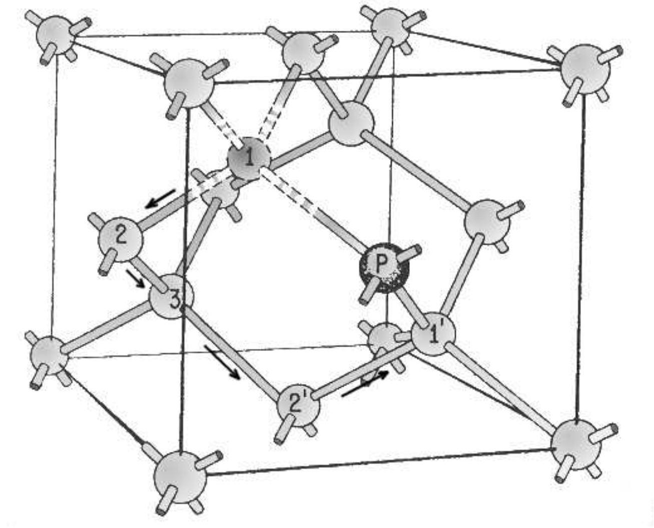

Figure 6.24 The silicon lattice containing an E-centre defect. The vacancy can reorient itself from its normal position nearest the phosphorous atom to a new nearest site by moving through the lattice as shown

For this model to be viable, RTS time constants should be correlated to the kinetics of reorientation of the defect. The measured activation energies for reorientation are 0.93 ± 0.05 eV, higher than the observed 0.2 ± 0.1 eV observed in the CCD47-20 study presented. The model also explains the lack of a correlation between RTS amplitude and the dark current pedestal, and lack of any direct evidence for field enhancement, as the model assumes the amplitude is dependent on the defect orientation, not the electric field strength. Electric fields have however been observed to influence the reorientation kinetics of defects, which may explain the large variation in time constants observed (Kimerling 1979).

The models described above each provide explanations for a number of observed RTS characteristics, but not all. The reorientation of the E-centre provides the most detailed description of a mechanism to explain the RTS phenomenon, but does not account for the two high state time constants observed in the data obtained for this thesis. The work in this chapter has shown that the most likely model for RTS involves the E-centre, the high field regions of a device and a single bi-stable mechanism.

6.8. Summary

This chapter has presented an in-depth study of fluctuating pixels in proton irradiated CCDs. The prevalence of the ‘Random Telegraph Signal’ phenomenon and the lack of understanding of the underlying mechanism was described first, followed by descriptions of the devices used for the study. The irradiation methodology was then presented followed by an in-depth analysis of the induced RTS pixel characteristics. The RTS phenomenon was shown to be strongly linked with the E-centre and most likely physically located within the high field regions of a device. A number of models for the underlying mechanism have been presented, the most plausible involving a single bi-stable defect configuration that can be thermally flipped from one stable state to another giving rise to the amplitude and period characteristics observed.

Chapter 7: Conclusions and Future Work

This chapter summarises the main conclusions of the three studies carried out for this thesis and indicates directions for possible future work in each case.

7.1. L3Vision Radiation Testing

To assess the potential of using L3Vision technology in space applications, two E2V Technologies CCD65 devices incorporating the L3Vision technology were irradiated with proton fluences representative of total mission fluences received by spacecraft operating in low Earth orbit. The main conclusions of the study are given below:

- After irradiation the two devices were shown to operate as expected with the resulting increase in dark current and number of bright pixels generated by each irradiation being comparable to previous proton irradiation studies on other devices.

- The L3Vision gain register operated normally after proton irradiation.

- Bright pixels generated in the gain register appeared not to be located in the high field avalanche regions as they exhibited similar characteristics to the bright pixels generated in the image section of the device.

The study has revealed no significant problems inhibiting the use of L3Vision technology in space applications although there is a need for further proton irradiation studies involving a larger number of devices to improve on current statistics and deduce if a bright defect generated in the avalanche region of a pixel in the gain register can cause device failure. A proton irradiation study of a batch of ~25 CCD65 devices featuring the L3Vision technology is currently being planned to address this question.

7.2. The Effect of Low Energy Protons on CCDs

The impact of low energy protons on the operational characteristics of CCD22 devices was investigated to assess the damage contribution of low energy protons to the observed on-orbit CTE degradation of the EPIC MOS devices of XMM-Newton. The main conclusions of the study are:

- Protons with energy of order a few keV cause more damage than that expected by the Non-Ionising Energy Loss function as they deposit the majority of their energy within the CCD.

- The greatest amount of damage to the buried channel is associated with the highest amount of energy deposited within it, the most damage caused by protons of ~220 keV which come to rest within the CCD buried channel volume.

- The component of the observed CTE degradation of the EPIC MOS devices of XMM-Newton attributed to soft protons is small, <20 %.

- The operation of the XMM-Newton spacecraft is optimal for keeping the soft proton flux reaching the EPIC MOS CCDs to a minimum.

The study also resulted in the development of a computational model that can be used to simulate the CTI expected after irradiation of a CCD with low energy protons. Input to the model involves specifying a representative CCD structure, in this case a CCD22 device, and can therefore be used to model other CCD devices in the future.

7.3. Random Telegraph Signals

A detailed investigation of the 'Random Telegraph Signal' phenomenon has been carried out with a number of new findings being made. The study involved the irradiation of two CCD47-20 devices with protons, and the subsequent development of detailed analysis software to allow the characterisation of radiation induced RTS pixels. The main findings of the RTS investigation are as follows:

- Approximately 45 % of bright pixels generated after proton irradiation exhibit RTS behaviour.

- The observed RTS pixels exhibited amplitude and period behaviour comparable to previous studies.

- Occurrence statistics and annealing results show the mechanism for RTS involves two distinct amplitude levels, RTS pixels with >2 amplitude levels being the result of more than one such bi-stable defect residing within the pixel.

- The large amplitude variations associated with RTS pixels indicate the RTS phenomenon is linked with the high field regions of a CCD pixel. Consideration of the pixel structure, the charge storage volume and extent of the high field region within a pixel also support this finding.

- The large number of RTS pixels generated after irradiation and the large amount of RTS pixels annealed at 120 ^{o}C provides strong evidence that the underlying mechanism behind RTS is linked with the E-centre. The RTS amplitude activation energy was found to be around mid-band, 0.53 ± 0.13 eV, also supporting the link with the E-centre which lies at 0.44 eV below the conduction band.

Future work will involve the use of a proton microprobe to ‘inject’ protons into specific regions of a CCD pixel allowing direct measurement of the location of bright and RTS defects within the volume of a pixel and accurate correlation with the high field and charge storage regions (Simon 2003).

Bibliography

Abbey, A. F., private communication, 2003.

Abbey, A. F., P. J. Bennie, M. J. L. Turner, B. Altieri, S. Rives, "Cooling out the Radiation Damage on the XMM-Newton EPIC MOS CCDs", *Nuc. Inst. and Meth.*, vol. **A513**, (2002), pp. 136-42.

Alig, R. C., S. Bloom, C. W. Struck, "Scattering by ionisation and phonon emission in semiconductors", *Phys. Rev. B.*, vol. **22**, (1980), pp. 5565-82.

Ambrosi, R. M., A. D. T. Short, A. F. Abbey, A. A. Wells, D. R. Smith, "The effect of proton damage on the X-ray spectral response of MOS CCDs for the Swift X-ray Telescope", *Nuc. Inst. Meth.*, vol. **A482**, (2002), pp.644-52.

Ballet, J., private communication, 2003.

Banghart, E. K., J. P. Lavine, E. A. Trabka, E. T. Nelson, B. C. Burkey, "A model for charge transfer in buried channel CCDs at low temperatures", *IEEE Trans. Electron Devices*, vol. **38**, (1991), pp. 1162-74.

Barbe, D. F., "Imaging devices using the charge coupled concept", *Proc. IEEE*, vol. **63**, (1975), pp. 38-67.

Bennie, P., "Digest of the EPIC MOS CCD damage", University of Leicester, Department of Physics and Astronomy Report, (2001).

Bertolini, G., A. Coche, "*Semiconductor Detectors*", North-Holland Pub. Co., Amsterdam, 1968.

Beynon, J. D. E., D. R. Lamb, "*Charge-coupled devices and their applications*", McGraw-Hill Book Co. (UK) Ltd., 1980.

Bond, I. H., "Radiation damage in optical charge coupled devices", Ph. D. Thesis, University College London, 1996.

Boyle, W. S., G. E. Smith, "Charge Coupled Semiconductor Devices", *Bell Syst. Tech. Jn.*, vol. **49**, (1970), pp. 587-93.

Bredthauer, R. A., J. H. Pinter, J. R. Janesick, L. B. Robinson, "Notch and large-area CCD imagers", *Proc. SPIE*, vol. **1447**, (1991), pp. 310-15.

Burke, E. A., "Energy dependence of proton-induced displacement damage in silicon", *IEEE Trans. on Nuc. Sci.*, vol. **33**, no. 6, (1986), pp. 1276-81.

Burrows, D. N., J.E. Hill, J.A. Nousek, A. Wells, A.D.T. Short, R. Willingale, O.Citterio, G. Chincarini, G. Tagliaferi, “The Swift X-ray Telescope”, *Proc. SPIE*, vol. **4140**, (2000), pp. 64-75.

Burt, D., private communication, 2002.

Castelli, C. M., “The soft X-ray performance of CCD detectors”, Ph. D. Thesis, University of Leicester, 1991.

Chantre, A., “Introduction to defect bistability”, *J. Appl. Phys.*, vol. **A48**, (1989), pp. 3-9.

Chowanietz, E. G., “Advances in CCDs for X-ray imaging and spectroscopy”, Ph. D. Thesis, University of Leicester, 1986.

Clauβ, T., “Einfluss von niederenergetischen Protonen auf pn-CCD-Detektoren”, Ph. D. Thesis, Institüt für Astronomie and Astrophysik der Eberhard-Karls-Universität Tübingen, Tübingen, Germany, 2000.

Dale, C., P. Marshall, B. Cummings, L. Shamey, A. Holland, “Displacement damage effects in mixed particle environments for shielded spacecraft CCDs”, *IEEE Trans. on Nuc. Sci.*, vol. **NS-40**, (1993), pp. 1628-37.

Daly, E. J., Internal project document, ESTEC/WMA/EJD/JET-X/1, (1989).

Daly, E. J., “The Radiation Belts”, *Radiation Physics and Chemistry*, vol. **43**, no. 1/2, (1994), pp. 1-17.

Emery, F. E., T. A. Rabson, “Average energy expended per ionized electron-hole pair in silicon and germanium as a function of temperature”, *Phys Rev.*, vol. **140**, no. 6A, (1965), pp. 2089-93.

Fano, U., “Ionization yield of radiations. II. The fluctuations of the number of ions”, *Phys. Rev.*, vol. **72**, no. 1, (1947), pp. 26-9.

Fowler, R. F., J. V. Ashby, C. Greenough, “Development of the EVEREST Device Modelling Software for Charge Generation Events”, Rutherford Appleton Laboratory Technical Report, RAL-TR-1998-075, (1998).

Gardiner, P., private communication, 2003.

Goswami, J., R. McGuire, R. Reddy, D. Lai, R. Jha, “Solar flare protons and alpha particles during the last 3 solar cycles”, *J. Geophys. Res.*, vol. **93**, (1988), pp. 7195-205.

Grove, A. S., “*Physics and Technology of Semiconductor Devices*”, John Wiley and Sons Inc., 1967.

Hartke, J. L., “The three-dimensional Poole-Frenkel effect”, *J. Appl. Phys.*, vol. **39**, (1968), pp. 4871-73.

Hess, W. N., “*The Radiation Belt and Magnetosphere*”, Blaisdell, 1968.

Heynderickx D., B. Quaghebeur, E. Speelman, E. J. Daly, “ESA’s SPace ENVironment Information System (SPENVIS): A WWW Interface to Models of the Space Enviroment and its Effects”, *Proc. AIAA*, vol. **0371**, (2000).

Hill, J. E., “The charge coupled device as an X-ray polarimeter”, Ph. D. Thesis, University of Leicester, 1999.

Holland, A. D., “Radiation effects in CCD X-ray detectors”, Ph. D. Thesis, University of Leicester, 1990.

Holland, A., A. G. Holmes-Siedle, B. Johlander, L. Adams, “Techniques for minimising space proton damage in scientific charge-coupled devices”, *IEEE Trans. on Nuc. Sci.*, vol. **NS-38**, (1991), pp. 1663-70.

Holland, A. D., “Annealing of proton-induced displacement damage in CCDs for space use”, *Inst. Phys. Conf. Ser.*, vol. **121**, (1991), pp. 33-40.

Holland, A. D., M. J. L. Turner, D. J. Burt, P. Pool, “The MOS CCDs for the European Photon Imaging Camera”, *Proc. SPIE*, vol. **2006**, (1993), pp. 2-10.

Holland, A. D., “The effect of bulk traps in proton irradiated EEV CCD’s”, Jet-X Project Document, JET-X(94)UL-230 WP2220, (1994).

Holmes-Siedle, A. G., S. J. Watts, A. D. Holland, Final report on ESTEC contract no. 8815/90/NL/LC(SC), “The irradiation, measurement and technology evaluation of X-ray sensitive CCDs for ESA scientific missions”, Brunel University, Uxbridge, UB8 3PH, UK, (1995).

Holmes-Siedle, A., L. Adams, “*Handbook of Radiation Effects*”, Oxford University Press, 2nd Ed., 2002.

Hopkins, I. H., G. R. Hopkinson, “Random telegraph signals from proton-irradiated CCDs”, *IEEE Trans. on Nuc. Sci.*, vol. **40**, no. 6, (1993), pp. 1567-74.

Hopkins, I. H., G. R. Hopkinson, "Further measurements of random telegraph signals in proton irradiated CCDs", *IEEE Trans. on Nuc. Sci.*, vol. **42**, no. 6, (1995), pp. 2074-81.

Hopkinson, G. R., D. H. Lumb, "Noise reduction techniques in CCD image sensors", *Jn. Phys. E.*, vol. **15**, (1982), pp. 1214-22.

Hopkinson, G. R., "Cobalt-60 and proton radiation effects on large-format 2-D CCD arrays for an Earth imaging application", *IEEE Trans. on Nuc. Sci.*, vol. **NS-39**, (1992), pp. 2018-25.

Hopkinson, G. R., "Proton damage effects on p-channel CCDs", *IEEE Trans. on Nuc. Sci.*, vol. **NS-46**, (1999), pp. 1790-96.

Howes, M. J., D. V. Morgan, "*Charge-coupled Devices and Systems*", John Wiley and Sons Ltd., 1979.

Hsieh, H. C., Luk, T. W., "Two-dimensional Transient Analysis of a Buried-Channel Charge-Coupled Device", *Solid-state Electronics*, vol. **27**, no. 3, (1984), pp. 213-24.

Hutchinson, I. B., "An investigation of the diffuse gas in the interstellar medium", Ph. D. Thesis, University of Leicester, 1999.

Janesick, J. R., "*Scientific Charge-Coupled Devices*", The Society of Photo-Optical Instrumentation Engineers, SPIE Press, Washington, 2001.

Jastrzebski, L., P. A. Lavine, W. A. Fisher, A. D. Cope, E. D. Savoye, W. N. Henry, "Cosmetic defects in CCD imagers", *Jn. Electrochem. Soc.*: Solid-state Science and Technology, vol. **128**, no. 4, (1981), pp. 885-92.

Jerram, P., P. Pool, R. Bell, D. Burt, S. Bowring, S. Spenser, M. Hazelwood, I. Moody, N. Catlett, P. Heyes, "The LLLCCD: Low light imaging without the need for an intensifier", *Proc. SPIE*, vol. **4306**, (2001), pp. 178-86.

Kandiah, K., "Low frequency noise mechanisms in field effect transistors", *Proc. Noise in Physical Systems and 1/f Noise*, (1985), pp. 19-25.

Kandiah, K., M. O. Deighton, F. B. Whiting, "A physical model for random telegraph signal currents in semiconductor devices", *J. Appl. Phys.*, vol. **66**, no. 2, (1989), pp. 937-48.

Keay, A., "An investigation of fine structure effects in CCDs developed for JET-X", Ph. D. Thesis, University of Leicester, 1997.

Kendziorra, E., T. Clauβ, N. Meidinger, M. Kirsch, M. Kuster, P. Risse, G. Hartner, R. Staubert, L. Strüder, "The effect of low energy protons on the performance of the EPIC pn- CCD detector on XMM-Newton", *Proc. SPIE*, vol. **4140**, (2000), pp. 32-41.

Kim, M., "Three-dimensional numerical analysis of astronomical charge-coupled device image sensors for X-ray or UV detection", Ph. D. Thesis, University of Leicester, 1995.

Kimerling, L. C., "Electronic stimulation of defect processes in semiconductors", *Inst. Phys. Conf. Ser.*, vol. **46**, (1979), pp. 56-73.

Kirton, J., M. J. Uren, S. Collins, M. Shulz, A. Karmann, K. Scheffer, "Individual defects at the Si SiO2 interface", *Semicond. Sci. Tech.*, vol. **4**, (1989), pp. 1116-26.

Larin, F., "*Radiation Effects in Semiconductor Devices*", John Wiley and Sons Inc., 1968.

Lemaire, J., A. D. Johnstone, D. Heynderickx, D. J. Rodgers, S. Szita, V. Pierrard, "Trapped Radiation Environment Model Development", *Aeronomica Acta*, vol. **393**, (1995), pp. 48-51.

Lumb, D. H., "X-ray imaging and spectroscopy with CCDs", Ph. D. Thesis, University of Leicester, 1983.

Mackay, C. D., R. N. Tubbs, R. Bell, D. Burt, P. Jerram, I. Moody, "Sub-electron read noise at MHz pixel rates", *Proc. SPIE*, vol. **4306**, (2001), pp. 289-98.

Marshall, P. W., C. J. Dale, E. A. Burke, G. P. Summers, G. E. Bender, "Displacement damage extremes in silicon depletion regions", *IEEE Trans. on Nuc. Sci.*, vol. **36**, no. 6, (1989), pp. 1831-39.

Martin, P. A., B. G. Streetman, K. Hess, "Electric field enhanced emission from non-coulombic traps in semiconductors", *J. Appl. Phys*., vol. **52**, no. 12, (1981), pp. 7409-15.

Messenger, G. C., "A summary review of displacement damage from high energy radiation in semiconductors and semiconductor devices", *IEEE Trans. on Nuc. Sci.*, vol. **NS-39**, (1992), pp. 468-73.

Morgan, D. V., K. Board, "*An Introduction to Semiconductor Microtechnology*", John Wiley and Sons Ltd., 2nd Ed., 1983.

Nartallo, R., E. Daly, H. Evans, P. Nieminen, F. Lei, P. Truscott, "Low angle scattering of protons on the XMM-Newton optics and effects on the on-board CCD detectors", *IEEE Trans. on Nuc. Sci.*, vol. **48**, no. 6, (2001), pp. 1815-21.

Nelms, N., "A new determination of the charged pion mass and muon neutrino mass upper limit from exotic atom X-ray spectroscopy", Ph. D. Thesis, University of Leicester, 2002.

O'Dell, S. L., M. W. Bautz, W. C. Blackwell, Y. M. Butt, R. A. Cameron, R. F. Elsner, M. S. Gussenhoven, J. J. Kolodziejczak, J. I. Minow, R. M. Suggs, D. A. Swartz, A. F. Tennant, S. N. Virani, K. M. Warren, "Radiation environment of the Chandra X-ray observatory", *Proc. SPIE*, vol. **4140**, (2000), pp. 99-110.

Parks, G. K, "*Physics of Space Plasmas: An Introduction*", Addison Wesley Pub. Co., California, US, chap. 6, 1991.

Prigozhin, G., S. Kissel, M. Bautz, C. Grant, B. LaMarr, R. Foster, G. Ricker, "Characterization of the radiation damage in the Chandra X-ray CCDs", *Proc. SPIE*, vol. **4140**, (2000), pp. 123-34.

Rasmussen, A., J. Chervinsky, J. Golovchenko, "Proton scattering off of XMM optics: XMM mirror and RGS grating samples", Columbia Astrophysics Laboratory Report, RGS-COL-CAL-99009, (1999).

Robbins, M. S., "Radiation damage effects in charge coupled devices", Ph. D. Thesis, Brunel University, 1992.

Roy, T., S. J. Watts, D. Wright, "Radiation damage effects in imaging charge coupled devices", *Nuc. Inst. and Meth.*, vol. **A275**, (1989), pp. 545-57.

Shiono, N., M. Shimaya, K. Sano, "Ionising radiation effects in MOS capacitors with very thin gate oxides", *Japanese J. App. Phys.*, vol. **22**, no. 9, (1983), pp. 1430-35.

Shockley, W., W. T. Reed, "Statistics of the recombination of holes and electrons", *Phys. Rev.*, vol. **87**, (1952), pp. 835-42.

Short, A. D., A. Keay, M. J. L. Turner, "Performance of the XMM EPIC MOS CCD detectors", *Proc. SPIE*, vol. **3445**, (1998), pp. 13-27.

Short, A. D., R. M. Ambrosi, M. J. L. Turner, "Spectral re-distribution and surface loss effects in Swift XRT (XMM-Newton EPIC) MOS CCDs", *Nuc. Inst. and Meth.*, vol. **A484**, (2002), pp. 211-24.

Short, A. D. T., private communication, 2002.

Shortes, S. R., W. W. Chan, W. C. Rhines, J. B. Barton, D. R. Collins, "Characteristics of thinned backside-illuminated charge-coupled device imagers", *App. Phys. Let.*, vol. **24**, no. 11, (1974), pp. 565-67.

Simon, A., C. Jeynes, R. P. Webb, R. Finnis, Z. Tabatabaian, P. J. Sellin, M. B. H. Breese, D. F. Fellows, R. van den Broek, R. M. Gwilliam, "The new Surrey ion beam analysis facility", in press, *Nuc. Inst. and Meth.*, vol. **B**, (2003).

Srour, J. R., "*Radiation Effects on and Dose Enhancements of Electronic Materials*", Noyes Publications, 1984.

Srour, J. R., R. A. Hartmann, K. S. Kitazaki, "Permanent damage produced by single proton interactions in silicon devices", *IEEE Trans. on Nuc. Sci.*, vol. **33**, no. 6, (1986), pp. 1597-1604.

Srour, J. R., C. J. Marshall, P. W. Marshall, "Review of displacement damage effects in silicon devices", *IEEE Trans. on Nuc. Sci.*, vol. **50**, no. 3, (2003), pp. 653-70.

Stassinopoulos, E. G., J. P. Raymond, "The Space Radiation Environment for Electronics", *Proc. of the IEEE*, vol. **76**, (1988), pp. 1423-42.

Stefanov, K. D., "Radiation Damage Effects in CCD Sensors for Tracking Applications in High Energy Physics", Ph.D. Thesis, Saga University, 2001.

Sze, S. M., "*Physics of Semiconductor Devices*", John Wiley and Sons Ltd., 2nd Ed., 1981.

Tranquille, C., "Solar proton events and their effect on space systems", *Radiation Physics and Chemistry*, vol. **43**, no. 1/2, (1994), pp. 35-45.

Turner, M. J. L., A. Abbey, M. Arnaud, M. Balasini, M. Barbera, E. Belsole, P. Bennie, J. P. Bernard, G. F. Bignami, M. Boer, U. Briel, I. Butler, C. Cara, C. Chabaud, A. Collura, M. Conte, A. Cros, M. Denby, P. Dhez, G. Di Coco, J. Dowson, P. Ferrando, S. Ghizzardi, F. Gianotti, C. V. Goodall, L. Gretton, R. G. Griffiths, O. Hainaut, J. F. Hochedez, A. D. Holland, E. Jourdain, E. Kendziorra, A. Lagostina, R. Laine, N. La Palombara, M. Lortholary, D. Lumb, P. Marty, S. Molendi, C. Pigot, E. Poindron, K. A. Pounds, J. N. Reeves, C. Reppin, R. Rothenflug, P. Salvetat, J. L. Sauvageot, D. Schmitt, S. Sembay, A. D. T. Short, J. Spragg, J. Stephen, L. Strüder, A. Tiengo, M. Trifoglio, J. Trümper, S. Vercellone, L. Vigroux, G. Villa, M. J. Ward, S. Whitehead, E. Zonca, "The European Photon Imaging Camera on XMM-Newton: The MOS Cameras", *Astronomy and Astrophysics*, vol. **365**, no. 1, (2001), pp. 27-35.

Van Allen, J. A., L. A. Frank, "Radiation around the Earth to a radial distance of 107,400 km", *Nature*, vol. **183**, (1959), pp. 430-34.

Van Lint, V. A. J., "The physics of radiation damage in particle detectors", *Nuc. Inst. and Meth.*, vol. **A253**, (1987), pp. 453-59.

Walden, R. H., R. H. Krambeck, R. J. Strain, J. McKenna, N. L. Schryer, G. E. Smith, "The Buried Channel Charge Coupled Device", *Bell Syst. Tech. Jn.*, vol. **51**, (1972), pp. 1635-40.

Watkins, G. D., J. W. Corbett, "Defects in irradiated silicon: electron paramagnetic resonance and electron-nuclear double resonance of the Si-E center", *Phys. Rev.*, vol. **134**, no. 5A, (1964), pp. 1359-77.

Watkins, G. D., "Metastable defects in silicon: hints for DX and EL2", *Semicond. Sci. Tech.*, vol. **6**, (1991), pp. 111-20.

Watts, S., A. Holmes-Siedle, A. Holland, "Further Radiation Evaluation of X-ray Sensitive Charge Coupled Devices (CCDs) for the XMM Telescope", Brunel University Report, BRUCRD-ESACCD-95-1R, (1995).

Ziegler, J. F., J. P. Biersack, U. Littmark, "*The Stopping and Range of Ions in Solids*", Pergamon Press, New York, 1985.